Imperial College London
Department of Mechanical Engineering

Compressor Blade Flutter in Combined Plunge-Twist Mode Shapes

George Harry Hill

June 2023

Submitted in part fulfilment of the requirements for the degree of Doctor of Philosophy in Mechanical Engineering of Imperial College London and the Diploma of Imperial College London.

Abstract

Modern aeroengine compressor designs strive to reduce weight and maintain high aerodynamic efficiency. Therefore, the aim of initial compressor designs is to implement novel features that achieve these goals. However, some modern features result in greatly reduced damping, which can lead to vibrational instabilities such as flutter. It is known that the first flap (1F) mode shape is particularly susceptible to flutter in compressors. A feature of the 1F mode shape is that it can be well approximated as a superposition of pure plunge and twist vibration, referred to as a combined mode shape.

This thesis aims to enhance understanding of flutter in combined plunge-twist mode shapes, with a focus on the interaction of flow and mode shape physics. The goal is to develop design guidelines for engine manufacturers early in the design process.

Unsteady CFD computations are conducted to determine the effect of different flow and modal parameters on the flutter stability of compressor cascades. Firstly, the influence of reduced frequency, plunge-twist ratio, and nodal diameter is investigated using experimentally validated CFD. A stability map of these input parameters is built, which shows that increasing the reduced frequency and plunge-twist ratio is beneficial for flutter prevention. Following this, a flutter model was developed to explain the location of the stability limit based on results from the parametric studies of the modal variables. This showed that the flutter limit for a subsonic compressor cascade can be expressed by the 'plunge-twist incidence ratio'. Finally, studies were conducted to determine how the inlet Mach number and flow incidence affect the flutter stability of a highly loaded compressor cascade. It was shown that the increased flow incidence and inlet Mach number are destabilising due to the increased complexity of the interaction of the unsteady flow and mode shape at off-design operating conditions.

Statement of Originality

The work presented in this thesis is, to the best of the candidate's knowledge, original and the candidate's own work, except as acknowledged in the text. The material has not been submitted, either in whole or in part, for a degree or comparable award of Imperial College or any other university or institution.

George Harry Hill
June 2023

Copyright Declaration

The copyright of this thesis rests with the author. Unless otherwise indicated, its contents are licensed under a Creative Commons Attribution-Non Commercial 4.0 International Licence (CC BY-NC).

Under this licence, you may copy and redistribute the material in any medium or format. You may also create and distribute modified versions of the work. This is on the condition that: you credit the author and do not use it, or any derivative works, for a commercial purpose.

When reusing or sharing this work, ensure you make the licence terms clear to others by naming the licence and linking to the licence text. Where a work has been adapted, you should indicate that the work has been changed and describe those changes.

Please seek permission from the copyright holder for uses of this work that are not included in this licence or permitted under UK Copyright Law.

Acknowledgements

I would first like to express my deepest gratitude to Dr. Sina Stapelfeldt for her exceptional guidance and support throughout this research project. Her technical expertise, passion for the topic, and insightful feedback have been instrumental in shaping the direction of this thesis. I am grateful to everyone that was a part of the DELTA projects, especially Julian Gambel Dipl.-Ing and Prof. Dieter Peitsch from TU Berlin and Dr. Bernhard Mueck and Dr. Sabine Schneider from Rolls-Royce Deutschland Ltd. They provided many helpful ideas and made the collaborative project really enjoyable. Thanks go to Peter Higgs for taking care of all the administration and keeping things running smoothly throughout my time at the Vibration UTC. I would like to thank all my colleagues from the Vibration UTC at Imperial College London for creating such a pleasant, friendly working environment. Their technical assistance and helpful discussions will be appreciated almost as much as our trips to the pub. Finally, I would like to thank my family, my girlfriend, and my amazing group of friends. They have all been so supportive, offered great advice, and empowered me throughout the writing of this thesis.

Contents

1 Introduction **14**

2 Background **16**
2.1 Blade-Disk Assembly Modes 16
2.2 Rotor Blade Aeroelasticity 20
2.2.1 Dynamic Aeroelasticity 21

3 Literature Review **25**
3.1 Types of Flutter 25
3.2 Influence of Mode Shape 26
3.3 Influence of Aerodynamics 34
3.4 Influence of Aeroacoustics 37
3.5 Turbulence Modelling 39

4 Objectives **40**

5 Methodology **42**
5.1 Flow Solver 42
5.2 Structural Model 42
5.3 Method of Flutter Computation 44
5.3.1 Aerodynamic Influence Coefficient Method 45
5.3.2 Work Done Method 48
5.4 Propagation of Acoustic Waves in Annular Ducts 49
5.5 Post Processing Methods 50
5.5.1 Local Aerodynamic Damping 50
5.5.2 Components of Aerodynamic Damping 52

6 Analysis of a Weakly Loaded Subsonic Linear Cascade **55**
6.1 Test Case 55
6.2 Computational Model 59
6.3 Computational Results 62
6.3.1 Validation 62
6.3.2 Steady State Results 68
6.3.3 Unsteady Results 70
6.3.4 Validation of Linear Cascade Approach 76
6.4 Chapter Summary 82

7 Flutter Model for Cascade Flows **84**
7.1 Model Definition 84
7.2 Validation and Simplification of the Model for a Subsonic Linear Cascade 92
7.3 Shape and Location of the Flutter Stability Limit 98
7.4 General Flutter Stability Parameter 100
7.5 Chapter Summary 102

8 Effect of Steady-State Aerodynamic Loading on Flutter Stability **103**
8.1 Test Case 103
8.2 Computational Implementation 104
8.3 Validation 109
8.4 Transonic Test Case Analysis 112
8.5 Effect of Varying Incidence 120
8.6 Effect of Varying Inlet Mach Number 132
8.7 Chapter Summary 138

9 Conclusions **140**

10 Future Work **144**

Bibliography **145**

Appendices **153**
I Proof of Work Done Analysis 153

List of Tables

5.1 Discrete distance function d_k as a function of the blade number k 46
5.2 Sign of W_1 for a pure plunge and pure twist mode shape at different points on the blade surface 52

List of Figures

1.1 Summary of aeroelastic instabilities in a typical turbofan . . . 14
2.1 First six annular disk mode shapes [8] . . . 16
2.2 First three fan blade mode shapes [10] . . . 18
2.3 Expanded 1F-2ND blade-disk assembly mode for a transonic fan . . . 19
2.4 Collar's aeroelasticity triangle . . . 21
2.5 Campbell diagram showing different aeroelastic instabilities . . . 23
2.6 Physical displacement for stable and unstable cases of vibration induced work done on the blade surface . . . 24
3.1 Regions of different flutter regimes on a compressor operating map [21] . . . 25
3.2 1F mode split into its plunge and twist components [6] . . . 28
3.3 Aerodamping as a function of blade mode frequency . . . 32
3.4 Flutter stability map produced by Carta [36] . . . 33
3.5 Components of work done per cycle as a function of mass flow rate [6] . . . 35
3.6 Aerodamping as a function of rotational speed . . . 36
3.7 Constant speed characteristic for the original SA model and the modified SA-PGH model of Lee [55] . . . 39
5.1 Schematic of a two-dimensional blade section vibrating with both a pure plunge (left) and pure twist mode shape (right) . . . 51
5.2 Time integral component W_2 as a function of phase of unsteady pressure . . . 52
6.1 Experimental test rig . . . 56
6.2 Test rig measurement section . . . 57
6.3 Vibrating blade module . . . 59
6.4 Measurement section geometry with dimensions . . . 60
6.5 Computational mesh showing blade -5 and the top wall . . . 61
6.6 Schematic showing rigid body rotation around the twist axis (T.A) . . . 61
6.7 Validation of the blade steady pressure coefficient against experimental data . . . 64
6.8 Validation of the blade unsteady pressure coefficient against experimental data – $k = 0.2$, $l/c = 1.3$ . . . 66
6.9 Validation of the complex AIC's – $k = 0.4$, $l/c = 1.25$ . . . 67
6.10 Validation of the aerodamping as a function of inter-blade phase angle – $k = 0.4$, $l/c = 1.25$ . . . 68
6.11 Mid-span steady pressure coefficient contour . . . 69

6.12 Steady pressure coefficient contour and streamlines of the suction side of blade 0 . . . 70
6.13 Aerodamping as function of IBPA for different l/c at $k = 0.6$. 71
6.14 Aerodamping as function of IBPA for different l/c at $k = 0.2$. 72
6.15 Harmonics of travelling wave mode coefficients expressed in terms of aerodamping, $k = 0.2$, $l/c = 2$ . . . 73
6.16 Aerodamping as function of k for different l/c . . . 74
6.17 Aerodamping as function of l/c for different k . . . 75
6.18 Flutter stability map . . . 76
6.19 Comparison of mid-span blade surface pressure coefficient profiles for the linear cascade and annular cascade . . . 79
6.20 Annular cascade mid-span pressure coefficient contour . . . 80
6.21 Aerodamping as a function of inter-blade phase angle for cases A–D . . . 81
6.22 Flutter stability maps for cases A–D . . . 82
7.1 Schematic of twist vibration induced incidence parameters . . 85
7.2 Schematic of plunge vibration induced incidence parameters . 86
7.3 Quasi-steady lift and moment due to combined plunge and twist vibration for a single vibration cycle . . . 88
7.4 Time integral D as a function of phase . . . 91
7.5 Constants of proportionality K as a function of reduced frequency k with $l/c = 1.5$ . . . 93
7.6 Constants of proportionality K as a function of twist axis setback l/c with $k = 0.4$ . . . 94
7.7 Contour maps of the phase of unsteady lift and moment due to plunge and twist vibration . . . 96
7.8 Flutter stability map produced using simple model . . . 98
7.9 $A(k)$ as a function of reduced frequency . . . 100
7.10 Flutter stability map including the stability parameter 'plunge-twist incidence ratio' . . . 101
8.1 Two-dimensional blade geometry and periodic boundaries . . . 104
8.2 Extent of computational domain . . . 105
8.3 Mesh convergence study . . . 107
8.4 Schematic showing rigid body rotation about the twist axis (T.A) . . . 108
8.5 Schematic of pure plunge mode shape implementation . . . 109
8.6 Isentropic Mach number validation of CFD against Repar [77] 110
8.7 Aerodamping as a function of inter-blade phase angle validation of CFD against Repar [77] . . . 112
8.8 Steady state Mach number contour (left) and blade surface isentropic Mach number (right) for the transonic test case . . 113

8.9 Stability map for the transonic test case . . . 114
8.10 Effect of reduced frequency on the a) amplitude of unsteady pressure coefficient, b) phase of unsteady pressure coefficient, and c) local work done per cycle for the transonic test case . . 117
8.11 Blade surface instantaneous unsteady pressure for $k = 0.2$ and $k = 0.3$ . . . 118
8.12 Aerodamping components as a function of l/c for $k = 0.5$ . . . 120
8.13 Selected operating points along the compressor characteristic for $M_i = 0.8$ . . . 121
8.14 Blade surface isentropic Mach number . . . 122
8.15 Mid-span Mach number contour near choke . . . 123
8.16 Mid-span Mach number contour near stall . . . 123
8.17 Aerodamping components as a function of incidence . . . 125
8.18 Upstream and downstream cut on reduced frequency as a function of incidence . . . 126
8.19 Effect of incidence on the a) amplitude of unsteady pressure coefficient, b) phase of unsteady pressure coefficient, and c) total aerodamping . . . 128
8.20 Suction side (SS) and pressure side (PS) contributions to the total aerodamping as a function of incidence – $k = 0.3$, $l/c = 2$ 129
8.21 Flutter regions for different flow incidences as a function of k and l/c . . . 131
8.22 Comparison of the flutter stability limit between the subsonic linear cascade and standard configuration 10 . . . 132
8.23 Blade surface isentropic Mach number for different inlet Mach numbers at fixed incidence . . . 133
8.24 Effect of Mach number on aerodamping – $k = 0.5$, $l/c = 0.9$. 134
8.25 Effect of Mach number on the a) amplitude of unsteady pressure coefficient, b) phase of unsteady pressure coefficient, and c) total aerodamping – $k = 0.5$, $l/c = 0.9$ . . . 136
8.26 Work done per cycle contour as a function of inlet Mach number and reduced frequency . . . 138

Nomenclature

Latin Symbols

a	Speed of sound
A	Blade surface area
c	Chord
$\boldsymbol{C}$	Damping matrix
C_p	Pressure coefficient
C'_p	Unsteady pressure coefficient
d_k	Discrete distance function
H	Plunge displacement amplitude
i	Incidence
$\boldsymbol{K}$	Stiffness matrix
k	Reduced frequency
k	Wavenumber
L	Lift
$\boldsymbol{L}$	Aerodynamic influence coefficient matrix
l	Twist axis setback
M	Moment
M	Mach number (magnitude)
M_x	Axial Mach number
M_θ	Circumferential Mach number
$\boldsymbol{M}$	Mass matrix
m_r	Modal mass
m	Nodal diameter
$\boldsymbol{n}$	Blade surface unit normal vector
N_b	Number of blades
p	Static pressure
p'	Instantaneous unsteady pressure
p_0	Total pressure
$\boldsymbol{q}$	Modal displacement vector
Re	Reynolds number
S	Pitch
t	Time
T	Temperature
T_0	Total temperature
V_∞	Free stream flow velocity
W	Aerodynamic work done per vibration cycle
$\boldsymbol{x}$	Physical displacement

x, y, z	Cartesian coordinates
x, r, θ	Cylindrical coordinates
z	Half-chord twist axis setback

Greek Symbols

α_P	Plunge vibration induced incidence
α_T	Twist vibration induced incidence
γ	Stagger angle
γ	Ratio of specific heat
δ	Logarithmic decrement
ζ	Aerodynamic damping ratio
η	Isentropic efficiency
θ_T	Twist angle amplitude
ξ	Plunge-twist incidence ratio
ρ	Density
σ_m	Inter-blade phase angle
ϕ	Phase of unsteady pressure
$\mathbf{\Psi}$	Physical mode shape matrix
$\mathbf{\Phi}$	Mass normalised mode shape matrix
ω	Angular frequency
ω_d	Damped angular frequency
Ω	Rotor shaft speed

Abbreviations

1F	1$^{\text{st}}$ flap mode shape
1T	1$^{\text{st}}$ torsion mode shape
2F	2$^{\text{nd}}$ flap mode shape
AIC	Aerodynamic influence coefficient
CFD	Computational fluid dynamics
EO	Engine order
FEA	Finite element analysis
IBPA	Inter-blade phase angle
LE	Leading edge
NACA	National Advisory Committee for Aeronautics
NC	Nodal circle
ND	Nodal diameter
NRBC	Non-reflecting boundary condition

NSV	Non-synchronous vibration
OGV	Outlet guide vane
TPR	Twist-plunge ratio
RANS	Reynolds-averaged Navier-Stokes
SA	Spalart-Allmaras
SDOF	Single degree of freedom
TA	Twist axis
TE	Trailing edge
TWM	Travelling wave mode
URANS	Unsteady Reynolds-averaged Navier-Stokes

Subscripts

P	Plunge
T	Twist

Superscripts

QS	Quasi-steady

1 Introduction

Modern aeroengine compressor designs strive to reduce weight and maintain high aerodynamic efficiency. The primary goal of initial compressor designs is therefore largely dictated by aerodynamic performance and weight loss requirements. The implementation of new features to achieve these goals poses issues for compressor aeroelastic stability. One design feature that is becoming common is manufacturing rotor disks and blades as a single component, called a blade-integrated disk, or 'blisk' [1]. These designs are favoured for their reduced weight and improved aerodynamics, but come with the penalty of decreased mechanical damping compared to traditional dovetail hub-blade contacts [2]. Even when blisks are not implemented, blades are becoming thinner to improve aerodynamics and reduce weight, but consequently have greatly reduced stiffness. This is accompanied by a trend of increased loading per stage, to either increase the overall pressure ratio or maintain an existing pressure ratio with a reduced number of stages. The decreased mechanical damping and increased loading mean there is an increased likelihood of many different types of aeroelastic instabilities throughout an aeroengine. A general overview of aeroelastic instabilities that occur in different components of a typical turbofan is shown by figure 1.1.

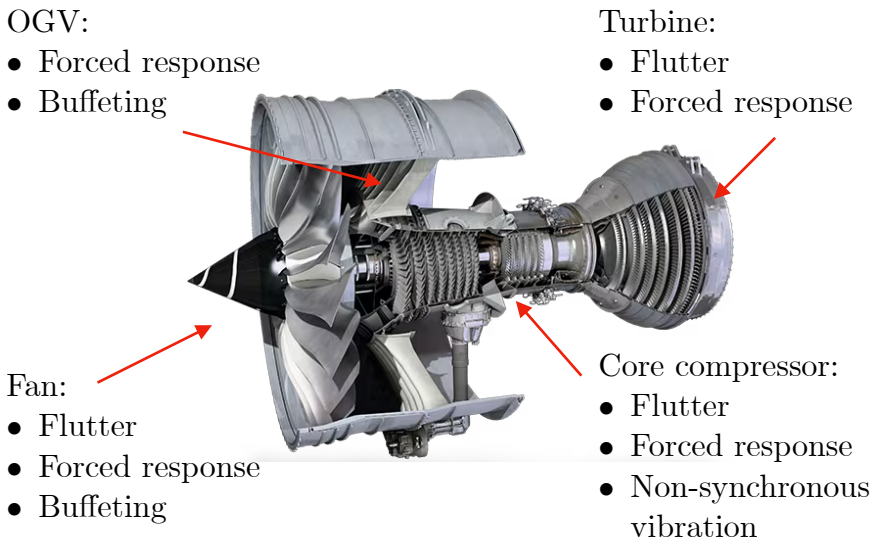


Figure 1.1: Summary of aeroelastic instabilities in a typical turbofan

The focus of this work is on an aeroelastic instability called flutter. Flutter is known to occur in many different dynamic structures, such as bridges

[3], wind turbines [4], and modern aero engines [5]. When flutter occurs, the vibration amplitude of the blades increases exponentially, which can lead to catastrophic failure of the structure. The aim for engine manufacturers is to design compressors that are flutter-free, or at least decrease the likelihood of flutter occurring in the typical operating envelope. To do so, the key flutter mechanisms must be understood and avoided in future designs.

When flutter occurs, the rotor blades of a compressor vibrate in a deterministic pattern called a mode shape. It has been shown that the first flap or 1F mode shape is particularly susceptible to flutter in compressors [6]. The 1F mode shape will differ based on the blade geometry and constraints of the system, such as mechanical damping at the root and part span shrouds. However, there are methods to define transferable properties of mode shapes for similar geometries. One such method is to assume that the mode can be considered a superposition of many simple 2D mode shapes defined along the span of the rotor blade. This final superposed mode is called a 'combined mode', which approximates the 1F mode shape. The most commonly implemented simple modes are plunge vibration, which occurs perpendicular to the chord; twist vibration about the elastic axis; and axial vibration parallel to the rotor axis. For 1F mode shapes, the axial component is often several orders of magnitude smaller than the plunge and twist vibration components and is frequently neglected. The 1F mode shape can then be defined by a ratio of the amplitudes of plunge and twist vibrations. For example, the modal amplitude of a 1F mode shape in the tip region of a modern fan blade may be described by 70% plunge amplitude and 30% twist amplitude.

The advent of increased computational speed in modern computer architectures means that high-fidelity CFD models can be used to model flutter in full-assembly multi-stage turbomachinery [7]. However, obtaining solutions for such cases is still rather slow and resource-intensive. Therefore, engine manufacturers look for methods to reduce the heavy computational expense. One method to do so is to investigate flutter using two-dimensional cascades. These implementations are beneficial as they provide physical insight into the mechanisms of flutter with a greatly reduced computational cost. In addition, due to their small overheads, these implementations can be used to define reduced-order models using data for a very large input parameter space, which is unfeasible for large CFD models in early design stages. The conclusions drawn from these models then allow engine manufacturers to implement design rules that, when applied to full-scale engine implementations, can help mitigate the likelihood of flutter.

2 Background

2.1 Blade-Disk Assembly Modes

Disk modes

The rotor disk is a component within a blade row of an axial flow compressor. The disk itself is typically annular in geometry, where the inner radius connects to the rotor shaft, which drives the rotation of the blade row, and the outer radius contains slots that house the individually manufactured blades. This component is purely structural and has no interaction with the flow through the compressor. The disk is not an infinitely stiff structure and will have its own modal content called 'disk modes'. The constraints of the structure are that the inner radius of the disk is fixed to the rotor shaft, while the outside radius is not constrained and is therefore free to vibrate. Figure 2.1 shows the displacement amplitude of the first six mode shapes for free vibration of a simple annular disk determined by MacBain [8].

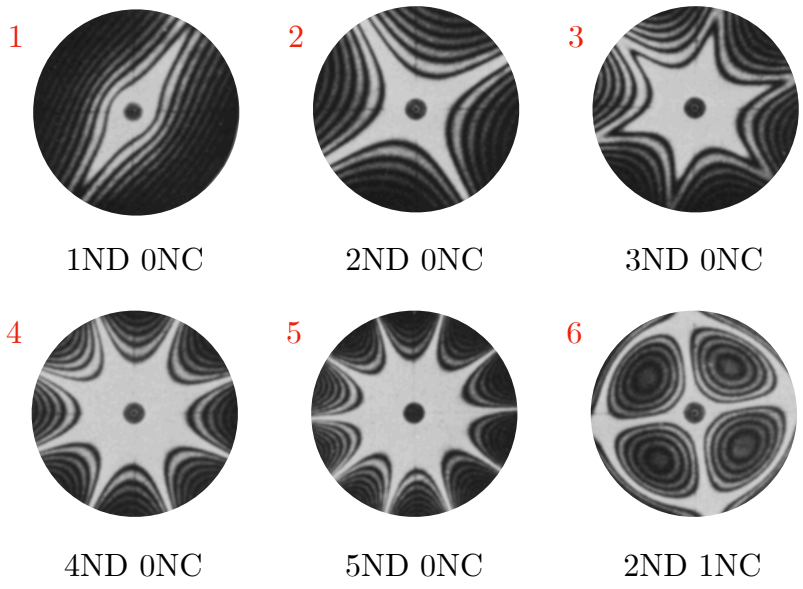


Figure 2.1: First six annular disk mode shapes [8]

The modes in figure 2.1 are ordered by increasing eigenfrequency. Regions of white indicate zero displacement amplitude, whereas regions shown in black indicate a large displacement amplitude. Annular disk mode shapes

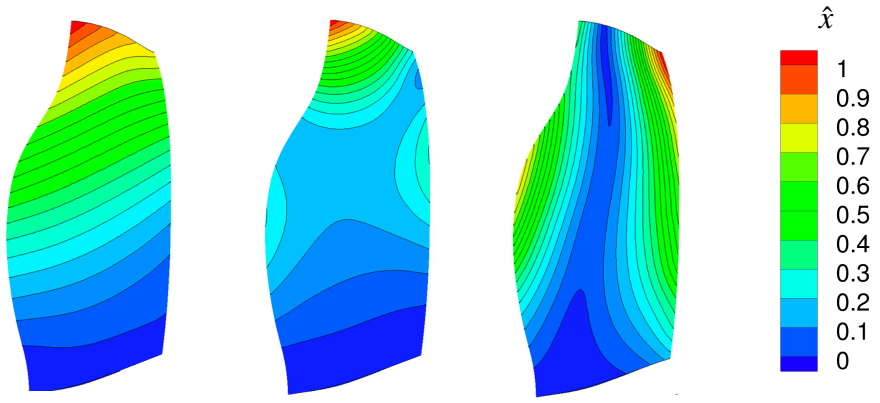
are typically categorised by the number of nodal diameters (ND) and nodal circles (NC). The number of nodal diameters is equal to the number of lines that pass through the diameter of the disk which have zero displacement. Whereas the number of nodal circles is the number of lines of constant radius with zero displacement. For example, mode two in Figure 2.1 has two lines of zero displacement passing through the diameter and can therefore be considered a 2ND disk mode. Additionally, disks may have both nodal diameters and nodal circles. This can be seen in mode six, which has two lines of zero displacement passing through the diameter and one line of constant radius with zero displacement and can therefore be classified as a 2ND–1NC disk mode. Nodal diameters are typically excited at much lower eigenfrequencies than nodal circles [9]. Figure 2.1 shows it takes up to the sixth disk mode to see the first nodal circle for this simple disk. For actual rotor blade disks, this mode number is likely to be significantly higher. For this reason, it is common to drop the number of nodal circles, which are commonly zero, and only reference the number of nodal diameters of the disk mode.

Blade Mode Shapes

The vibration mode shapes of the individual blades are called the 'blade modes', and exist independently of mechanical coupling with the rotor disk. It is often assumed that the hub-disk contact is infinitely stiff; therefore, the hub of the blade is constrained to have identical displacement to the outer annulus of the disk. Assuming the blades do not have part-span shrouds or are constrained at the tip, the structural constraints are similar to those of cantilevered beams and vibrate in similar mode shapes despite the complex geometries of modern blades. Figure 2.2 shows the normalised displacement amplitude, $\hat{x}$, of the first three blade mode shapes for free vibration of a typical fan blade [10]. The modes are ordered from left to right by increasing eigenfrequency. The first mode is the first 'flap' or 'bending' mode shape (1F), followed by the second flap (2F), and finally the first torsion (1T) mode shape.

Blade-Disk Assembly Modes

The blade-disk contact at the hub mechanically couples the individual blades in the row and the rotor disk. This combines the modal content of both the rotor disk, the blades, and additional components such as part span shrouds to create blade-disk assembly modes. These can be described by the modal content of the blade mode, followed by the disk mode. For



First Flap (1F) | Second Flap (2F) | First Torsion (1T)

Figure 2.2: First three fan blade mode shapes [10]

example, 1F–2ND is a disk mode with two nodal diameters and blades that are vibrating in a first flap mode shape, as shown for a transonic fan in figure 2.3. Effects such as mistuning of the rotor blades and additional structural constraints can make the description of the blade-disk assembly mode more complex [11].

For blade-disk assemblies, the nodal diameter of the disk mode can be used to determine the phase angle between adjacent blades in the row, under the assumption that the mode is cyclic symmetric. This angle is called the inter-blade phase angle, σ_m, and is defined as

$$\sigma_m = \frac{2\pi m}{N_b} \tag{2.1}$$

where m is the number of nodal diameters and N_b is the number of blades in the row. For a given blade row, the maximum number of nodal diameters is $(N_b-1)/2$ if N_b is odd and $N_b/2$ if N_b is even. The zeroth and maximum nodal diameters form single standing waves around the circumference. Whereas for all other nodal diameters, the vibration pattern creates a pair of travelling waves called 'double modes'. These modes have identical frequency and nodal diameter but form travelling waves that propagate in different directions around the annulus. The notation for these travelling waves is that forward travelling wave modes will travel in the same direction as the rotor, and backward travelling wave modes will travel in the opposite direction as the rotor. Nodal diameters for forward travelling wave modes are often signed

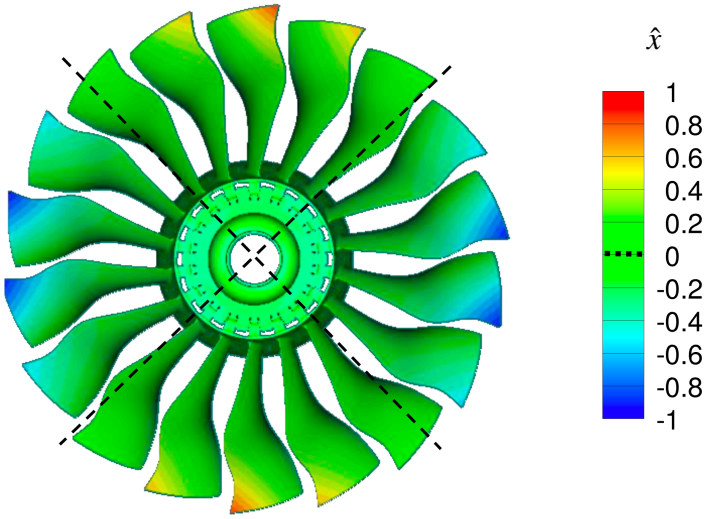


Figure 2.3: Expanded 1F-2ND blade-disk assembly mode for a transonic fan

positive, e.g., $m = +2$, and nodal diameters for backward travelling wave modes are signed negative, e.g., $m = -2$. The physical displacement of the mechanically coupled blades can be found by the relation

$$q_k(t) = \sum_{m=0}^{N_b-1} \hat{q}_m e^{i(\omega t + k\sigma_m)} \tag{2.2}$$

where $q_k(t)$ is the physical displacement of the kth blade in the row and $\hat{q}_m$ is the amplitude coefficient of the travelling wave mode. The definition of this relation is dependent on the system being tuned, meaning the modal content (natural frequency and mode shape) for each blade in the row is identical. It can be seen that the inter-blade phase angle fixes the phase difference for the vibration of the adjacent blades.

Reduced frequency and the quasi-steady limit

The eigenfrequency of the blade mode shape is often expressed non-dimensionally as the reduced frequency k

$$k = \frac{\omega c}{V_\infty} \tag{2.3}$$

where c is the chord length, V_∞ is the upstream relative velocity magnitude, and ω is the angular frequency. Frequently, semi-chord is used instead of the chord length due to its derivation from thin airfoil theory [12] and the vibration frequency instead of the angular frequency to better relate the reduced frequency to the convective length [6]. Physically, the reduced frequency is the ratio of the time taken for the flow to be convected a single chord length and the period of the oscillation cycle. For example, if $k = 0.5$, then the flow is convected $2\pi/(0.5) = 12.56$ chord lengths per oscillation cycle. The reduced frequency is therefore not only a measure of the frequency of the vibration but also of the unsteadiness of the flow due to this vibration. For $k \approx 0.05$, the flow is convected over large distances with respect to the chord, and the unsteady flow perturbations have less influence on the blade unsteady lift. Whereas for $k \approx 1$, the flow is convected over much shorter distances, and the unsteady flow perturbations have a greater influence on the blade unsteady lift. The limit of $k \to 0$ is known as the quasi-steady limit. In the quasi-steady limit, the perturbations in the flow are varying so slowly that they can be approximated as steady. In this limit, the blades are still vibrating, which means that the instantaneous aerodynamics are the same as those of a static aerofoil at the same angle of attack.

2.2 Rotor Blade Aeroelasticity

Aeroelasticity can be defined by Collar's aeroelasticity triangle [13], where the corners of the triangle represent inertial, elastic, and aerodynamic forces, as shown in figure 2.4. These three forcing types form the basis of all aeroelastic instabilities. Structural dynamics is associated with the interaction of inertial and elastic forces, stability and control with inertial and aerodynamic forces, and static aeroelasticity with aerodynamic and elastic forces. Finally, there is dynamic aeroelasticity, which includes the interaction of forcing from all three disciplines. The majority of turbomachinery aeroelastic instabilities fall into the category of dynamic aeroelasticity.

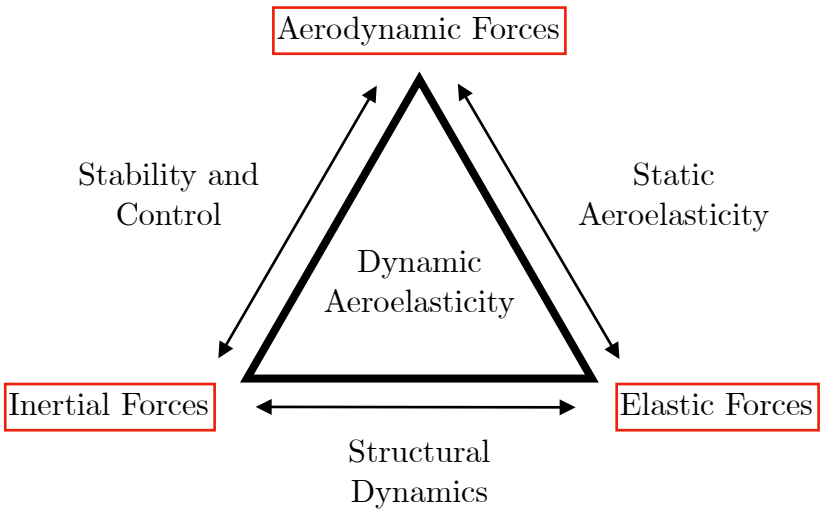


Figure 2.4: Collar's aeroelasticity triangle

2.2.1 Dynamic Aeroelasticity

Dynamic aeroelasticity can be defined by the general aeroelasticity equation shown in equation 2.4. Where $\mathbf{M}$, $\mathbf{C}$, and $\mathbf{K}$ are the mass, damping, and stiffness matrices respectively and $\boldsymbol{x}$ is the physical displacement vector. The aerodynamic forcing vector on the right-hand side of equation 2.4 has been split into two components: $\boldsymbol{f}_E$, which is due to external aerodynamic forcing and has many sources, and $\boldsymbol{f}_V$, which is self-excited forcing due to the vibration of the blades. This separation of forcing allows different types of aeroelastic stability to be assessed more clearly. This is discussed in more detail in the coming section. But for example, flutter calculations can be performed by setting $\boldsymbol{f}_E$, forced response by setting $\boldsymbol{f}_V$ and some instabilities require both forcing components.

$$\mathbf{M}\ddot{\boldsymbol{x}} + \mathbf{C}\dot{\boldsymbol{x}} + \mathbf{K}\boldsymbol{x} = \boldsymbol{f}_E + \boldsymbol{f}_V \tag{2.4}$$

Forced Response

Forced response occurs when the frequency of an unsteady aerodynamic response forms a resonant condition with the natural frequency of the assembly mode. Typically, this occurs when a rotor passes through a circumferentially non-uniform, often stationary flow field, which induces an unsteady aerodynamic loading at a frequency that is harmonic of the rotor shaft speed

[14]. Such harmonics are referred to as engine orders (EO). The resonant conditions can be identified on a Campbell diagram, as shown in figure 2.5, where the x axis is the rotor shaft speed and the y axis is the vibration frequency of the assembly mode or the excitation frequency. It shows that forced response occurs at the crossings of the frequency of the mode and a given engine order, indicating a resonant condition. With forced response, the aerodynamic unsteadiness is a pre-existing flow feature and does not require a self-excited forcing due to vibration of the blades. Therefore, $f_V = 0$ in equation (2.4) and

$$f_E = \sum_{n=0}^{\infty} c_n e^{in\Omega t} \tag{2.5}$$

where n is the harmonic of the shaft speed, c_n is the forcing amplitude, and Ω is the rotor shaft speed. Forced response is typically categorised as low engine order (LEO) or high engine order (HEO) [15]. High engine order forced response typically occurs when a rotor passes through wakes and potential flow from adjacent stators or struts. This type of response is particularly important as these effects are present in all stages of a multi-stage compressor, meaning forced response can occur throughout the entire engine. Low engine order forced response can occur in compressors and turbines but is more likely to occur in fan blades. For fan blades, inlet distortions such as ground vortex ingestion and cross-wind gusts induce low engine order responses [16] [17].

Non-Synchronous Vibration

Non-synchronous vibration (NSV) is an umbrella term used to describe any instability that does not occur at a harmonic of the rotor shaft speed. Although technically this includes instabilities such as flutter and acoustic resonance, this is not how NSV is placed in the literature. Typically for NSV, there is an inherent unsteady aerodynamic excitation in the flow that generates periodic unsteadiness at non-integral engine orders, which can be seen on the Campbell diagram in figure 2.5. The majority of the literature focuses on unsteady aerodynamics which occur when the compressor is operating near stall at a stable operating point, but there can also be non-integral responses at choke due to unsteady shock waves. If the frequency of the aerodynamic excitation and the blade's natural frequency are close, they can become 'locked in' to the structural frequency, resulting in large vibration amplitudes [18]. For this instability, it is predominantly the unsteady aerodynamics, rather than the blade vibration-induced aerodynamics, that drives

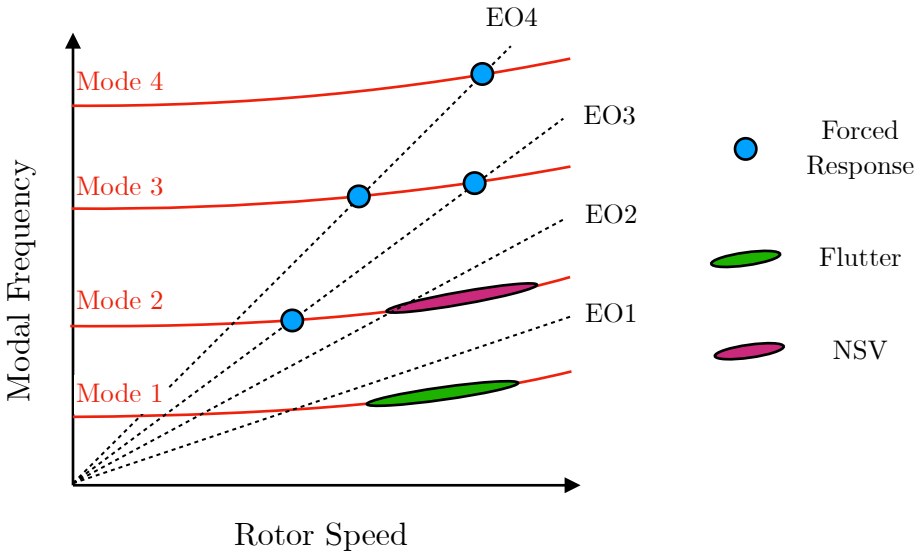


Figure 2.5: Campbell diagram showing different aeroelastic instabilities

the vibration. This distinguishes NSV from flutter, as the flow unsteadiness is not only due to blade vibration and cannot be described as linear. Sources of aerodynamic excitation include vortex shedding and buffeting [19].

Flutter

Flutter is a self-excited instability in which the unsteady aerodynamic response due to the blades vibration transfers energy into the mechanical structure [20]. If the flutter conditions are maintained, the vibration amplitude increases which can quickly lead to catastrophic engine failure. At the onset of flutter, a small initial displacement of the blade induces a change in the unsteady flow field, which in turn changes the unsteady blade aerodynamic loading. If this loading does work on the blade, then energy is transferred from the flow into the structure. This causes an increase in the blade vibration amplitude, which forms a positive feedback loop with the amplitude of the unsteady aerodynamic response. This process is unstable and causes exponentially increasing vibration amplitudes. However, if the unsteady blade aerodynamic loading does negative work (equivalent to the blade doing positive work on the flow), then energy is transferred from the blade to the flow, which damps the vibration response. This process is stabilising and causes exponentially decreasing vibration amplitudes. Figure 2.6 shows the displacement over time for the stable and unstable scenarios

posed above. The unsteady aerodynamic forcing is self-excited in nature. Whereby the only inherent unsteadiness in the flow is a result of the blades own vibration. Therefore, $f_E = 0$. Flutter is an inherently linear instability, but at large vibration amplitudes, non-linear effects may come into play due to unsteady propagating suction side separations.

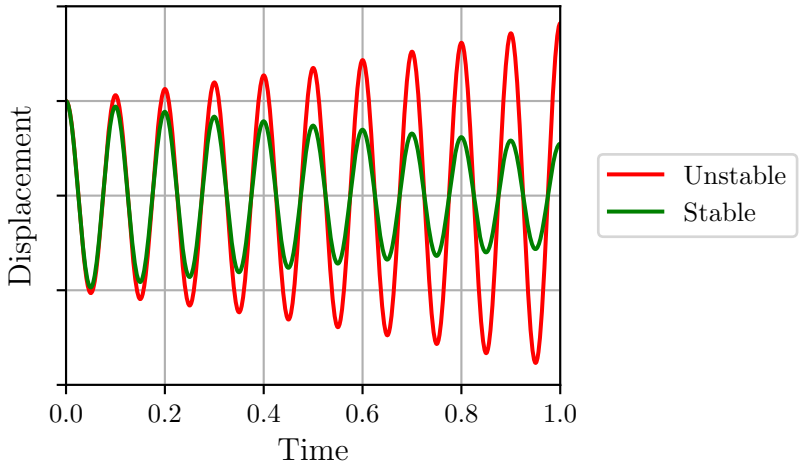


Figure 2.6: Physical displacement for stable and unstable cases of vibration induced work done on the blade surface

3 Literature Review

3.1 Types of Flutter

Many different types of flutter occur at different points on the compressor operating map, as shown by the work of Platzer and Carta in figure 3.1 [21]. Each of these types of flutter will have their own distinct mechanisms by which flutter occurs.

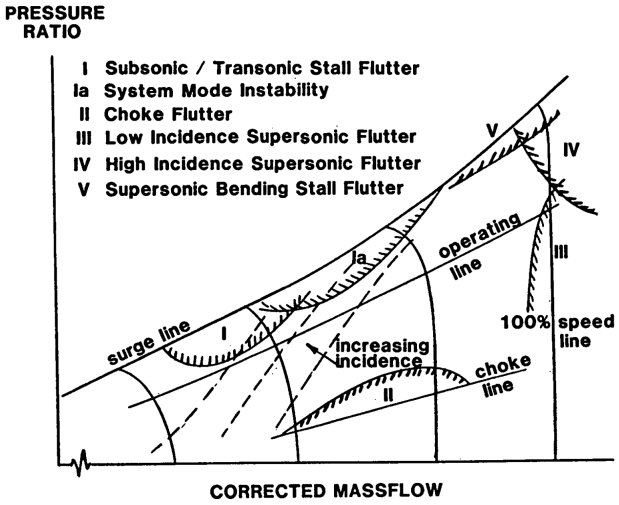


Figure 3.1: Regions of different flutter regimes on a compressor operating map [21]

The aim of this thesis is not to give an extensive overview of the mechanisms of different types of flutter in transonic compressors. But rather, isolate types of flutter that typically vibrate in 1F mode shapes, which can then be expressed as combined plunge-twist mode shapes. There are two main types of flutter which are most commonly associated with 1F mode shapes. These are subsonic stall flutter [22] and classical flutter [23].

Classical flutter is typically associated with the early work on combined mode shapes using simple, often two-dimensional cascades operating at zero incidence. In modern compressors, classical flutter does not pose a threat, as the structural dynamic design usually ensures that the blades are stiff enough to prevent coupling of the plunge and twist components [24]. The initiation of classical flutter does not require the stalling of the blades or the presence of shock waves and is thus able to occur in the vicinity of the working line.

While the name suggests that the blades are stalled, subsonic stall flutter can occur when the slope of the characteristic is negative. This phenomenon

is highly important to understand, as it is usually flutter, rather than stall or surge, which forms the limiting operating condition of the rotor. Subsonic stall flutter typically occurs at part speed near the stall line and is associated with shock wave movement, boundary layer separation, and radial flow migration on the suction surface driven by adverse pressure gradients.

An exhaustive list of the parameters that are critical for flutter in compressors was provided by Srinivasan [1]. Here, only the key literature relevant to subsonic stall flutter and classical flutter in 1F mode shapes is presented.

3.2 Influence of Mode Shape

The modal content of the blade-disk assembly is very important when discussing flutter stability. The majority of the literature shows that the first flap (1F) mode shape is most prone to flutter for fan blade stall flutter [25], flutter in core compressors [26], and classical flutter of cascades [23]. The first flap mode shape has the interesting property that it can be well approximated by a superposition of pure plunge motion perpendicular to the chord and pure twist motion about some elastic axis. These superposed approximations are referred to as 'combined modes'.

Plunge-twist ratio

Since the very earliest published literature, researchers have sought to investigate the effect of varying the amplitude ratio of the plunge and twist components on the flutter stability of combined modes. This was first conducted by Whitehead [27], who investigated the effect of varying the plunge-twist ratio of flat plates in cascade by defining a twist axis location. The twist axis location is defined as a chord-wise point downstream of the leading edge, about which the blades will vibrate as rigid bodies. Mode shapes with a twist axis location located close to the leading edge will be twist-dominated, but the twist axis location can be extended far downstream to implement a plunge-dominated mode. Whitehead showed that the most unstable twist axis location was at about 75% chord and that both the leading edge twist dominated modes and the plunge dominated modes were stable. The twist axis location method of Whitehead was adopted by Panovsky and Kielb [28] to investigate flutter stability for a two-dimensional turbine cascade. In this work, the combined mode also implemented an axial vibration component parallel to the blade chord, in addition to the plunge and twist components. In this work, the twist axis location was not constrained to chord-wise locations but could be located at any point on the two-dimensional plane of the turbine cascade. CFD was run for many twist axis locations on the

plane, and a tie-dye contour was built from the minimum aerodamping over all inter-blade phase angles. This method linearly interpolated the contributions from the individual mode shapes to build very large stability maps with minimal computational expense. It was concluded that a twist axis located on the aft portion of the aerofoil is most unstable, and a twist axis located near the leading edge is most stable. Whereas for plunge-dominated modes, the least stable torsion axes lie along the cascade axial direction rather than the cascade tangential direction. A different method for defining the twist-plunge ratio was defined by Halliwell [29] for clappered fan blades. Rather than defining an analytical mode shape using the definition of a twist axis location, Halliwell split an existing mode shape into its plunge and twist components. The twist-plunge ratio was defined as

$$TPR = \frac{c\theta_T}{\hat{H}} \tag{3.1}$$

where c is the blade chord, θ_T is the twist angle amplitude about the elastic axis, and $\hat{H}$ is the plunge displacement amplitude. While results were not stated about varying the twist-plunge ratio, Halliwell stated that it is likely that increasing the twist-plunge ratio is likely to create instability in the fan. This was based on previous work, such as that of Whitehead. The twist-plunge ratio definition of Halliwell was adopted by Vahdati and Cumpsty [6] for use in 1F flutter of a modern transonic fan. The twist-plunge ratio parameter, α, uses an identical implementation, except the chord c is replaced by the semi-chord, b, to better reflect the twist amplitude at the leading edge. In this work, it was described how the 1F mode shape can be decomposed into its plunge and twist components, as shown in figure 3.2. It was shown that by averaging the 1F mode shape at radial sections along the blade span, the plunge component of the mode shape can be obtained. To obtain the twist component, the plunge component is subtracted from the initial 1F mode shape. This not only defines the twist mode but also ensures that the plunge and twist components summate to reproduce the 1F mode. While the work of Vahdati and Cumpsty defined this parameter, the effect of varying the twist-plunge ratio on flutter stability was not investigated.

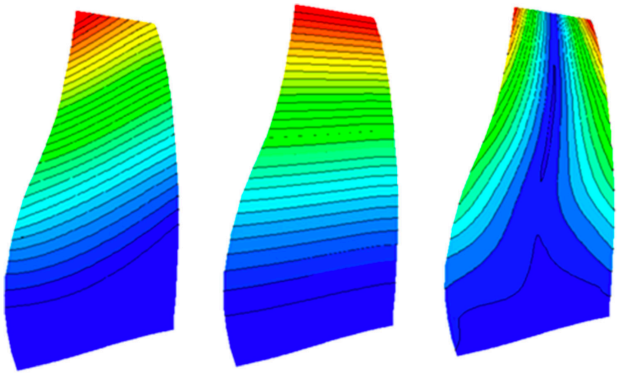


Figure 3.2: 1F mode split into its plunge and twist components [6]

Lee et al. [30] used the twist-plunge ratio parameter α and 1F mode splitting procedure of Vahdati and Cumpsty to investigate the flutter stability of a low-speed fan. In this work, modification of the mode is achieved by splitting the 1F mode into its plunging component and twisting component and then modifying the amplitude of the twist component of the mode. The new 1F mode shape is obtained by adding the plunge component to the modified twist component. It was shown that as the parameter α decreases (i.e., the percentage of twisting motion in the 1F mode shape is reduced), the aerodamping of the rotor increases, and hence the flutter margin of the rotor increases. Iseni et al. [31] also investigated the effect of varying α on the flutter stability of a highly loaded fan blade. It was shown that increasing α only began to modify the aerodamping at greater than 50% span of the blade. It was concluded that increasing α made larger changes to the throat area, which resulted in larger unsteady variations in shock strength, which destabilised the blade.

A novel method for expressing the work done per vibration cycle for a combined mode shape was determined by Kielb et al. [32] for a two-dimensional turbine cascade. In this work, plunge-twist-axial mode shapes made up the components of the combined mode. In this work, η is defined as the displacement amplitude of plunge vibration perpendicular to the chord, ξ as the displacement amplitude of vibration parallel to the chord, and α as the twist angle amplitude of twist vibration about the leading edge. A work done per vibration cycle matrix was defined as

$$b_l = \begin{bmatrix} W_{\xi\xi} & W_{\xi\eta} & W_{\xi\alpha} \\ W_{\eta\xi} & W_{\eta\eta} & W_{\eta\alpha} \\ W_{\alpha\xi} & W_{\alpha\eta} & W_{\alpha\alpha} \end{bmatrix} \tag{3.2}$$

where the diagonal terms represent the work done by the unsteady pressures acting on the mode shapes producing these unsteady pressures, and the off-diagonal terms represent the work done by the unsteady pressures generated by one vibration mode acting on a different mode. For example, $W_{\eta\eta}$ represents the work done by plunge motion induced unsteady pressures interacting with the plunge mode shape, and $W_{\eta\alpha}$ represents the work done by plunge motion induced unsteady pressures interacting with the twist mode. The total work done for any two-dimensional mode shape can then be calculated by

$$W = \{a\}^T [b_l] \{a\} \tag{3.3}$$

where

$$\{a\} = \begin{bmatrix} \xi \\ \eta \\ \alpha \end{bmatrix} \tag{3.4}$$

This shows that the total work done per vibration cycle can be expressed as the sum of the interactions of the individual components. A similar procedure was employed by Vahdati and Cumpsty [6], except in their definition, the interaction of the plunge and twist vibration induced unsteady pressures is considered to act to create a change in unsteady lift and unsteady moment. For example, $W_{\eta\eta}$ is replaced by the term $W_{P,L}$, which can be read as the work done due to plunge vibration induced unsteady lift. In either implementation, the generated work done is identical.

Inter-blade phase angle

In the majority of the literature, compressor blades are shown to flutter in low nodal diameter forward travelling wave modes [22]. However, there is very little explanation in the literature as to what the mechanism is between the nodal diameter and the flow that creates this destabilising condition. Jia et al. [33] investigated the effect of fan blade vibration mode on flutter stability, with an emphasis on the effect of nodal diameter. The components of the work done method developed by Kielb et al. was applied to explain observed trends in aerodamping. It was shown that the five aerodynamic

work coefficients related to the chord-wise mode ξ are much smaller in magnitude than the four components related to plunge and twist. It was shown that this is particularly true in low nodal diameter forward travelling wave modes, where the fan was most susceptible to flutter. It was hypothesised that the chord-wise vibration produced negligible work done compared to the other components, as the passage area variation for chord-wise vibration is significantly smaller. It was shown that the plunge motion induced work done $W_{\eta\eta}$ and $W_{\eta\alpha}$ was stable for all nodal diameters, and the twist motion induced work done $W_{\alpha\eta}$ and $W_{\alpha\alpha}$ was unstable for low nodal diameter forward travelling wave modes. In addition, the largest stabilising contribution was the work done by plunge vibration induced unsteady pressure interacting with the plunge mode $W_{\eta\eta}$ and the largest destabilising contribution was the work done by twist vibration induced unsteady pressure interacting with the plunge mode $W_{\alpha\eta}$ in low nodal diameter forward travelling wave modes, where flutter occurs. Dong et al. [34] investigated the effect of inter-blade phase angle on a high-speed wide-chord transonic fan. In this work, a passage area change coefficient was defined. Application of this parameter showed that larger inter-blade phase angles gave rise to more dramatic changes in the passage area. This resulted in a phase change and an increase in the unsteady pressure amplitude, which gave a large positive aerodynamic damping. Additionally, it was stated that the shock wave structure on the suction side is highly dependent on the inter-blade phase angle, and this change in structure changes the aerodamping.

Reduced frequency

It has long been known that the eigenfrequency of the blade mode is critical for flutter stability [27]. Frequently in the literature, the eigenfrequency is expressed non-dimensionally as either the reduced frequency or the reduced velocity, where one is simply the reciprocal of the other. It was shown in the early works of Sisto [35] that flutter in pure bending modes occurs at large critical flutter reduced velocities (or low reduced frequencies) for two-dimensional stall flutter in cascades. A similar conclusion was drawn by Carta [36] for two-dimensional cascades at zero incidence vibrating in combined plunge-twist mode shapes. Zhao [37] investigated the effect of reduced frequency on flutter stability for flat plates at zero incidence in an inviscid flow field. It was shown that at high reduced frequencies, the aerodamping tends to zero as the blades become too stiff to be affected by the flow, and that flutter can occur at low reduced frequencies but is highly dependent on the twist-plunge ratio. Zhao also implemented the splitting of the mode

shape into work done components, as implemented by Vahdati and Cumpsty. These components were then plotted as a function of reduced frequency for the same twist-plunge ratio. It was shown that the work done due to plunge vibration induced unsteady lift had a large stabilising contribution for all reduced frequencies, whereas the largest destabilising contribution came from the work done due to twist vibration induced unsteady lift. The work done by either vibration mode generating an unsteady moment was very small compared to the other two components.

The effect of reduced frequency becomes more complex when the upstream and downstream acoustic waves become cut on. It was shown by Vahdati and Cumpsty [6] that flutter occurs in a very narrow frequency range, which is defined by the range where the upstream acoustic wave is cut on, and the downstream acoustic wave is cut off. It was determined that the swirl imparted downstream is the reason for the difference between the upstream and downstream cut on frequency. This work showed that there are no monotonic trends in the aerodamping as a function of vibration frequency. In this paper, the calculations performed are for the fan only, and there is no reflection of the acoustic waves from the fan intake, downstream OGV, or the inlet and outlet boundaries of the domain. It was stated that the downstream wave being cut off causes the downstream circumferential travelling pressure wave to propagate up the passage and interact with the flow near the shock, and this interaction with the shock is destabilising.

However, it appears from the literature that this is dependent on the geometry, operating point, and twist-plunge ratio. It was shown by Huang [38] that flutter occurs at frequencies where the upstream acoustic wave is cut on and the downstream acoustic wave is cut off. But flutter was shown not to be bound by the limits of the cut on frequencies, as shown in figure 3.3. Huang theorised that this discrepancy is due to the difference in twist-plunge ratio between the two cases, although this was not validated in this work.

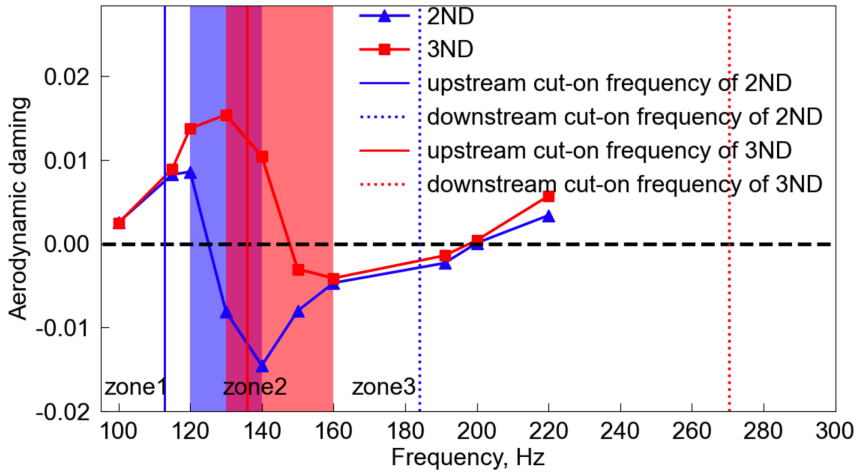


Figure 3.3: Aerodamping as a function of blade mode frequency

Stability maps

There are several instances in the literature of authors plotting the modal parameters of twist-plunge ratio, reduced frequency, and nodal diameter on a single figure called a 'stability map'. One of the first to do so was Carta [36]. In this work, the reduced velocity $V_\infty/\omega b$ was plotted against the twist-plunge deflection ratio defined by α/H as shown in figure 3.4. For this case, the points marked 'flutter' and 'stable' are determined by experiment, and the flutter stability limit, which for this case shows the location where the logarithmic decrement δ is zero, is determined by theory for a single airfoil. This shows that modes with a high reduced velocity (low reduced frequency) and a large twist-plunge ratio are most susceptible to flutter. It can also be seen that the flutter stability limit follows the trend of an offset rectangular hyperbola of these two parameters.

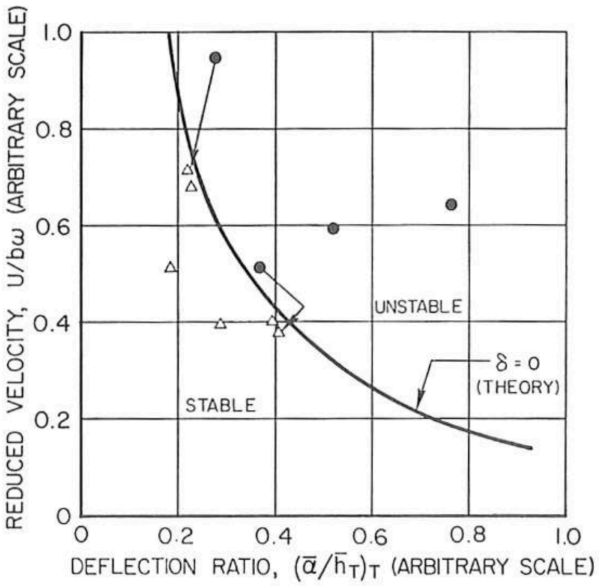


Figure 3.4: Flutter stability map produced by Carta [36]

A similar conclusion that the flutter stability limit can be defined by a rectangular hyperbola of twist-plunge ratio and reduced velocity was proposed by Halliwell [29] for clappered fan blades. It has been previously stated that Halliwell defined a twist-plunge ratio as $c\theta_T/\hat{H}$. This was further expanded by the inclusion of the reduced frequency k to produce a flutter stability parameter defined as

$$\xi_H = \frac{c\theta_T}{k\hat{H}} \tag{3.5}$$

Halliwell plotted a stability map of reduced velocity and twist-plunge ratio for several nodal diameters and showed that the flutter stability limit can be defined by lines of constant ξ_H. It was advised that the fan blades should be designed to have smaller twist-plunge ratios in order to prevent flutter, as the gradient of the aerodamping with respect to the twist-plunge ratio is greater than the gradient with respect to the reduced velocity. Nipkau et al. [39] defined a stability map as a function of 'plunge-twist ratio' and reduced frequency for three different modern fan blade designs. It showed that design A, which had the highest plunge-twist ratio of the three modes, was the only flutter stable design when operating at part-speed operating conditions near stall. A stability limit is presented, which shows a similar rectangular hyperbolic shape of the stability limit as in the previous works

but cannot be effectively defined as the stated 'plunge-twist ratio' is not defined mathematically.

3.3 Influence of Aerodynamics

When a compressor is throttled at a constant rotational speed, the mass flow rate decreases and the total pressure ratio increases. This results in an increase in the flow incidence on the blades. As a result, the shock front moves towards the leading edge and increases in strength. The increased shock strength causes the boundary layer downstream of the shock front to thicken. Towards the stall line, where the adverse pressure gradient is largest, the boundary layer on the suction side can separate. In the region just after the shock front on the suction side, there is a low axial flow velocity, which results in a centrifuging of the flow radially towards the tip, which is commonly referred to as 'radial flow migration'. The streamlines of the flow near the stall boundary are therefore very different compared to those near the working line, where the streamlines have an approximately constant radial height. This change in shock structure, state of the boundary layer, and radial flow migration is known to affect flutter stability.

Mass flow rate

As was just mentioned, decreasing the mass flow rate at constant rotational speed results in stronger shocks, shock-induced separations, and radial flow migration. In the early work on flutter using two-dimensional cascades, these effects were compared to a change in the incidence of the flow on the blades.

It was shown by Vahdati and Cumpsty [6] that decreasing the mass flow rate at constant rotational speed caused flutter to occur for a typical transonic fan operating at part-speed. Similar results have been shown for different fan blade designs [40] and validated experimentally [41]. The components of the aerodamping were investigated by Vahdati and Cumpsty, as shown in figure 3.5. The conclusion drawn in this paper is that the aerodamping due to plunge and twist vibration induced moments is small and mostly cancel, and that the drop in aerodamping is largely determined by the interactions with the unsteady lift. In this case, it was shown that the aerodamping for high mass flow rates is dominated by the aerodamping due to plunge vibration induced unsteady lift. Critically, the aerodamping at low mass flow rates, where the aerodamping is less than zero, is dominated by the aerodamping due to twist vibration induced unsteady lift.

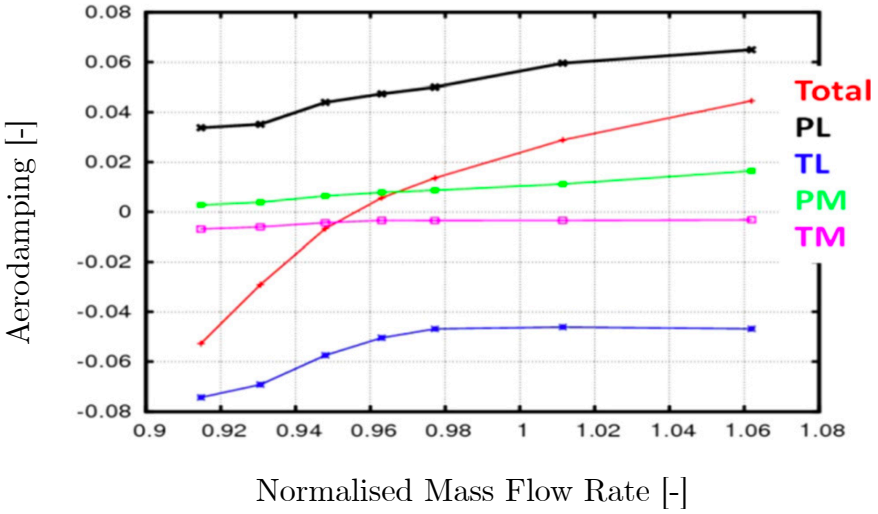


Figure 3.5: Components of work done per cycle as a function of mass flow rate [6]

It has been established for a long time in two-dimensional cascades that increasing the incidence on the blade row results in flutter [35]. Although there have been some contentious papers produced on the effect of steady aerodynamic loading. For example, it was shown by Smith and Kadambi [42] that for torsional flutter of a simple two-dimensional cascade, increasing the mean flow incidence on the blade is stabilising. This is quite contrary to almost all the literature on the topic. Although perhaps this suggests that there is some dependency on blade geometry.

Rotational speed

Subsonic stall flutter typically occurs at part-speed in narrow speed ranges on the compressor operating map. At these speed ranges, the unstable aerodamping near stall produces a stability limit that takes a 'bite' out of the compressor's operating map. Hence, the speed range over which flutter occurs is referred to as 'flutter bite' [43]. The speed range where flutter bite is most commonly seen in transonic fans is when the tip relative Mach number is close to 1 [6] [40]. Vahdati et al. [25] showed that flutter bite at part-speed operating conditions can occur without acoustic reflections for a transonic fan. Flutter of this kind is referred to as 'blade-only' flutter. An arbitrary

high working line was defined near the stall line, and the aerodamping was calculated for many rotational speeds. Figure 3.6 shows the aerodamping as a function of rotational speed as determined by [25]. It states that the minimum aerodamping at 77.5% speed is caused by the interaction of the mode shape and the shock-induced flow separation. The separation downstream of the shock front is destabilising as the phase of unsteady pressure shifts in this region. At higher speeds, there is a shock at approximately half-chord, but the higher axial velocity means the flow remains attached. Since the flow remains attached, there is no phase change, and consequently the aerodamping is positive. At lower speeds, the flow is subsonic and separates on the suction side. However, the aerodamping at this point is also stable, as the separation is not strong enough to induce a large enough phase change to make the blade unstable.

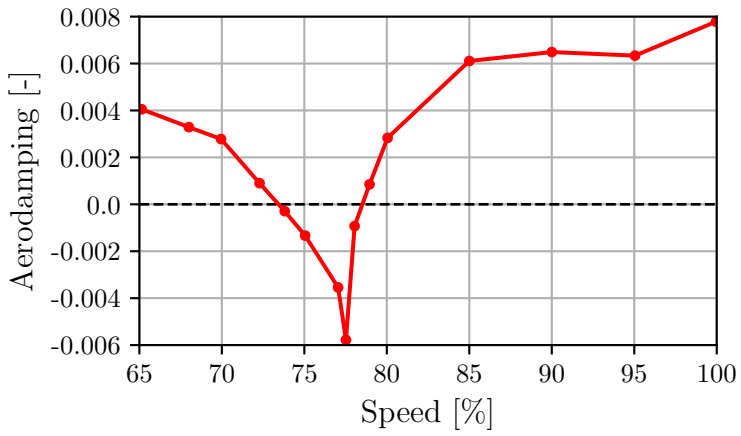


Figure 3.6: Aerodamping as a function of rotational speed

Shock structure

It is clear that at off-design operating points, the structure of the shock is very important. Vahdati et al. [25] showed that the supersonic pre-shock region was stabilising, whereas the post-shock separation was destabilising for a typical transonic fan blade vibrating in a 1F mode shape. This comparison was conducted at approximately 70% span. This work showed the effects of the shock by relating the unsteady pressure upstream and downstream of the shock to the blade velocity deduced from the mode shape vector. In the supersonic pre-shock region, the unsteady pressure is out of phase with the blade velocity, which is stabilising, whereas the unsteady pressure in

the post-shock separation region is in phase with the blade velocity, which is destabilising. Since the mode shape is similar, given the close proximity either side of the shock, it is concluded that the shock and the associated flow separation is destabilising due to the change in the phase of unsteady pressure. However, this does not seem to be a universal trend in the literature. While some works agree with that of Vahdati et al. [44] [45], other works appear to show the opposite trend. For example, Isomura and Giles [46], Huang et al. [38] and Aotsuka and Murooka [47] all showed that the supersonic pre-shock region is destabilising and the post-shock separation is stabilising. Therefore, the structure of the shock and flow separation and the interaction with the mode shape is geometry and operating point specific.

Radial flow migration

It was hypothesised in the literature that the radial flow migration was responsible for the phase lag in the separated region downstream of the shock. Rendu et al. [44] decomposed the mode shape into ten panels along the span of a modern fan blade. By vibrating each of the panels individually, the effect of the interaction of the flow and vibration of each panel was investigated. It was shown that vibration of the panel at approximately 65% span was by far the least stable radial level, despite the fact that the minimum aerodamping for the entire blade occurred at 90% span. It was noted that the vibration of this panel leads to oscillations of the whole shock, which radially propagate unsteady pressure fluctuations towards the tip. They concluded that radial flow migration is a key ingredient for flutter, and two-dimensional analysis of a three-dimensional fan blade near stall is not possible.

3.4 Influence of Aeroacoustics

It was shown by Giles [48] that the roots of the Euler equations which describe unsteady, inviscid and compressible flow can be expressed by three unsteady perturbations: an entropic wave, a vortical wave, and acoustic waves. Where the entropic wave carries perturbations in density, the vortical wave carries perturbations in vorticity, both of which are convected by the flow. On the other hand, the solution of the acoustic waves produces perturbations in density, velocity, and pressure, which propagate both with the convected flow and against the convected flow. Therefore, the vibration of the blades in a compressor can excite upstream and downstream acoustic waves. The propagation of acoustic waves in annular ducts has been extensively studied for cases with no mean flow [49], rigid body or 'wheel' flow [50] and non-uniform mean flow [51]. For the no mean flow case and rigid body flow, the pressure

perturbations are eigenfunctions consisting of combinations of Bessel functions. When there is non-uniform mean velocity, the eigenfunctions cannot be expressed in terms of standard functions but can be determined numerically via a process called 'wave-splitting'. When the eigenvalues are known, it can be determined whether the upstream and downstream acoustic waves are 'cut-on' or 'cut off'. Zhao [24] showed that for subsonic rigid body flow, the axial wavenumber can be defined by

$$k_x = \frac{-M_x\left(k - M_\theta \frac{m}{r}\right) \pm \sqrt{\left(k - M_\theta \frac{m}{r}\right)^2 - k_{r\theta}^2\left(1 - {M_x}^2\right)}}{1 - {M_x}^2} \tag{3.6}$$

where M_x and M_θ are the axial and circumferential Mach numbers, m is the nodal diameter, $k_{r\theta}$ is the radial-circumferential wavenumber, and k is the free stream wavenumber. When the axial wavenumber is complex, axially propagating acoustic waves decay exponentially and are defined as cut-off. Whereas, if the axial wavenumber is real, then acoustic waves can propagate axially in the duct. It was shown by Vahdati et al. [25] that there must be a clear distinction between 'acoustic flutter' and 'blade only flutter'. Acoustic flutter is driven by the reflection of upstream propagating acoustic waves from the fan intake face, while blade flutter is driven by shock-induced flow separation. Acoustic flutter also does not require stalling of the blades and can occur in the vicinity of the working line. It was also shown that the axial distance between the fan face and a 'bump feature', which fixed the location of the wave reflection, is critical for determining acoustic flutter, as this distance modifies the phase of the reflected pressure wave. Zhao [26] showed similar results for flutter in an embedded blade row of a high-pressure compressor. It was concluded that the distance to upstream and downstream stators was critical for setting the phase of the reflected pressure wave and that the most unstable condition is when the reflected wave lags the outgoing wave by 90°. Additionally, it was shown that reflections can also occur off the inlet and outlet boundaries, and particular care should be taken when specifying the distance to the computational boundaries and the axial mesh density near the boundaries. Zhao expanded this work and developed a simple analytical model to detect intake reflection-induced flutter of fan blades [43]. In some cases, it has been shown that acoustic flutter occurs at significantly higher frequencies than blade-only flutter [52], while others suggest that the effects of blade-only flutter and acoustic flutter can be concurrent [25]. In some cases, it is desirable to investigate the effects of just the blade-only flutter. It was shown by Colonius et al. [53] that the implementation of a 'sponge layer' in the inlet and outlet ducts can effectively mitigate reflections from the inlet and outlet boundaries. It was stated that

when a wave with a wavelength smaller than the local axial mesh size enters the inflated mesh, its amplitude is dissipated to reduce and even eliminate numerical reflections. This work was applied in addition to the non-reflecting boundary conditions of Giles [48].

3.5 Turbulence Modelling

Turbulence modelling is required to provide closure to the Reynolds average Navier-Stokes (RANS) equations. By far the most common turbulence model for turbomachinery applications is the Spalart-Allmaras (SA) turbulence model [54]. However, the original Spalart-Allmaras implementation has been shown to stall prematurely and predict larger regions of separation than expected compared to experimental validation due to an increased blockage in the passage. A portion of this thesis will be to determine flow features near stall, therefore, correctly modelling the flow in this region is critical. Lee et al. [55] derived a modified SA model based on the work of Liu et al. [56] and Li et al. [57]. Liu et al. altered the turbulence production to increase in regions of high helicity (SA-H), whereas Li et al. introduced the adverse pressure gradient into the production term to correct the overprediction of the flow separation in the original SA model (SA-PH). Lee et al. combined the effects of both and created the SA-PGH turbulence model. Figure 3.7 shows the improvement in the stall margin of the SA-PGH model compared to the original SA model implementation for a modern fan blade taken from the work of Lee et al. [55].

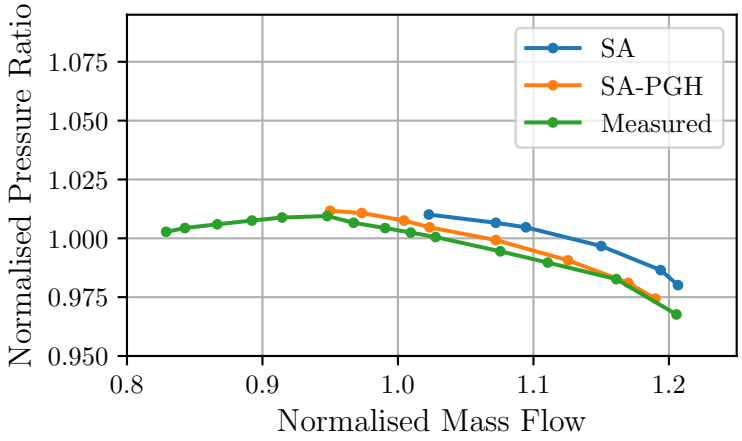


Figure 3.7: Constant speed characteristic for the original SA model and the modified SA-PGH model of Lee [55]

4 Objectives

The aim of this thesis is to improve the understanding of flutter in combined plunge-twist mode shapes. The core of this thesis places specific emphasis on understanding the physics of the interaction of flow and mode shape, which leads to flutter, with the aim of developing design rules that can be used by engine manufacturers in the early stages of the design process. This will be achieved by investigating the effect of different flow and modal parameters on the flutter stability of compressor cascades.

Many investigations into modal parameters such as plunge-twist ratio, reduced frequency, and nodal diameter have predominantly relied on computational simulations, with limited experimental validation across a wide range of input parameters. To address this gap and to ensure the validity of the conclusions drawn in the literature, both computational and experimental methods are employed to investigate the effect of these parameters on the flutter stability of a compressor cascade.

It has been shown in the literature that the effect of modal parameters on flutter stability can be best summarised as a stability map. Such maps allow designers to identify regions where flutter is likely to occur as a function of the input parameters. Designers are particularly interested in the location of the stability limit, which must be moved to ensure flutter-stable designs. However, there has been little work investigating the reasoning behind the location of this flutter limit; rather, most works simply state its location and develop design rules based on these findings. This is a reasonable conclusion, but it does not fully explain the mechanisms at play that produce the shape and location of the flutter limit.

The previous chapters showed that the operating point and steady aerodynamic loading are critical for determining compressor blade stall flutter. In the literature, the majority of the work investigating the effect of operating point and steady loading is for three-dimensional rotating compressor geometries or very old cascade implementations that used low-fidelity CFD. This presents an opportunity to investigate the effect of steady aerodynamic loading on flutter stability for a highly loaded two-dimensional compressor cascade. This maintains the low computational cost of two-dimensional cascades but implements the high loading of a transonic compressor. The results from the two-dimensional cascade implementation can then be compared to results for three-dimensional rotating compressors from the literature to identify similarities and differences in the results. If designers are to continue to use simple 2D cascades, it is important to understand the benefits and limitations of the implementation.

Therefore, the objectives of this thesis are to

1. Determine the effect of plunge-twist ratio, reduced frequency, and nodal diameter on the flutter stability of a two-dimensional cascade using experimentally validated CFD.

2. Develop a flutter model to physically explain the location of the stability limit based on the results from the parametric study of the modal variables.

3. Determine how the inlet Mach number and flow incidence affect flutter stability of a highly loaded two-dimensional compressor cascade.

5 Methodology

5.1 Flow Solver

The flow solver used throughout this thesis is a three-dimensional, compressible, unsteady Reynolds-averaged Navier-Stokes (uRANS) solver [58]. Turbulent closure is provided by a modified one-equation Spalart-Allmaras turbulence model. The modification better predicts the flow behaviour near stall by scaling the source term based on the local pressure gradient and the velocity helicity of the flow [55]. The equations are solved using a finite volume method, in which the domain is discretised using unstructured grids. The flow variables are stored at the vertices of the grid, and the fluxes are calculated using a highly efficient edge-based data structure. The inviscid and viscous fluxes are evaluated using Roe's flux vector difference splitting to provide matrix artificial dissipation in a Jameson-Schmidt-Turkel (JST) scheme [59]. The overall solution is second-order accurate in time and space. Steady-state solutions are obtained using the RANS method with local time-stepping and residual smoothing to accelerate convergence. The solver implements viscous wall functions to model the flow near the wall. This solver has frequently demonstrated its capabilities to successfully model off-design turbomachinery flows [22] [60] [61].

5.2 Structural Model

The fluid-structure model used throughout this work is 'weakly coupled'. For this implementation, the blade mode shapes and natural frequencies are first found by solving a free vibration problem for a single blade at the shaft speed and temperature of interest. This is typically conducted using structural finite element analysis (FEA). Then, the physical displacement of the blade is expressed as the product of the mode shape matrix and a single modal displacement vector, which converts the equations of motion into modal space. This limits the vibration of the blades to pre-specified linearised mode shapes and natural frequencies. At each time step, the aerodynamic forces are input into the equations of motion, and a system of linear equations is solved to determine the physical displacements for the next time step. The mesh is then deformed accordingly by a spring analogy algorithm [62], and the flow solver iterates to the next time step. This method is simpler, faster, and less computationally intensive than fully coupled solvers, which iterate between the flow solver and a separate structural FEA model at each time step. Additionally, this method allows specific mode shapes to be examined at different points along a constant speed characteristic without a change in

the aerodynamic forcing causing the excitation of a different mode shape. This means that the aeroelastic solver can be used more like a parametric study, which is highly beneficial for understanding the mechanisms behind different aeroelastic instabilities.

The equations of motion for damped forced vibration can be described by the general aeroelasticity equation as shown in equation 5.1

$$\mathbf{M}\ddot{\boldsymbol{x}} + \mathbf{C}\dot{\boldsymbol{x}} + \mathbf{K}\boldsymbol{x} = \boldsymbol{f} \tag{5.1}$$

where $\mathbf{M}$, $\mathbf{C}$, and $\mathbf{K}$ are the mass, damping, and stiffness matrices respectively; $\boldsymbol{x}$ is the physical displacement vector; and $\boldsymbol{f}$ is the aerodynamic forcing vector. The force vector can be split into two parts: the normal pressure force and the tangential viscous shear force. Throughout this work, the viscous shear force will be neglected, as it is typically several orders of magnitude smaller than the normal pressure force. For the weakly coupled fluid-structure solver, the natural frequencies and mode shapes must first be found for free vibration where $\boldsymbol{f} = 0$. It is assumed throughout this work that the mechanical damping is zero, therefore $\mathbf{C} = 0$. This simplifies equation 5.1 to a structural eigenvalue problem of the blade-disk assembly.

$$\mathbf{M}\ddot{\boldsymbol{x}} + \mathbf{K}\boldsymbol{x} = 0 \tag{5.2}$$

$$\boldsymbol{x} = \hat{\boldsymbol{x}}e^{i\omega t} \tag{5.3}$$

$$\mathbf{A} = \mathbf{M}^{-1}\mathbf{K} \tag{5.4}$$

$$\left[\mathbf{A} - \omega^2\mathbf{I}\right]\hat{\boldsymbol{x}} = 0 \tag{5.5}$$

The solution of equation 5.5 returns n system eigenvalues (natural frequencies ω_n) and eigenvectors (mode shapes $\boldsymbol{\Psi}_n$). Typically, the mode shapes are expressed in units of metres, which must first be mass normalised. Mass normalisation simplifies the equations of motion by modifying the mode shape vector so the modal mass is equal to unity. Let $\boldsymbol{\Psi}$ be a chosen physical mode shape with units metres and m_r be the modal mass. The mass normalised mode shapes $\boldsymbol{\Phi}$ can be found as

$$m_r = \boldsymbol{\Psi}^T\mathbf{M}\boldsymbol{\Psi} \tag{5.6}$$

$$\boldsymbol{\Phi} = \frac{\boldsymbol{\Psi}}{\sqrt{m_r}} \tag{5.7}$$

where the mass normalised mode shapes have units ($mkg^{-\frac{1}{2}}$). To begin the transformation into modal space, the physical displacement vector, $\boldsymbol{x}$, in equation 5.1 is expressed as the product of the mode shape vector and the modal displacement vector.

$$\boldsymbol{x} = \boldsymbol{\Phi q} \tag{5.8}$$

Substituting equation 5.8 into equation 5.1 and pre-multiplying by the transpose of the mode shape matrix gives

$$\boldsymbol{\Phi}^T \mathbf{M} \boldsymbol{\Phi} \ddot{\boldsymbol{q}} + \boldsymbol{\Phi}^T \mathbf{C} \boldsymbol{\Phi} \dot{\boldsymbol{q}} + \boldsymbol{\Phi}^T \mathbf{K} \boldsymbol{\Phi q} = \boldsymbol{\Phi}^T \boldsymbol{f} \tag{5.9}$$

The equations of motion can be simplified further by exploiting the orthogonality properties of the mass, stiffness and damping matrices with respect to the mass normalised mode shape vectors.

$$\boldsymbol{\Phi}^T \mathbf{M} \boldsymbol{\Phi} = \mathbf{I} \tag{5.10}$$

$$\boldsymbol{\Phi}^T \mathbf{C} \boldsymbol{\Phi} = \text{diag}\left(2\zeta_i \omega_i\right) \tag{5.11}$$

$$\boldsymbol{\Phi}^T \mathbf{K} \boldsymbol{\Phi} = \text{diag}\left(\omega_i^2\right) \tag{5.12}$$

$$\ddot{\boldsymbol{q}} + \text{diag}\left(2\zeta_i \omega_i\right) \dot{\boldsymbol{q}} + \text{diag}\left(\omega_i^2\right) \boldsymbol{q} = \boldsymbol{\Phi}^T \boldsymbol{f} \tag{5.13}$$

Here $\boldsymbol{\Phi}^T \boldsymbol{f}$ is the modal force vector and ζ is the aerodynamic damping ratio. The modal force for a single blade can then be written as

$$\Phi^T f = \int p \boldsymbol{n} \cdot \boldsymbol{\Phi} dA \tag{5.14}$$

where p is the static pressure, $\boldsymbol{n}$ is the blade surface unit normal vector, and dA is the infinitesimal area. The equations of motion are advanced in time using the unconditionally stable, second-order accurate Newmark-Beta method [63].

5.3 Method of Flutter Computation

The main parameter used to determine whether a blade will flutter is the aerodynamic damping ratio, or 'aerodamping'. When the aerodamping ratio is greater than zero, the blade vibration is damped, and the amplitude will

decrease exponentially over successive vibration cycles. This feedback mechanism is stable and will not result in flutter. Whereas when the aerodamping ratio is less than zero, vibration amplitudes will increase exponentially, resulting in flutter. In this thesis, two methods are used to calculate the aerodamping ratio.

1. Aerodynamic influence coefficient method.
2. Work done method.

5.3.1 Aerodynamic Influence Coefficient Method

The aerodynamic influence coefficient (AIC) method [64] linearly combines the influence of forcing on a blade due to its own vibration as well as propagating disturbances from neighbouring blades. Let the forcing terms of the right-hand side of equation 5.13 be defined by the product of the influence coefficient matrix $\boldsymbol{L}$ and the modal displacement vector $\boldsymbol{q}$.

$$\boldsymbol{\Phi}^T \boldsymbol{f} = \boldsymbol{L}\boldsymbol{q} \tag{5.15}$$

$$\boldsymbol{L}\boldsymbol{q} = \begin{bmatrix} \hat{L}_0 & \hat{L}_{N-1} & \hat{L}_{N-2} & \dots & \hat{L}_1 \\ \hat{L}_1 & \hat{L}_0 & \hat{L}_{N-1} & \dots & \hat{L}_2 \\ \vdots & \vdots & \vdots & & \vdots \\ \hat{L}_{N-1} & \hat{L}_{N-2} & \hat{L}_{N-3} & \dots & \hat{L}_0 \end{bmatrix} \begin{Bmatrix} q_0(t) \\ q_1(t) \\ \vdots \\ q_{N-1}(t) \end{Bmatrix} \tag{5.16}$$

Equation 5.16 gives an insight into how the influence coefficient method works. The rows of this matrix indicate the selection of a reference blade, which is the blade where the forcing will be calculated. For example, consider the first row of the matrix $\boldsymbol{L}$, which corresponds to the zeroth blade in the row. The vibration of blade 0 activates the L_0 influence coefficient, which represents the influence of the vibrating blade on its own forcing. Additionally, the vibration of blade +1 activates the L_{N-1} influence coefficient, which represents the influence of the vibrating blade +1 on the blade 0 forcing. It can therefore be seen that by selecting different reference blades, the forcing on each blade can be represented as the sum of influences due to the vibration of all blades in the row. Writing the influence coefficient matrix allows the forcing term to be moved to the left-hand side of the aeroelasticity equation, as shown in equation 5.17.

$$\ddot{\boldsymbol{q}} + \left[\text{diag}\left(\omega_i^2\right) - \boldsymbol{L}\right] \boldsymbol{q} = 0 \tag{5.17}$$

Throughout this thesis, it is assumed that the rotor blades are tuned. This means that the geometry, modal content, and flow are cyclic-symmetric

k	0	1	2	3	4
d_k	0	-1	-2	2	1

Table 5.1: Discrete distance function d_k as a function of the blade number k

and can be described by a travelling wave mode. For blades vibrating in a travelling wave mode, the phase lag between adjacent blades is constant and can be described by the inter-blade phase angle. For a rotor vibrating in a nodal diameter m, the inter-blade phase angle can be calculated as shown by equation 5.18. Knowledge that the phase lag is constant can then be applied to set the phases of modal displacements for each blade using a kinematic relationship. Let the modal displacements $q_k(t)$ for the k^{th} blade in a single row be defined using the inter-blade phase angle and the travelling wave mode amplitude $\hat{q}_m$ as shown in equation 5.19. Here k is counted in the direction of rotation of the rotor.

$$\sigma_m = \frac{2\pi m}{N_b} \tag{5.18}$$

$$\boldsymbol{q} = q_k(t) = \sum_{m=0}^{N_b-1} \hat{q}_m e^{i(\omega t + d_k \frac{2\pi m}{N_b})} \tag{5.19}$$

In equation 5.19, d_k is a circular function that maps the discrete distances between the blades in the row to a fixed reference blade, which then sets the phase lag of the vibration. To ensure that positive nodal diameters refer to forward travelling wave modes and negative nodal diameters to backwards travelling wave modes, the discrete distances are counted backwards to the direction of the rotor. An example of the function d_k is shown in table 5.1 for an example blade row containing five blades.
The definition of the modal displacements in equation 5.19 takes the form of an inverse Fourier transform. Consequently, the travelling wave mode amplitude can be determined if the individual blade modal displacements are known by performing a Fourier transform as

$$\hat{q}_m = \sum_{k=0}^{N_b-1} \hat{q}_k e^{-id_k \frac{2\pi m}{N_b}} \tag{5.20}$$

This equation has a very useful property, which allows multiple nodal diameters to be run simultaneously in a single CFD simulation. Let only the $k = 0$ blade vibrate in the prescribed blade mode shape, and keep all other blades fixed. This results in $\hat{q}_{k=0}$ being the only non-zero modal displacement in

the blade row. Since $d_k = 0$ when $k = 0$ as shown in table 5.1, then $\hat{q}_m$ is a constant for all nodal diameters. In other words, the vibration of the zeroth blade only excites all travelling wave modes with identical amplitude. The method stated above to determine the travelling wave mode amplitude can also be applied to the influence coefficients to determine the travelling wave mode coefficients C_m.

$$\hat{C}_m = \sum_{k=0}^{N_b-1} \hat{L}_k e^{-id_k \frac{2\pi m}{N_b}} \tag{5.21}$$

$$\ddot{\boldsymbol{q}}_m + \left[\text{diag}\left(\omega_m^2\right) - \boldsymbol{C}_m\right] \boldsymbol{q}_m = 0 \tag{5.22}$$

Equation 5.22 shows the aeroelastic equation of motion in travelling wave mode coordinates. The additional benefit of solving these equations, rather than those in terms of the influence coefficients shown in equation 5.17, is that the travelling wave mode coefficient matrix is diagonal. This means that the equations of motion for each nodal diameter m can be decoupled and solved independently. The solution method therefore treats each nodal diameter as its own damped, free-vibration SDOF oscillator. Assume a solution of the form

$$\boldsymbol{q}_m = \hat{\boldsymbol{q}}_m e^{\lambda_m t} \tag{5.23}$$

$$\therefore \left[\text{diag}\left(\lambda_m^2 + \omega_m^2\right) - \boldsymbol{C}_m\right] \boldsymbol{q}_m = 0 \tag{5.24}$$

As has been mentioned, the system of equations can now be decoupled into a single equation for each inter-blade phase angle

$$\lambda^2 + \omega_m^2 - C_m = 0 \tag{5.25}$$

$$\lambda = \pm\sqrt{C_m - \omega_m^2} \tag{5.26}$$

The aerodynamic damping ratio is found by a comparison of terms between the eigenvalues of the AIC approach and a SDOF oscillator. The equations of motion for a damped free-vibration SDOF oscillator are given by

$$\ddot{x} + 2\zeta\omega\dot{x} + \omega^2 x = 0 \tag{5.27}$$

$$x = \hat{x} e^{\lambda_S t} \tag{5.28}$$

$$\lambda_S = -\zeta\omega_n \pm i\omega_n\sqrt{1-\zeta^2} \tag{5.29}$$

$$\lambda_S = -\delta_r \pm i\omega_d \tag{5.30}$$

Equation 5.30 shows the system eigenvalues λ_S for a damped, free vibration single SDOF oscillator. Where ω_d is the damped natural frequency, ω_n is the natural frequency, and δ_r is the decay rate of the vibration response. The aerodynamic damping ratio for the AIC method can be found by a comparison of terms with the SDOF oscillator.

$$\omega_n = \sqrt{\omega_d^2 + \delta_r^2} = \sqrt{\Im\left(\lambda\right)^2 + \Re\left(\lambda\right)^2} \tag{5.31}$$

$$\zeta = \frac{\delta_r}{\omega_n} = -\frac{\Re(\lambda)}{\sqrt{\Im\left(\lambda\right)^2 + \Re\left(\lambda\right)^2}} \tag{5.32}$$

If $\zeta << 1$ then $\omega_d \approx \omega_n$ therefore

$$\zeta \approx -\frac{\Re(\lambda)}{\Im(\lambda)} \tag{5.33}$$

5.3.2 Work Done Method

For this method, a small, fixed-amplitude motion is prescribed to the blades in a pre-defined blade mode and frequency. In this method, the inter-blade phase angle is implemented by circumferential phase-lagged boundary conditions. An energy method is then used to relate the integrated work done per vibration cycle to the aerodamping ratio. Equation 5.34 shows the integrated work done per vibration cycle. The energy method of Carta [36] showed that the work done per cycle can be related to the logarithmic decrement by equation 5.35. The full proof of this equation is shown in Appendix I. The aerodamping ratio can be determined from the logarithmic decrement as shown in equation 5.36. It is assumed for all cases that the system is underdamped ($\delta \ll 1$), therefore the approximation shown in equation 5.36 is used throughout. Finally, the aerodamping ratio can be expressed in terms of the work done per vibration cycle in equation 5.37. It can be seen from equation 5.37 that the sign of the aerodamping ratio is opposite to that of the work done. This is the typical sign convention used in the literature for flutter. Where positive work done – or work done on the blade by the flow – causes increasing vibration amplitudes, which results in a negative aerodamping ratio. Whereas negative work done – or work done on the flow by the blade – causes decreasing vibration amplitudes, which results in a positive aerodamping ratio. The benefit of applying prescribed motion as

opposed to more traditional displacement tracking methods is that the local aerodynamic work can be examined on the blade surface. However, this method has the downside that the flutter frequency is assumed to be identical to the natural frequency of the system and that there is no interaction between assembly modes.

$$W = \int_T \int p\boldsymbol{n} \cdot \boldsymbol{v} dA dt \tag{5.34}$$

$$\delta = -\frac{W}{\hat{\dot{q}}^2} \tag{5.35}$$

$$\zeta = \frac{\delta}{\sqrt{\delta^2 + (2\pi)^2}} \approx \frac{\delta}{2\pi} \tag{5.36}$$

$$\therefore \zeta \approx -\frac{W}{2\pi \hat{\dot{q}}^2} \tag{5.37}$$

5.4 Propagation of Acoustic Waves in Annular Ducts

Whether an acoustic wave propagates axially within an annular duct can be determined by the axial wavenumber. An expression for the axial wavenumber for rigid body, or 'wheel' flow was determined by Zhao [24] as

$$k_x = \frac{-M_x \left(k - M_\theta \frac{m}{r}\right) \pm \sqrt{\left(k - M_\theta \frac{m}{r}\right)^2 - k_{r\theta}^2 \left(1 - {M_x}^2\right)}}{1 - {M_x}^2} \tag{5.38}$$

where M_x and M_θ are the axial and circumferential Mach numbers, m is the nodal diameter, $k_{r\theta}$ is the radial-circumferential wavenumber, and k is the free stream wavenumber. Here, the radial-circumferential wavenumber is found as a combination of Bessel functions. When the axial wavenumber is complex, axially propagating acoustic waves decay exponentially and are defined as cut-off. Whereas, if the axial wavenumber is real, then acoustic waves can propagate axially in the duct. Therefore, the cut-on condition is given by

$$\left(k - M_\theta \frac{m}{r}\right)^2 > k_{r\theta}^2 \left(1 - {M_x}^2\right) \tag{5.39}$$

From this relation, the cut-on frequencies can be determined by

$$\omega_{m,n} = aM_\theta \frac{m}{r} + a\sqrt{k_{r\theta}^2 \left(1 - {M_x}^2\right)} \tag{5.40}$$

where an acoustic wave will propagate when the frequency is greater than $\omega_{m,n}$. For a thorough derivation from the convected wave equation and explanation of the method for obtaining the radial-circumferential wavenumber, the reader is directed to the work of Zhao [24].

5.5 Post Processing Methods

5.5.1 Local Aerodynamic Damping

The work done per vibration cycle shown in equation 5.34 is integrated over the blade surface to give a single value for a given blade. However, the work done per cycle can also be expressed locally over the blade surface. This allows more detailed post-processing to determine regions on the blade surface that contribute detrimentally to flutter stability. It can also help to gain a deeper understanding of the interaction of local unsteady flow and vibration that generates a given aerodamping. The local work done per cycle vector is defined in equation 5.41.

$$W(x) = -\int_T p(x,t)\boldsymbol{n} \cdot \boldsymbol{\Phi} A \dot{q}(t) dt \tag{5.41}$$

where A is the local area and the local blade velocity has been expressed as the product of the modal velocity and the mode shape vector. Equation 5.41 can be expanded by assuming that the local unsteady pressure can be expressed as a simple cosine wave with some amplitude and phase lag. This assumption holds true when the vibration amplitude is small and the response is linear. Let

$$p(x,t) = \hat{p}(x)\cos(\omega t + \phi) \tag{5.42}$$

$$\dot{q}(t) = \hat{\dot{q}}\cos(\omega t) \tag{5.43}$$

$$\therefore W(x) = -\hat{p}(x)\boldsymbol{n} \cdot \boldsymbol{\Phi} \hat{\dot{q}} A \int_T \cos(\omega t + \phi)\cos(\omega t) dt \tag{5.44}$$

The expanded local work is defined by equation 5.44. It is helpful at this point to split equation 5.44 into two parts. The first part contains all the amplitude terms, and the second part contains the time integrals. The product of these two equations will reproduce the local work done per cycle.

$$W_1(x) = -\hat{p}(x)\boldsymbol{n} \cdot \boldsymbol{\Phi} \hat{\dot{q}} A \tag{5.45}$$

$$W_2(x) = \int_T \cos(\omega t + \phi)\cos(\omega t)dt \tag{5.46}$$

The expressions for W_1 and W_2 can be used to draw conclusions about the work done on the blade from known parameters and the amplitude and phase of unsteady pressure. The most important part of both of these equations is the sign of the product, which will determine whether stable or unstable work is done on the blade. Figure 5.1 shows a schematic of a two-dimensional blade section vibrating with both a pure plunge (left) and pure twist mode shape (right). The blade surface for both modes is split into four regions: the leading edge on the suction side (A), the trailing edge on the suction side (B), the trailing edge on the pressure side (C), and the leading edge on the pressure side (D). The sign of W_1 can be determined for each mode and location on the blade surface by evaluating the sign of the terms in equation 5.45. The amplitude of unsteady pressure $\hat{p}$ and the local area A are positive for both modes and all locations on the blade surface. The blade normal surface vector $\boldsymbol{n}$ is fixed by the blade geometry and will vary depending on the location on the blade. Finally, the sign and amplitude of the mode shape vector $\boldsymbol{\Phi}$ will vary depending on the chosen mode shape. The sign of W_1 for each mode shape and location on the blade surface is summarised in table 5.2.

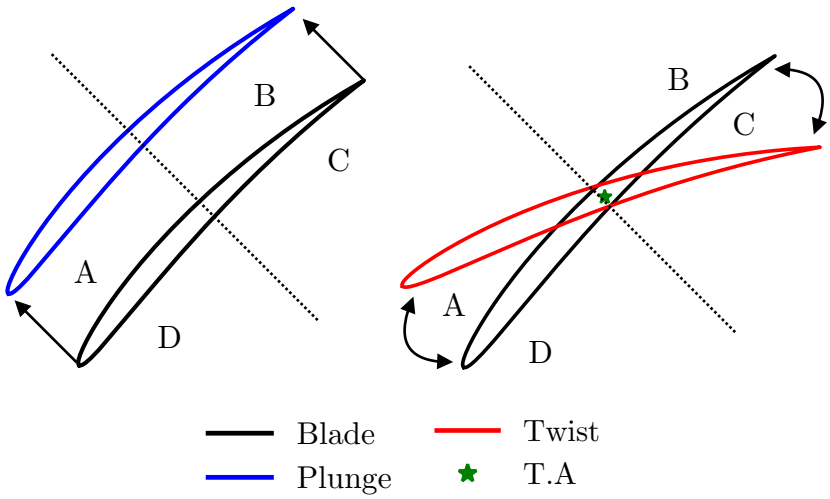


Figure 5.1: Schematic of a two-dimensional blade section vibrating with both a pure plunge (left) and pure twist mode shape (right)

	Plunge	Twist
A	+	+
B	+	−
C	−	+
D	−	−

Table 5.2: Sign of W_1 for a pure plunge and pure twist mode shape at different points on the blade surface

For the time integral component W_2 given by equation 5.45, it is the phase of unsteady pressure, which is critical for determining whether the work done is stable or unstable. Figure 5.2 shows how W_2 varies as a function of the phase lag of the unsteady pressure behind the modal velocity. This result shows that when $0 < \phi < 90$ and $270 < \phi < 360$, the sign of W_2 is positive, and when $90 < \phi < 270$, the sign of W_2 is negative. In addition, this shows that the peak values of W_2 occur when the phase of unsteady pressure is either completely in phase or completely out of phase with the modal velocity. Contrary to intuition, this means that the forcing must be in phase with the modal velocity to cause instability, rather than in phase with the displacement.

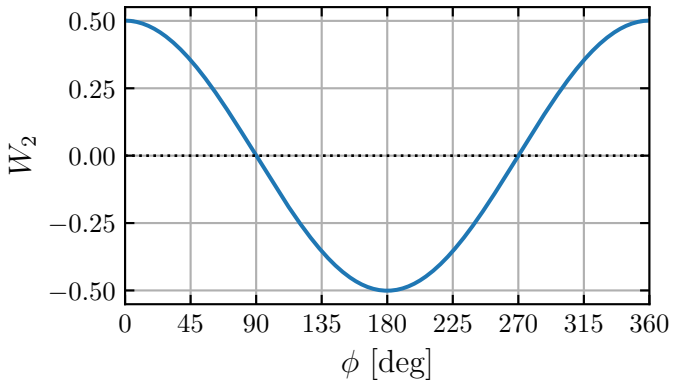


Figure 5.2: Time integral component W_2 as a function of phase of unsteady pressure

5.5.2 Components of Aerodynamic Damping

It was shown by Vahdati and Cumpsty [6], who expanded on the work of Kielb et al. [32] that the aerodynamic damping for 1F mode shapes can

be split into four components, which, when summated, recover the total aerodamping. Firstly, the 1F mode shape vector $\mathbf{\Phi}$ is split into its plunge mode $\mathbf{\Phi}_P$ and twist mode $\mathbf{\Phi}_T$ components, where the plunge and twist mode components sum to give the original 1F mode. To obtain the plunge mode component, the 1F mode shape is averaged at radial slices along the span of the compressor blade and assigned to all nodes in that layer. To obtain the twist mode component, the plunge mode component is subtracted from the 1F mode. This not only returns the twist mode component but also ensures that both components sum to give the original 1F mode shape. The plunge and twist mode shapes are then run as separate aeroelastic simulations at the same frequency and operating point. These simulations return the blade surface unsteady pressures due to plunge vibration $p_P(t)$ and twist vibration $p_T(t)$. The work done per cycle components can then be calculated as shown in equations (5.47)–(5.50).

$$W_{P,L} = \int_T \left[\int p_P(t) \boldsymbol{n} \cdot \mathbf{\Phi}_P dA \right] \dot{q}(t) dt \tag{5.47}$$

$$W_{T,L} = \int_T \left[\int p_T(t) \boldsymbol{n} \cdot \mathbf{\Phi}_P dA \right] \dot{q}(t) dt \tag{5.48}$$

$$W_{P,M} = \int_T \left[\int p_P(t) \boldsymbol{n} \cdot \mathbf{\Phi}_T dA \right] \dot{q}(t) dt \tag{5.49}$$

$$W_{T,M} = \int_T \left[\int p_T(t) \boldsymbol{n} \cdot \mathbf{\Phi}_T dA \right] \dot{q}(t) dt \tag{5.50}$$

It can be seen that each of the work done terms contains mixed values of $p_P(t)$, $p_T(t)$, $\mathbf{\Phi}_P$, and $\mathbf{\Phi}_T$. The subscripts of the pressure terms indicate the source of the forcing. For example, the presence of the term $p_P(t)$ indicates plunge motion-induced unsteady forcing, and $p_T(t)$ indicates twist motion-induced unsteady forcing. The subscript of the mode shape indicates the mechanism by which this forcing does work on the blade. For example, $\mathbf{\Phi}_P$ modifies the blade surface normal vector $\boldsymbol{n}$ so positive work is done when the pressure acts to induce a change in unsteady lift. Whereas, $\mathbf{\Phi}_T$ modifies the blade surface normal vector so positive work is done when the pressure acts to induce a change in unsteady moment. Therefore, $W_{P,L}$, for example, can be read as 'work done due to plunge motion induced unsteady lift'. When both the forcing mechanism and the interaction mechanism are defined, the work terms are referred to as 'forcing-vibration pairs'. The $W_{P,L}$ and $W_{T,M}$ terms can be found directly from the CFD simulations of the pure plunge and pure twist mode shapes. This is because the blade

surface unsteady pressures and the mode shape vectors are both taken from the same simulation, i.e., both from plunge or both from twist. For this reason, these work terms are called 'matching components'. For the $W_{T,L}$ and $W_{P,M}$ terms, additional post-processing is required, as the pressure and mode shape vectors are shared between plunge and twist simulations. For $W_{T,L}$, for example, the blade surface unsteady pressures $p_T(t)$ are taken from the twist simulation but are then multiplied by the mode shape vector from the plunge simulation $\mathbf{\Phi_P}$. As the pressure and mode shape are crossing over different simulations, these work terms are called 'cross components'. The sum of all four work done components returns the same work done as that obtained by running a single simulation of the original 1F mode shape. The aerodamping ratio is obtained from the work done components, as shown in equation 5.51. To ensure that the aerodamping ratio calculated from the components is correctly normalised compared to the 1F mode, the modal mass used in the calculation of the amplitude of the modal velocity includes both plunge and twist vibration modes, as shown in equations (5.52)–(5.54).

$$\zeta = -\frac{(W_{PL} + W_{TL} + W_{PM} + W_{TM})}{2\pi\hat{\dot{q}}^2} \tag{5.51}$$

$$\hat{\dot{q}} = \sqrt{m_r}\omega \tag{5.52}$$

$$m_r = \mathbf{\Psi}^T \mathbf{M} \mathbf{\Psi} \tag{5.53}$$

$$\mathbf{\Psi} = \mathbf{\Psi}_P + \mathbf{\Psi}_T \tag{5.54}$$

6 Analysis of a Weakly Loaded Subsonic Linear Cascade

In this chapter, a weakly loaded subsonic linear cascade is used for aeroelastic simulations. The implementation of this geometry and operating point has two benefits. Firstly, the experimental rig on which these simulations are based allows variation of the rotor blade plunge-twist ratio, reduced frequency, and nodal diameter, which provides validation of what is frequently a purely computational investigation of these parameters in the literature. Secondly, the simplified flow and geometry of this test case allow a clear separation of the driving factors for flutter. Therefore, in the first part of this chapter, parametric studies on the effect of plunge-twist ratio, reduced frequency, and nodal diameter are performed in order to validate unsteady CFD. After this, an extended modal parameter space is investigated, which is outside the permissible range of the experimental rig, in order to investigate trends in aerodamping across a wider input range. Unsteady CFD is then used to build stability maps. These maps indicate regions where flutter is likely to occur and allow the determination of the stability limit, where the aerodamping is zero, as a function of the modal inputs. Finally, the validity of the linear cascade implementation is analysed by comparing results to several other cascade implementations that are more representative of a low-speed compressor geometry and operating point.

6.1 Test Case

Test Rig

Investigations were conducted on a weakly loaded subsonic linear compressor cascade, based on the test rig shown in figure 6.1. Experimental data for the purpose of validating CFD was obtained in a collaborative project with TU Berlin. The air flow through the test rig is provided by a radial blower, which is then homogenised by passing through a diffuser and a settling chamber with multiple honeycomb grids. Finally, the flow passes through a converging nozzle before entering the measurement section, which houses the blades. The outlet flow is then expelled at atmospheric pressure at the end of the measurement section. Several flow properties are measured to ensure the correct operating point: total pressure and temperature are measured at the settling chamber side wall; dynamic pressure with a Pitot-static probe at the centre of the measurement section inlet face; and inlet static pressure at the inlet face side wall. These variables are used to inform

the boundary conditions of the CFD setup.

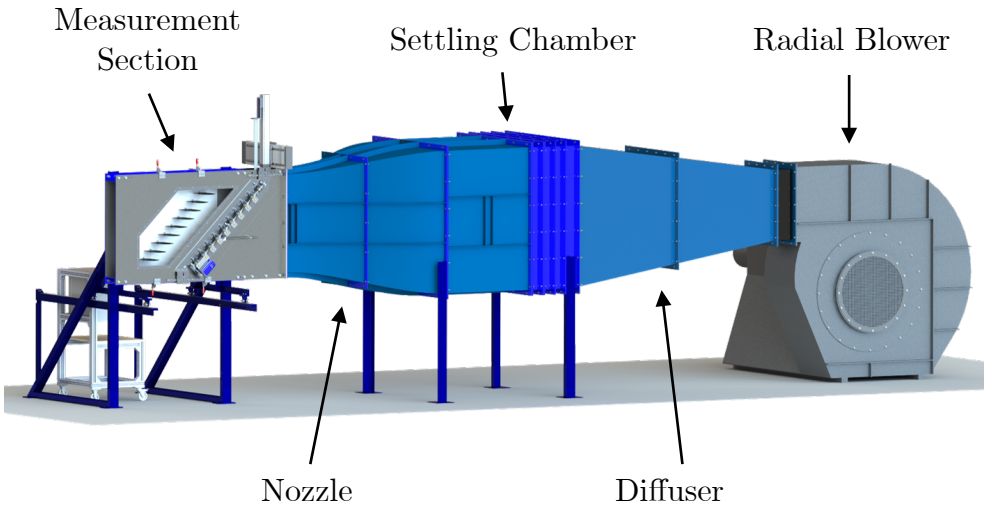


Figure 6.1: Experimental test rig

Measurement Section

Figure 6.2 shows the test rig measurement section. The cascade is comprised of a single blade row housed in a rectangular 'fish tank' geometry. The blades are highlighted in grey, and the dimensions of the section are highlighted in red. The hub and tip (front and back wall in dimension z of figure 6.2) are flat, and therefore the cascade is termed 'linear'. This differentiates the cascade from an annular geometry, which has a curved hub and casing and is typically circumferentially periodic. As linear cascades cannot be periodic, the circumferential boundaries (top and bottom walls in Figure 6.2) are terminated by viscous hard walls.

The cascade blade row is formed by an eleven-blade passage with a pitch-chord ratio of $S/c = 0.75$. The blade profiles are a modified NACA 65-Series [65], with a maximum thickness of $6\%c$ at half-chord and 10° circular arc camber line. The span-chord ratio of the blades is 1.313. The stagger is fixed to $\gamma = 43°$, and since the inlet flow is limited to having zero y velocity, the incidence on the blade row is fixed at $i = 2°$. The implementation of a low incidence limits the likelihood of corner separations and also means the operating point is far away from stall. The inlet Mach number set by the blower is constant throughout, with $M_i = 0.087$, so the flow through the cascade is entirely subsonic. This results in a Reynolds number of $Re = 0.3 \times 10^6$ at the inlet face. The blade profile and operating point aim to

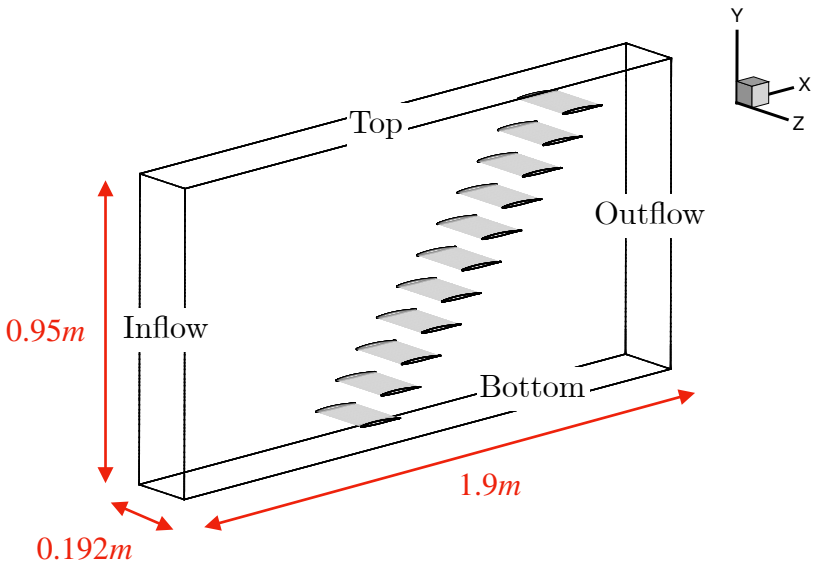


Figure 6.2: Test rig measurement section

replicate a two-dimensional section cut of a low-speed compressor blade row in the tip region. While the flow through the measurement section is three-dimensional, the blade section and inlet flow profile are constant along the span and will therefore be considered quasi-two-dimensional.

Piezo-resistive differential pressure transducers were employed to measure the blade surface pressures across the seven central blades of the cascade. The pressure transducers exhibited linear behaviour around the zero point and can be considered bidirectional. Calibration was conducted against externally calibrated precision pressure cells, which showed accurate pressure readings in the single-digit Pascal range. The data acquisition system provided a theoretical resolution of 0.0267 Pa. The measurement blades have twenty mid-span pressure taps, with ten each for the suction and pressure surfaces. The experimental setup can therefore only measure the unsteady pressures at mid-span. The pressure taps have an exponential spacing along the chord, with greater density towards the leading edge.

Blade Mode Shape

The blade mode shape implemented in this chapter is a quasi-two-dimensional combined plunge-twist mode shape, which approximates a 1F mode. The mode shape is defined purely analytically; no structural FEA was performed on the blades themselves to determine the mode. There are several assump-

tions made about the vibration mode of the blades. Firstly, it is assumed that the 1F mode can be defined by a combined mode, which is a superposition of pure plunge motion perpendicular to the chord and pure twist motion about the half chord blade centre. Secondly, it is assumed that the pure plunge and pure twist components are in phase. For this implementation, this means the plunge motion starts the vibration cycle with an upward motion and the twist motion with a clockwise rotation, which acts to open the blade passage. Finally, it is assumed that the blades are rigid bodies, so there is no chord-wise flexion of the mode shape. Under these assumptions, the mode shape is equivalent to a single degree of freedom (SDOF) rotation about a twist axis located a chord-wise distance l downstream of the leading edge. This distance is referred to as the 'twist axis setback'. By varying l, the plunge-twist ratio of the mode shape can be varied, where $l = 0.5c$ corresponds to a pure twist mode shape and $l \to \infty$ to a pure plunge mode. The normalised twist axis setback l/c is used as the parameter to define the plunge-twist ratio and the reduced frequency k to define the vibration frequency.

Vibrating Blade Module

The blade movement is prescribed experimentally by a vibrating blade module. Throughout this chapter, an AIC method is implemented; therefore, the vibrating blade module will only prescribe motion to the central blade of the cascade. All the other blades are fixed. An additional requirement of this method is that the module implements forced vibration, and the unsteady aerodynamic forces have no influence on the amplitude of the vibration. The central blade of the cascade is attached at the hub to a lever on the outside of the wind tunnel. The lever is mounted to a traversing plate, which can be moved back and forth along linear bearings on the side wall to change the twist axis setback. Figure 6.3 shows a section cut of the traversing plate at its maximum twist axis setback. Moving the blade position in the slot fixes the location of the blade in the cascade. Oscillatory motion is provided by an electric step motor, with an eccentric attached to its shaft through a scotch yoke mechanism and a connecting rod. The motor speed is used to vary the blade vibration frequency. Lever displacement is monitored with a laser triangulation distance sensor at the tip of the lever. It should be noted here that the actual experimental implementation of the mode shape will have a small span-wise component, as the blade is not constrained at the tip. A more detailed summary of the experimental implementation and results is given by Malzacher et al. [66].

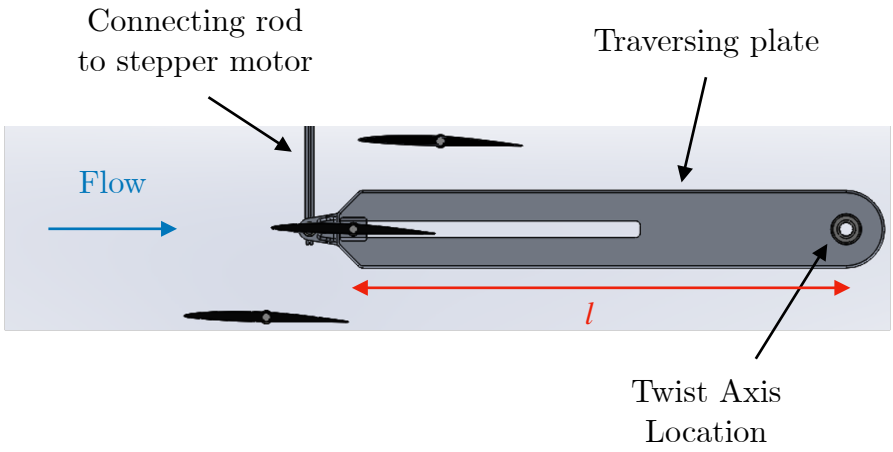


Figure 6.3: Vibrating blade module

6.2 Computational Model

Domain

Figure 6.4 shows a span-wise view down the cascade with the blade numbering convention used in the CFD. Blades are numbered from -5 (top) to $+5$ (bottom) in the direction of what would be positive rotation for the rotor. The vibrating blade 0 is the central blade of the cascade. The inflow and outflow boundaries are highlighted in green, while all other viscous boundaries are shown in black. The steady-state flow solutions are obtained by imposing total pressure, total temperature, and flow angle at the far-field inflow boundary as well as static pressure at the outflow boundary. One-dimensional non-reflecting boundary conditions are implemented at the inflow and outflow boundaries to minimise undesirable reflections, which are known to affect flutter stability [25]. The flow is assumed to be turbulent throughout the entire domain.

Mesh

The computational mesh is semi-unstructured. In the span-wise direction, the domain is discretised by 23 radial layers. All viscous surfaces, including the hub, tip, top, and bottom walls of the domain, have near-wall mesh refinement to correctly capture the flow in the boundary layer. The mesh of the top blade -5 and the refinement near the top wall can be seen in figure 6.5. The boundary layer is resolved with a high density of hexahedral

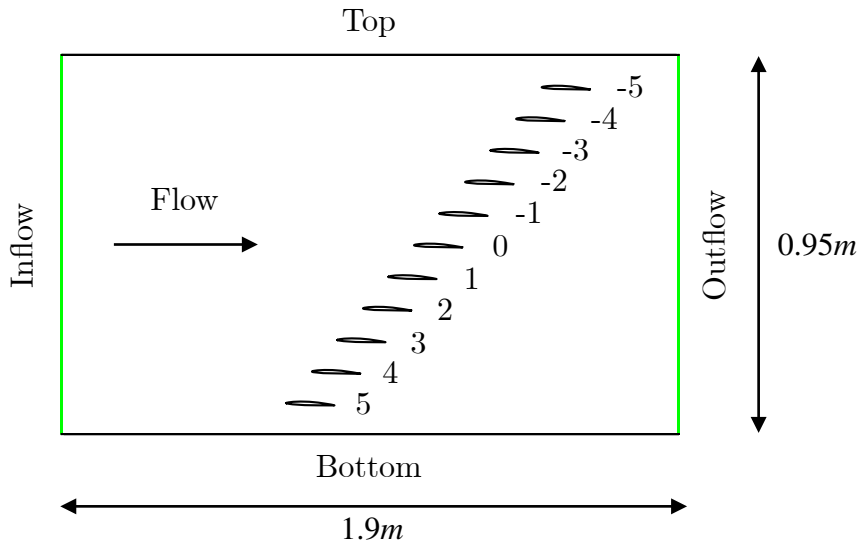


Figure 6.4: Measurement section geometry with dimensions

elements, with an average of $y+ = 45$. Approximately 86% of the surface elements have $\{25 < y+ < 65\}$. The far field contains a coarser prismatic mesh, which aims to minimise reflection of disturbances off the inflow and outflow boundaries. The inlet boundary is placed four chords upstream of the leading edge of blade 0 and the outlet is placed four chords downstream of the trailing edge of blade 0. The overall mesh contains approximately 1.7×10^6 nodes. Several mesh densities were investigated, and the final mesh was selected based on agreement with the experimental data.

Mode Shape

A schematic of the implementation of the combined mode and the key parameters is shown in figure 6.6, where T.A. is the twist axis location, l is the twist axis setback, $\hat{H}$ is the plunge displacement amplitude, $\hat{t}$ is the twist displacement amplitude, and $\hat{\theta}_T$ is the twist angle amplitude. The leading and trailing edge amplitudes can therefore be given by $A_{LE} = \hat{H} + t$ and $A_{TE} = \hat{H} - t$ respectively. By changing the twist axis setback l, the plunge-twist displacement ratio, $\hat{H}/\hat{t}$, of the mode can be varied. The normalised twist axis setback l/c is used as the variable for prescribing the plunge-twist ratio.

An arbitrary origin rotation of axes method is used to implement the SDOF rotation about the twist axis. For this method, the origin is set to the

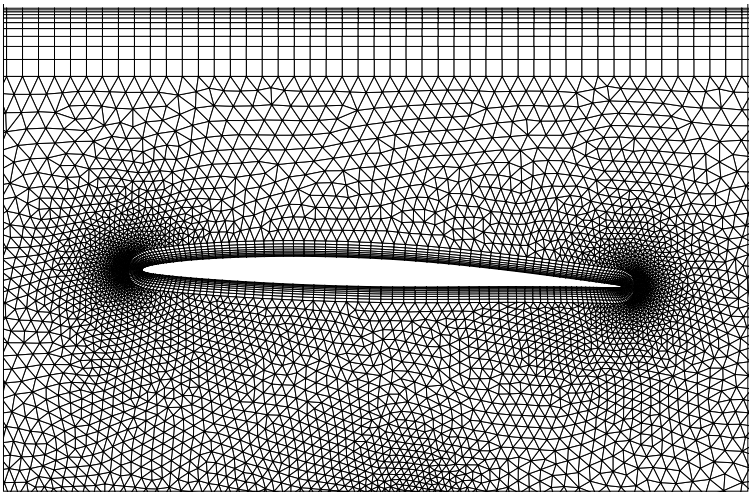


Figure 6.5: Computational mesh showing blade -5 and the top wall

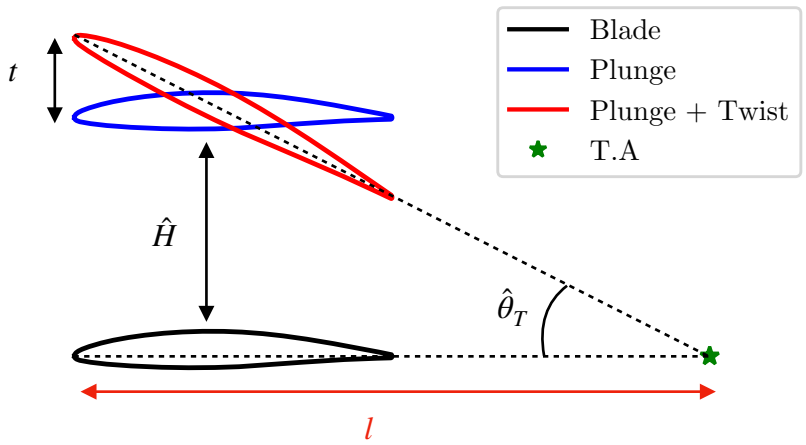


Figure 6.6: Schematic showing rigid body rotation around the twist axis (T.A)

twist axis location (x_{TA}, y_{TA}) and each node on the blade surface is rotated about said origin by an angle θ_T. This returns a new set of perturbed blade coordinates, which are then subtracted from the initial blade coordinates to obtain the mode shape vector. The rotated coordinate vectors in x and y are given by $\boldsymbol{d}_x$ and $\boldsymbol{d}_y$ respectively. The implementation of the rotation is shown in equations (6.1)–(6.2).

$$\boldsymbol{d}_x = x_{TA} + (\boldsymbol{x} - x_{TA})\cos(\theta_T) + (\boldsymbol{y} - y_{TA})\sin(\theta_T) \tag{6.1}$$

$$\boldsymbol{d}_y = y_{TA} - (\boldsymbol{x} - x_{TA})\sin(\theta_T) + (\boldsymbol{y} - y_{TA})\cos(\theta_T) \tag{6.2}$$

As mentioned in chapter 5, the aeroelastic solver used in this work is weakly coupled. One requirement of this implementation is that the physical displacements can be satisfied by the product of a linear mode shape vector and the modal displacement vector. Assuming that θ_T is small, the mode shape can be linearised in θ_T by a small angle approximation, transforming the rotated coordinate vectors into equations (6.3)–(6.4).

$$\boldsymbol{d}_x = x_{TA} + \boldsymbol{x} - x_{TA} + (\boldsymbol{y} - y_{TA})\theta_T \tag{6.3}$$

$$\boldsymbol{d}_y = y_{TA} - (\boldsymbol{x} - x_{TA})\theta_T + \boldsymbol{y} - y_{TA} \tag{6.4}$$

Finally, the initial blade coordinate vectors can be subtracted from the perturbed coordinate vectors to obtain the physical mode shape vectors, as shown in equations (6.5)–(6.6). The mode shape vector is then mass-normalised, and a modal displacement is selected to satisfy the correct physical displacement. The blade vibration is discretised in time, with 360 time steps per vibration cycle. This time step was chosen from a time convergence study based on agreement with the experimental data.

$$\boldsymbol{\Psi}_x = (\boldsymbol{y} - y_{TA})\theta_T \tag{6.5}$$

$$\boldsymbol{\Psi}_y = -(\boldsymbol{x} - x_{TA})\theta_T \tag{6.6}$$

6.3 Computational Results

6.3.1 Validation

Prior to investigating the parameters that drive flutter, the steady and unsteady CFD results are validated against experimental measurements. It should be noted here that experimental validation of the CFD is conducted

using only the mid-span steady and unsteady pressures, as this is the only span-wise location on the blade for the experimental pressure transducers.

Figure 6.7 shows the validation of the steady-state blade surface pressure coefficient C_p as a function of the normalised chord x/c. There is a good agreement for blades 0 and +1, whereas blade −1 has some minor discrepancies towards the leading edge on the pressure side. There are a few explanations for this discrepancy. Firstly, the prescribed stagger angle of blade −1 was not implemented precisely enough prior to the experimental campaign. Since the flow angle is fixed, an incorrect stagger angle may change the flow incidence on the cascade, causing a discrepancy at the leading edge. Secondly, the steady aerodynamic loading when the blower was switched on caused small changes to the applied stagger angle. Although this particular explanation does not explain why this discrepancy is only noticeable on blade −1. Thirdly, the third pressure tap on the pressure side of blade −1 was faulty and returned incorrect readings, as this is the only tap with poor agreement. Finally, this could be a poor prediction of the CFD. Figure 6.7 also shows that there is a non-uniform loading across the blades in the cascade, as blade +1 has a higher mean static pressure than blade −1. This is due to the viscous hard walls on the top and bottom of the cascade, which are limiting the flow turning from the blades. This results in a higher mean static pressure on the cascade bottom wall and a lower mean static pressure on the top wall, which would create a pressure gradient along each of the blades in the row.

For the unsteady CFD, the mid-span unsteady pressure on the blade surfaces is compared. In the CFD, the pressure signals are Fourier-decomposed into amplitude and phase at the prescribed blade vibration frequency. Due to the subsonic, low incidence, and attached flow, the Fourier components in the higher harmonics of the vibration frequency are neglected, as they are several orders of magnitude smaller than the first harmonic. The results are shown in terms of the unsteady pressure coefficient $C_p{}'$ in figure 6.8 for $k = 0.2$ and $l/c = 1.3$ across the five central blades of the cascade. Here, the phase is shown with respect to the modal velocity. The amplitudes of unsteady pressure from CFD are generally well predicted. There is a large dip in the amplitude of unsteady pressure from tap three on the pressure side of blade −1. This is the same tap that had issues with poor agreement for the steady pressure coefficient in figure 6.7. It is concluded that this faulty tap is the reason for the discrepancy in both results. The largest amplitude of unsteady pressure occurs at the leading edge of the vibrating blade, as the vibration of the blade causes the stagnation point to switch between the suction and pressure sides over each vibration cycle. The slope of the phase with respect to the normalised chord gives an indication of the velocity of

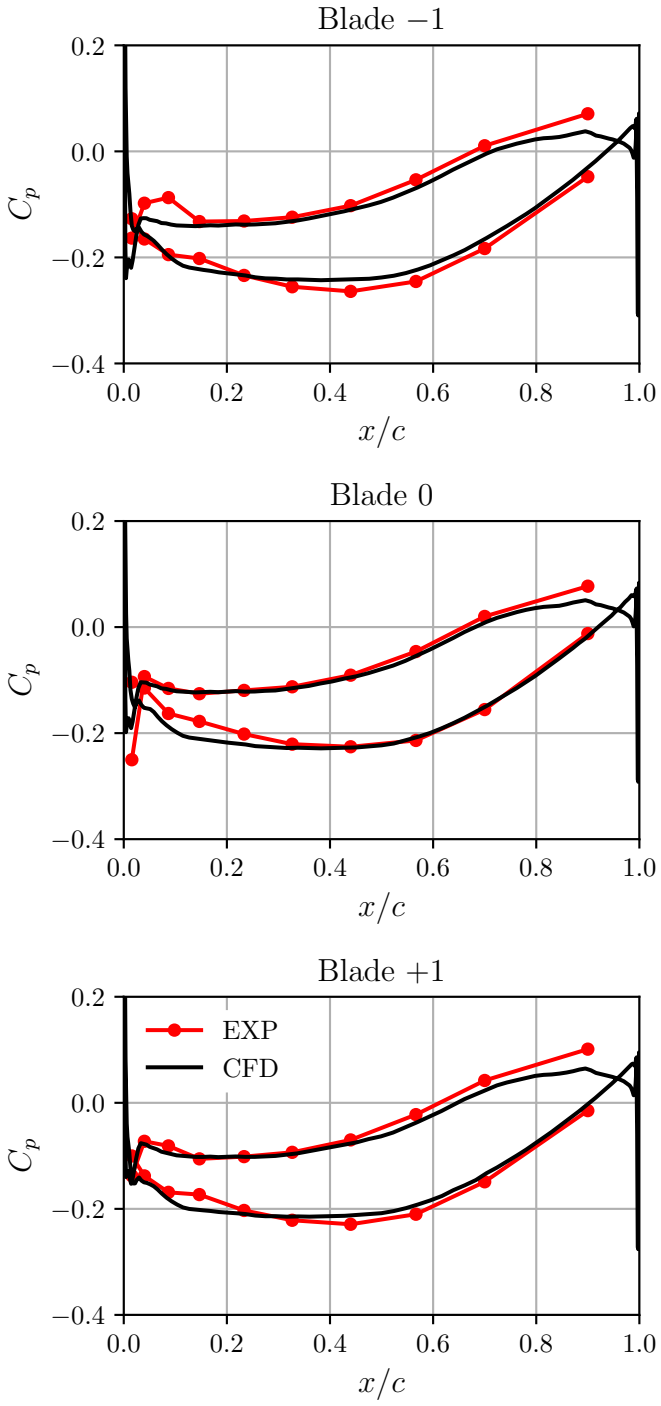


Figure 6.7: Validation of the blade steady pressure coefficient against experimental data

the unsteady pressure perturbations [40]. For a 1D wave, the wave velocity is given by

$$v = \frac{\omega}{k} = \frac{\omega}{d\phi/dx} \tag{6.7}$$

where k is the wave number, ω is the angular frequency, and ϕ is the phase. Therefore, the gradient of the phase with respect to x/c indicates the direction and speed of travel of a perturbation in pressure. A positive gradient of the phase indicates a downstream travelling perturbation, and a negative slope indicates an upstream travelling perturbation. It can be seen that for the suction side of blade 0, the gradient of the phase is positive, indicating a downstream travelling perturbation. The unsteady disturbance then propagates away from blade 0 downstream towards blade -1, inducing a large unsteady pressure amplitude on the pressure side. A much smaller unsteady pressure amplitude is felt on the suction side of blade -1 as the disturbance does not travel as effectively past the leading edge. Disturbances propagating from blade 0 to blade $+1$ must travel against the convected flow and are therefore acoustic in nature. This differentiates the disturbances propagating from blade 0 to blade -1, which will have additional entropic and vortical convected components [48]. This can be seen from the gradient of the phase for the suction side of blade $+1$, which has a negative gradient, indicating that there is an upstream travelling disturbance propagating from blade 0. Since perturbations travelling from blade 0 to blade $+1$ travel against the convected flow, the overall amplitudes of unsteady pressure are considerably smaller than for blade -1. In addition to the convected flow, there is also a pressure gradient across the cascade, which such perturbations must also travel against. For blade $+1$, the largest amplitudes of unsteady pressure occur on the suction side, as this side is closest to the vibrating blade 0.

The chord-wise length of the covered passage is approximately half chord for all blades in the row. It can be seen that there is very little phase change between the suction side of blade 0 and the pressure side of blade -1 at approximately half chord where the covered area is shared. It can also be seen that there is very little phase change between the pressure side of blade 0 and the suction side of blade $+1$ at half chord where the covered passage is shared. This indicates that there is a near instantaneous propagation of the disturbance from blade 0 to the suction side and pressure side of blade -1 and blade $+1$, respectively.

The integrated modal force and displacement for each blade are converted into the aerodynamic influence coefficients to begin the validation of the aerodamping analysis. Figure 6.9 shows the validation of the complex influence coefficients for blades -3 up to $+3$ for $k = 0.4$ and $l/c = 1.25$. Coefficients

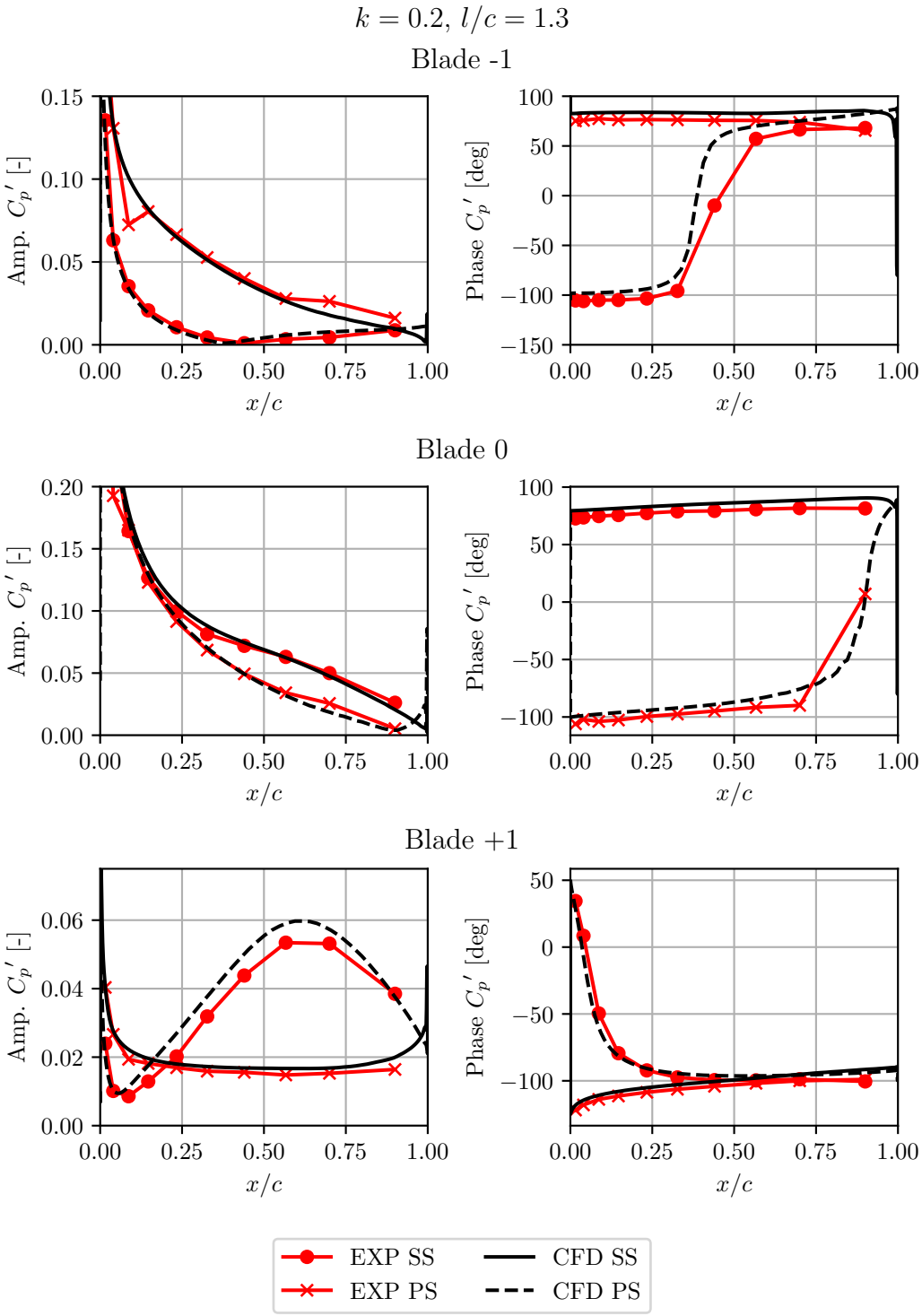


Figure 6.8: Validation of the blade unsteady pressure coefficient against experimental data – $k = 0.2$, $l/c = 1.3$

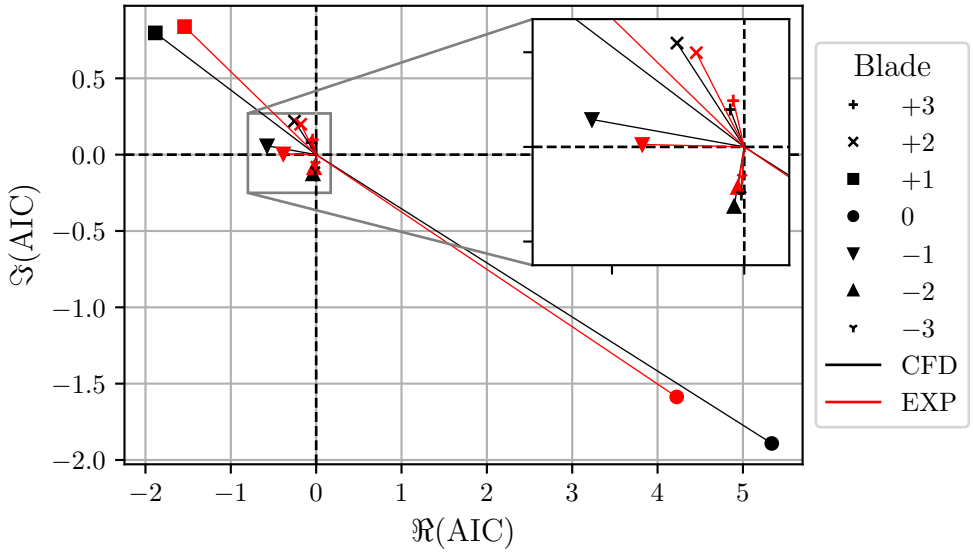


Figure 6.9: Validation of the complex AIC's – $k = 0.4$, $l/c = 1.25$

with a positive imaginary component will cause instability as they are in phase with the modal velocity, causing work done on the blade by the flow [67]. It can be seen that blade 0 provides the largest stabilising contribution. In all tested modes, blade 0 always has a stabilising contribution as the forcing generated by the vibration damps its own vibration, which is in agreement with conclusions from the literature for unstalled blades [68]. Generally, blades a greater discrete distance from the vibrating blade 0 will have smaller AIC magnitudes and subsequently contribute less to the travelling wave mode coefficient amplitude. This is because disturbances propagate less effectively over a larger distance from the vibrating blade, which induces a smaller modal force amplitude and thus a smaller influence coefficient. It can be seen from figure 6.9 that the AICs of the blades furthest away (+3 and −3) have a much smaller magnitude than the blade 0 closest neighbours. For this reason, coefficients for blades $> \pm 3$ will be neglected when calculating the aerodamping. This also allows consistency with the experimental campaign.

The aerodynamic damping ratio can now be calculated by the eigenanalysis shown in Section 5. Figure 6.10 shows the validation of aerodamping against the inter-blade phase angle for $k = 0.4$ and $l/c = 1.25$. There is a good agreement between CFD and experiment, both in the trend of aerodamping as a function of inter-blade phase angle and the prediction of the location and amplitude of the minimum aerodamping. The mean absolute

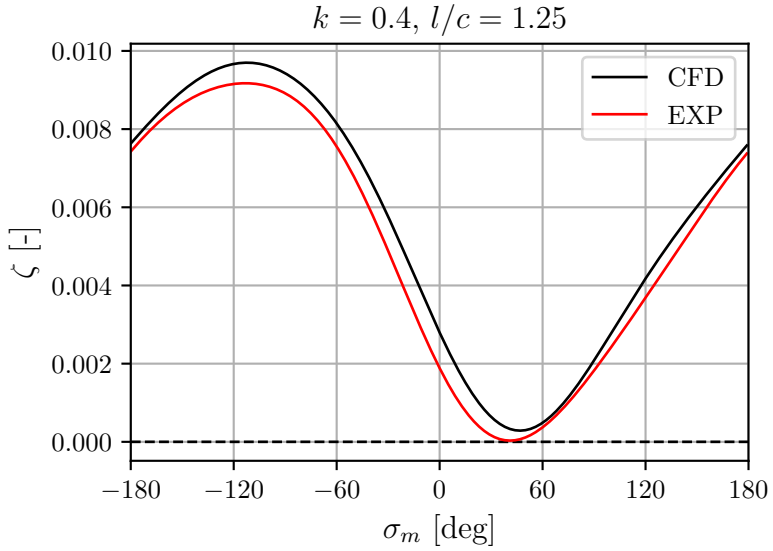


Figure 6.10: Validation of the aerodamping as a function of inter-blade phase angle – $k = 0.4$, $l/c = 1.25$

error for this reduced frequency and twist axis setback is $\epsilon = 4.7 \times 10^{-4}$. The percentage error is not stated as the expected result is close to zero for some inter-blade phase angles. Both CFD and experiment show that for this k and l/c, flutter occurs in low inter-blade phase angles and forward travelling wave modes, which is expected for flutter of this kind [69].

6.3.2 Steady State Results

Following the successful validation of steady flow, unsteady flow, and aerodamping at mid-span, results are now shown for flow throughout the entire domain. Figure 6.11 shows CFD results for the steady pressure coefficient contour at the nominal operating condition. It can be seen from the figure that there is a positive pressure gradient from blade +5 (bottom) to blade −5 (top). This gradient is caused by the viscous end-walls on the top and bottom walls of the cascade. The alignment of the blade stagger angle and the bottom and top walls of the cascade creates an incidence of $i = 2°$, which prevents uniform flow deflection. This turns the region between blade +5 and the cascade bottom wall into a converging nozzle, which increases the mean upstream static pressure. Conversely, the region between blade −5 and cascade top wall is turned into a diverging nozzle, which decreases the mean upstream static pressure. The mean blade loading across the blade row is not only non-uniform but also non-linear with respect to the distance from the

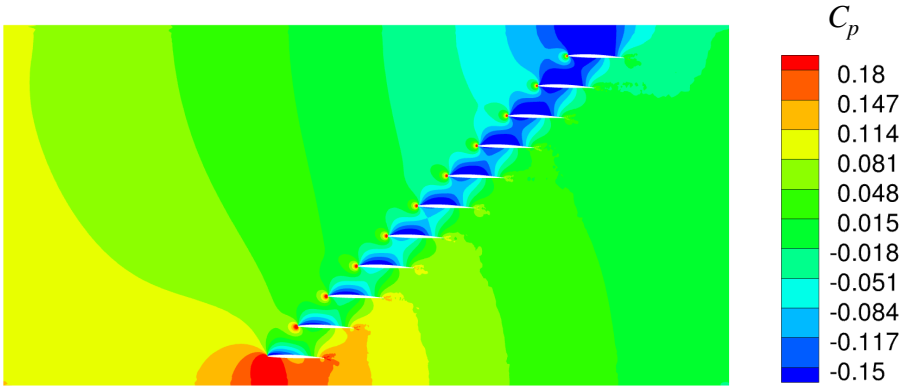


Figure 6.11: Mid-span steady pressure coefficient contour

end-walls, as the blade geometry is different for the diverging and converging sections.

Figure 6.12 shows the blade suction side surface pressure coefficient contour of the central blade 0 with surface streamlines. It can be seen from the figure that the largest blade loading on the suction side occurs towards the trailing edge, which is validated by the mid-span experimental validation in figure 6.7. The main conclusion to be drawn from this figure is that there is some span-wise variation in the flow field that cannot be validated by the experiment, as the experiment only has pressure taps at mid-span. Towards the hub and casing, there is an increase in the pressure coefficient due to the viscous boundary layer reducing the flow velocity, thus increasing the static pressure. It can also be seen that there is a small deflection of the surface streamlines towards the trailing edge near the hub and casing. This deviation is the initial formation of a corner separation, but due to the small incidence $i = 2°$, the effects are relatively small. Corner separations for similar cascades have been shown to occur at a minimum of $i = 4°$ [70].

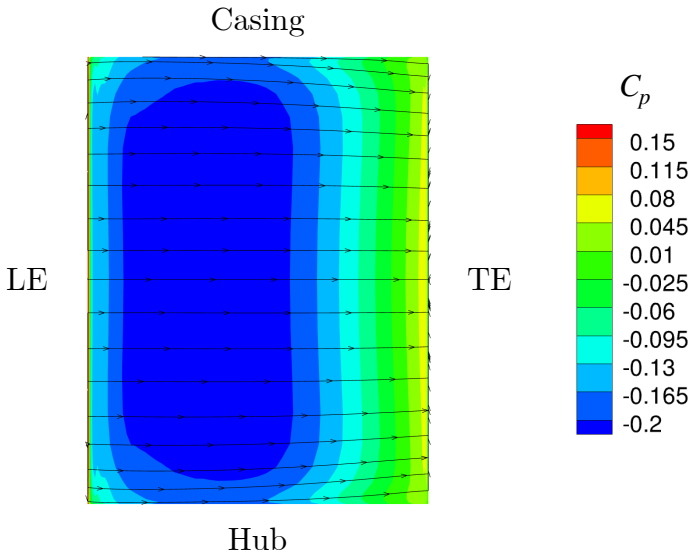


Figure 6.12: Steady pressure coefficient contour and streamlines of the suction side of blade 0

6.3.3 Unsteady Results

Numerical simulations are now used to predict the aerodynamic damping over a wider range of reduced frequencies and normalised twist axis setbacks than permitted in the experiment. The reduced frequencies are varied in the range $0.2 < k < 0.7$, and the normalised twist axis setback is in the range $0.5 < l/c < 3$, where the former corresponds to a pure twist mode and the latter contains a large plunge component. For this set of results, the unsteady flow over the entire blade is used for the calculation of the aerodamping.

Figure 6.13 shows the curves of aerodynamic damping against the inter-blade phase angle for different l/c with $k = 0.6$. For $l/c > 1$, the aerodamping is positive and stable for all inter-blade phase angles. Negative aerodamping occurs when $l/c < 1$ in small, positive inter-blade phase angles, which corresponds to flutter in a forward travelling wave mode. It can be seen that, in general, increasing l/c increases the aerodamping for all inter-blade phase angles. This is equivalent to saying that decreasing the amount of twist in the combined mode shape makes the rotor more stable for this operating point and reduced frequency. It can also be seen that the minimum aerodamping, which is the minimum across all inter-blade phase angles, does not increase linearly with l/c but rather follows some higher-order growth. The shape of the aerodamping curves changes significantly as l/c is varied. For $l/c = 2$, the aerodamping curve follows a near-negative cosine with a mini-

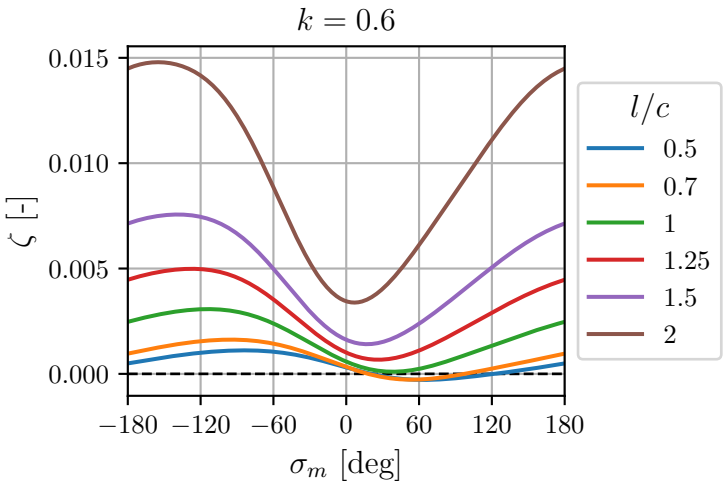


Figure 6.13: Aerodamping as function of IBPA for different l/c at $k = 0.6$

mum aerodamping at $\sigma_m = 7°$, whereas for $l/c = 0.5$, the curve more closely resembles a negative sine shape with a minimum aerodamping at $\sigma_m = 64°$. Consequently, the largest range of unstable IBPA's exists for the pure twist mode shape $l/c = 0.5$ and is unstable in the range $21° < \sigma_m < 120°$.

Figure 6.14 shows the curves of aerodynamic damping against the inter-blade phase angle for different l/c with $k = 0.2$. For this reduced frequency, there are negative aerodamping values for all l/c at some inter-blade phase angles, which are generally small and positive. When comparing the aerodamping curves for $k = 0.2$ to those for $k = 0.6$, it can be seen that generally, decreasing the reduced frequency decreases the aerodamping, meaning low reduced frequency vibration modes are more susceptible to flutter. Interestingly, the minimum aerodamping does not occur at $l/c = 0.5$ but instead at $l/c = 1.25$. This indicates that the mode stabilises as $l/c \to 0.5$ for a pure twist mode shape. This will be discussed in further detail in the coming results.

The aerodamping curves for $k = 0.6$ in figure 6.13 and $k = 0.2$ in figure 6.14 have very different shapes. By looking at equation 5.21, it can be seen that the travelling wave mode coefficients are the result of a Fourier transform of the aerodynamic influence coefficients. Where the AIC's are the Fourier coefficients and the harmonic is the discrete distance function δ_k between blade 0 and the adjacent blades in the row. Therefore, blade 0 corresponds to the zeroth harmonic Fourier coefficient, the inclusion of the two nearest neighbours adds the first harmonic Fourier coefficient, and so

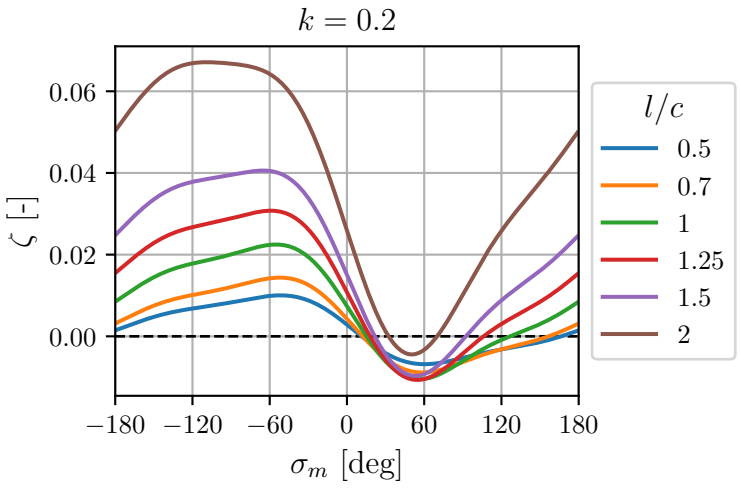


Figure 6.14: Aerodamping as function of IBPA for different l/c at $k = 0.2$

on. The Fourier transform sums all of the coefficients to find the travelling wave mode coefficients. Figure 6.15 shows the individual contribution of each Fourier coefficient and how they sum to give the total aerodamping ratio. It was shown by Crawley [68] that the forcing generated by the vibration of Blade 0 always damps its own vibration. Subsequently, the zeroth Fourier coefficient always has a positive value, and due to it being the zeroth coefficient, it is constant with respect to the inter-blade phase angle. Critically, it is the zeroth coefficient that can be used to determine the mean aerodamping as a function of the inter-blade phase angle. It can be seen that as the Fourier coefficient increases, the amplitude of the aerodamping contribution decreases. This is because the amplitude of the AIC's decreases as the distance from the vibrating blade 0 decreases, as shown in figure 6.9. It can be seen from $k = 0.2$ in figure 6.14 that the higher order harmonics contribute significantly to the aerodamping compared to $k = 0.6$ in figure 6.13 for the same l/c. It can therefore be concluded that at low reduced frequencies, unsteady disturbances propagate more effectively to the blades that are further away as compared to higher frequencies, which in turn decreases aerodamping.

To further investigate the trends in reduced frequency, aerodamping is plotted as a function of reduced frequency for the different values of l/c at a constant inter-blade phase angle in figure 6.16. For these cases, $\sigma_m = 40°$ was selected because this was one of the most unstable inter-blade phase angles at each reduced frequency. Comparing the curves in figure 6.16, it is

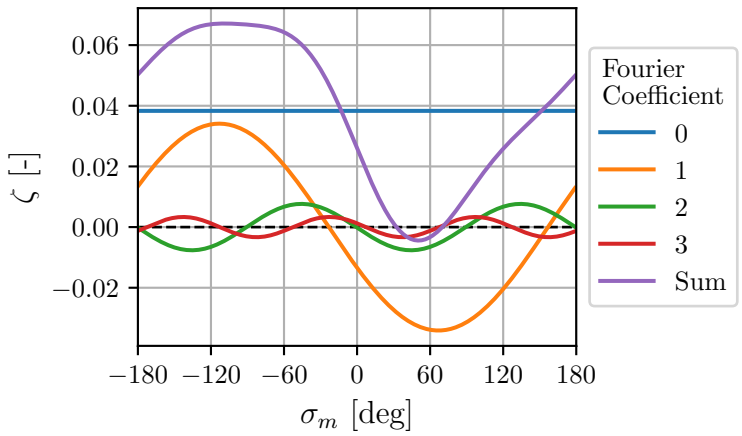


Figure 6.15: Harmonics of travelling wave mode coefficients expressed in terms of aerodamping, $k = 0.2$, $l/c = 2$

clear that the reduced frequency has a strong influence on the aerodynamic damping. However, different trends are seen across the range of twist-axis setbacks. When the twist axis is inboard of the aerofoil, $l/c < 1$, aerodynamic damping is negative for all reduced frequencies. Whereas mode shapes with a larger plunge component, $1.5 < l/c < 3$, reach a local maximum at some reduced frequency, typically in the region of $k = 0.3$. It can therefore be concluded that increasing the reduced frequency does not necessarily decrease the aerodamping, as is expected from the literature [71]. For all l/c, it appears that $\zeta \to 0$ as $k \to \infty$. The aerodamping tending to zero at very high reduced frequencies is attributed to the blades being too stiff to be affected by the flow [37].

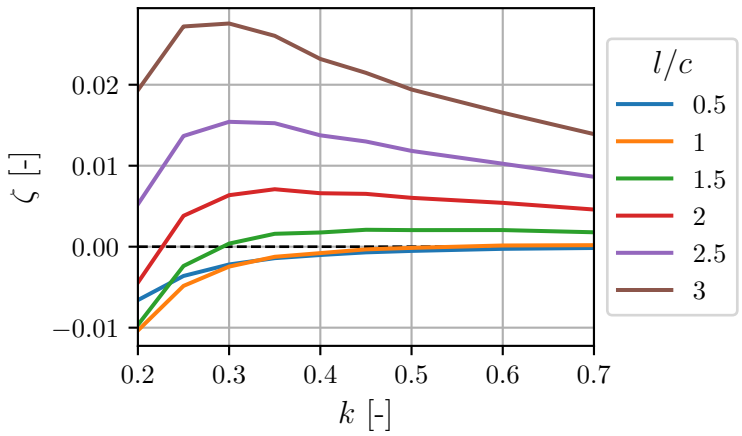


Figure 6.16: Aerodamping as function of k for different l/c

Figure 6.17 shows aerodamping as a function of twist axis setback for different k at constant inter-blade phase angle $\sigma_m = 40°$. It can be seen that for $k = 0.7$ the aerodamping is monotonic and follows a parabolic trend in l/c. The same, however, cannot be said for $k = 0.2$, where the aerodamping is decreasing in the range $0.5 < l/c < 1.2$, at which point it reaches a local minimum, and then increases rapidly up towards $l/c = 3$. There also exists a local minima for $k = 0.25$ and $k = 0.3$ at slightly smaller l/c. It is particularly interesting that the minimum aerodamping does not occur at the lowest value of l/c. This indicates that the pure twist mode shape is more stable than a combined mode shape with a small plunge component. It can be concluded that it is the cross-coupling of forcing and vibration from the plunge and twist motion that causes the minimum aerodamping, confirming the results shown in [6]. The general conclusion is that increasing l/c is beneficial, as typical compressor blade 1F mode shapes will have large enough reduced frequencies and twist axis setbacks to be outside the range where increasing l/c will cause a decrease in the aerodamping, excluding a very poor design. It can also be seen that the critical l/c at which flutter occurs decreases as the reduced frequency increases. This shows the close dependency of reduced frequency and twist axis setback on flutter stability.

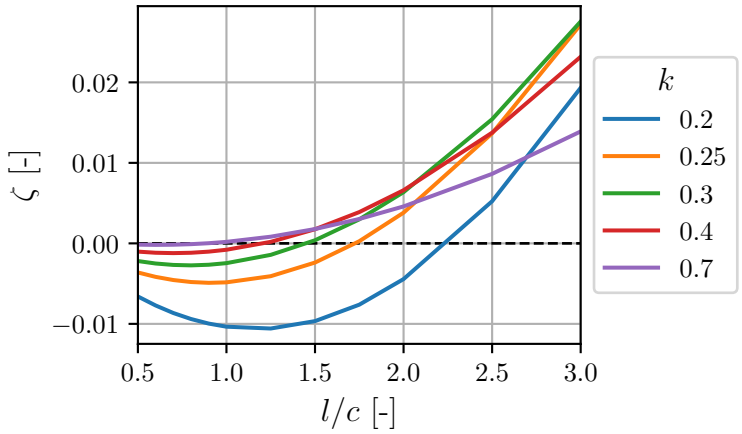


Figure 6.17: Aerodamping as function of l/c for different k

The effect of reduced frequency, twist axis setback and inter-blade phase angle are best summarised by a stability map. To build this map, the minimum aerodamping is chosen over the entire IBPA domain and plotted as a contour as a function of reduced frequency and twist axis setback as shown in figure 6.18. Regions of the contour shaded in red show negative aerodamping resulting in flutter and blue shaded regions show positive aerodamping in which the rotor is stable. The stability limit, where the aerodamping is zero, is highlighted for both the CFD and the experiment. There is a good agreement between the stability limit determined by CFD and experiment for the computed range reduced frequencies and twist axis setbacks. The most unstable mode shape is $k = 0.2$ and $l/c = 1$, whereas the most stable mode shape is $k = 0.3$ and $l/c = 3$. Despite the fact that generally, increasing the reduced frequency and twist axis setback is beneficial for preventing flutter, the most stable mode shape has a rather low reduced frequency and high twist axis setback. Therefore, for this cascade, it may be beneficial to sacrifice some of the blade stiffness for a mode shape with a large plunge component, so the aerodamping is at its most stable value. The shape of the flutter stability limit appears to follow some offset rectangular hyperbola of k and l/c, which is similar to conclusions drawn from the literature [36].

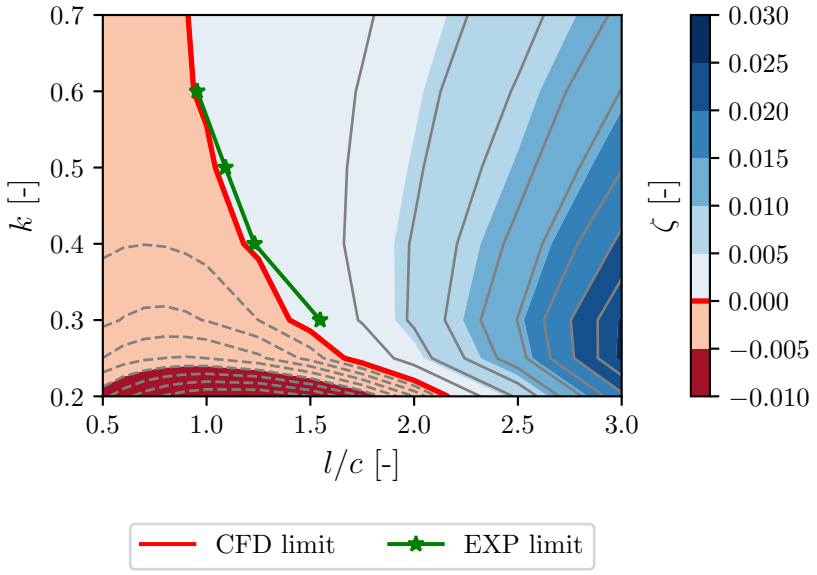


Figure 6.18: Flutter stability map

6.3.4 Validation of Linear Cascade Approach

The linear cascade aims to approximate the two-dimensional flow and mode shape for a section cut of a low-speed compressor rotor in the tip region. However, the implementation of a linear cascade means some of the flow features differ from those that would typically be seen in a low-speed compressor. The primary differences are the viscous circumferential boundaries (top and bottom walls of the measurement section), the linear hub and tip geometry, and the viscous walls on the hub and tip. The viscous circumferential boundaries not only mean there is zero circumferential periodicity but also introduce a non-uniform blade loading to the blade row. The linear hub and tip geometry are also not representative, as this geometry prevents periodicity in the flow. Finally, the viscous walls on the hub and tip and the implementation of a short blade span mean that the flow is no longer representative of a section cut in the tip region, as a large span-wise boundary layer is present. Aside from the changes to the cascade geometry, the non-uniform blade loading questions the validity of the implementation of the AIC method, as the blades are technically not tuned and therefore the linear superposition of forcing does not hold true. To assess the validity of the linear cascade and the implementation of the AIC method, four cascade implementations are investigated.

Case A

Case A implements the linear cascade, which is representative of the experimental setup. For the sake of completeness, the cascade implementation is summarised here. For this case, there are viscous hard walls on the hub and tip and viscous walls on the circumferential boundaries (top and bottom walls of the measurement section). The blade row is formed of 11 blades, and seven blades are used for determining the aerodamping using the AIC method. It was shown in figure 6.11 that for this case, there is a non-uniform blade loading across the blade row. Therefore, there are a few considerations that must be made about the validity of the AIC method. Firstly, it is assumed that the blades far away from the central vibrating blade have a small amplitude of modal forcing and contribute very little to the aerodamping. Secondly, it is assumed that the nearest neighbouring blades to the vibrating blade 0 have a similar steady aerodynamic loading and therefore can be considered tuned.

Case B

Case B implements an annular cascade setup, which aims to be more representative of a low-speed compressor cascade. For this case, the linear hub and tip geometry are replaced with an annular geometry with a diameter $D = 1$m which introduces flow three-dimensionality but maintains zero radial velocity. The viscous circumferential boundaries are replaced with periodic boundaries, which eliminate the non-uniform blade loading present in the linear cascade. Therefore, the rotor can now be considered fully tuned rather than approximating a tuned system. Finally, the viscous hub and tip boundary conditions are replaced with inviscid wall boundary conditions. This removes the large span-wise boundary layer present in the linear cascade and makes the flow more representative of a section cut of a compressor blade in the tip region. In this case, an AIC method is implemented to determine the aerodamping. To maintain similarity to the AIC method implemented for the linear cascade, 11 blades are placed in the blade row, and seven blades are used in determining the aerodamping.

Case C

Case C has an identical domain to that of Case B. The only difference between the two is that the aerodamping for case C is calculated using a work done method with phase-lagged boundary conditions. The reason for

implementing this case is to determine whether the 11 blades in the blade row and the 7 blades used in the calculation of the travelling wave mode coefficients are sufficient to correctly predict the aerodamping.

Case D

Case D implements the program code LINSUB developed by Whitehead [72]. The original implementation calculates forces and moments about the leading edge, which for this case is adapted to forces and moments around the twist axis as shown in [73]. This code implements an analytical method to determine the unsteady lift and moment for a cascade of flat plates vibrating in pure plunge motion perpendicular to the chord and pure twist motion about half chord. The implementation assumes that the flow is two-dimensional and the flat plates are operating at zero incidence. In order to have a better comparison of results, the aerodynamic response and mode shape for the two-dimensional section are spread in the span-wise direction to create a quasi-two-dimensional domain. The span of this domain is equal to those of cases A, B, and C. This allows the aerodamping ratio to be of the same magnitude as in the previously mentioned cases. This code is implemented primarily to assess whether the blade geometry of the linear cascade, such as the camber and thickness profile, has a considerable effect on flutter stability compared to flat plates. Additionally, this code implements zero flow incidence, which can be compared to the $i = 2°$ flow incidence of the linear cascade.

For each of the cases stated above, some properties of the cascade are fixed between implementations:

- Mode shape: All blades will vibrate in a combined plunge-twist mode shape with equal vibration amplitude.
- Operating point: The inlet Mach number is fixed to $M_i = 0.087$ and the incidence is fixed to $i = 2°$ (excluding case D which has $i = 0°$)
- Domain: The span, chord, stagger angle and blade profile (excluding case D which are flat plates)
- Solver parameters: Similar mesh densities, same time step and turbulence model.

Figure 6.19 shows the blade surface pressure coefficient profiles for the linear cascade setup (case A) and the annular cascade setups (cases B and C). It can be seen that the annular cascade implementation has a crossover of

the pressure and suction sides at approximately $x/c = 0.16$ which indicates that the annular cascade setup is operating at an incidence significantly below the design point. The linear cascade setup does not have a crossover due to the pressure gradient that exists in the linear cascade. This is particularly interesting as cases A, B, and C are all operating at the same incidence, but the pressure gradient in the linear cascade appears to act as a change in incidence. The loading of the blades is reasonably similar towards the trailing edge. Figure 6.20 shows the annular cascade (case B,C) mid-span pressure coefficient contour. It can be seen that there is no longer a circumferential pressure gradient on the blades, and each blade in the cascade has a uniform loading and can be considered tuned.

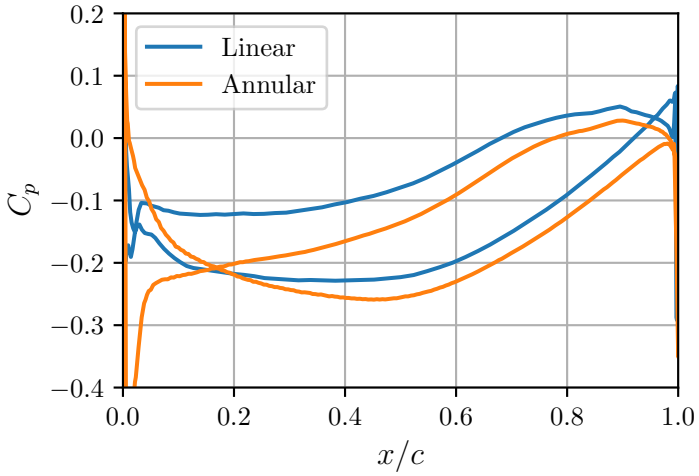


Figure 6.19: Comparison of mid-span blade surface pressure coefficient profiles for the linear cascade and annular cascade

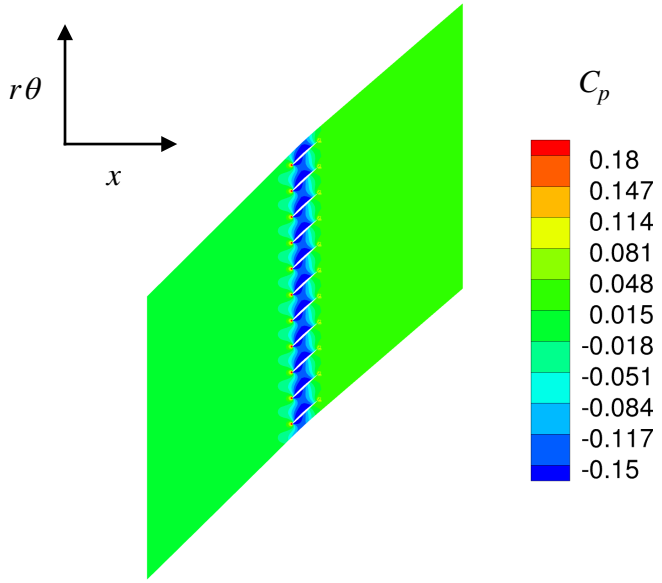


Figure 6.20: Annular cascade mid-span pressure coefficient contour

Figure 6.21 shows how the aerodamping varies as a function of the inter-blade phase angle for cases A-D with $k = 0.4$ and $l/c = 1$. There is generally good agreement in the trends of aerodamping as a function of IBPA. There is a good agreement in the amplitude of minimum aerodamping for cases A, B, and D, but a slightly more unstable aerodamping for case C. There is also a slight discrepancy in the IBPA, in which the minimum aerodamping occurs. The minimum aerodamping occurs at approximately 53°, 32°, 48°, and 37° for cases A,B, C, and D, respectively. Interestingly, in the region where the aerodamping is negative, the agreement between cases B and C is quite poor. These cases have an identical domain, but case B implements an AIC method and case C implements a work done method with phase-lagged boundary conditions to determine the aerodamping. It is concluded that the inclusion of seven blades in calculating the aerodamping via an AIC method may not be sufficient to correctly predict the aerodamping. The aerodamping for case D, which implements an entirely analytical method, has a good agreement with the aerodamping from cases determined by high-fidelity CFD. This shows that the small incidence $i = 2°$, blade camber and thickness profile, and three-dimensionality of the flow do not have an important role to play in determining the aerodamping for this cascade.

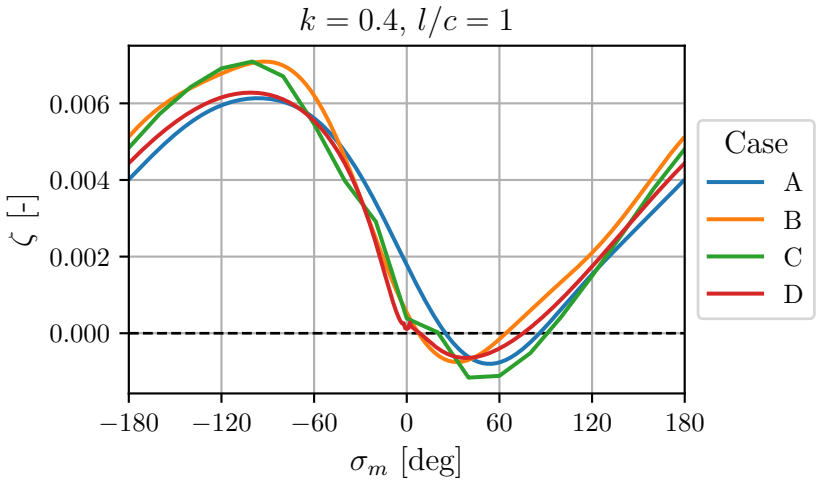


Figure 6.21: Aerodamping as a function of inter-blade phase angle for cases A–D

The stability maps for each cascade implementation are now compared for a range of reduced frequencies and normalised twist axis setbacks in figure 6.22. For this case, the inter-blade phase angle is fixed to $\sigma_m = 40°$. It can be seen that the contours of aerodamping are very similar in each case. The additional benefit of case D is that the implementation is purely analytical and can run a large number of reduced frequencies and twist axis setbacks very quickly. This is the reason that the aerodamping contour is significantly smoother than those for cases A, B, and C. In addition to there being a good agreement for the contours of aerodamping, the location of the stability limit is very similar for all cases. This shows that the change in the steady aerodynamic loading between cases A and B and C does not have a large effect on flutter stability. It also shows that the aerodamping of the linear cascade can be well approximated by simple analytical methods, such as that shown in case D. Finally, it shows that the AIC method is an effective method for predicting the aerodamping, despite the fact that the linear cascade is technically not tuned due to the non-uniform loading across the blade row.

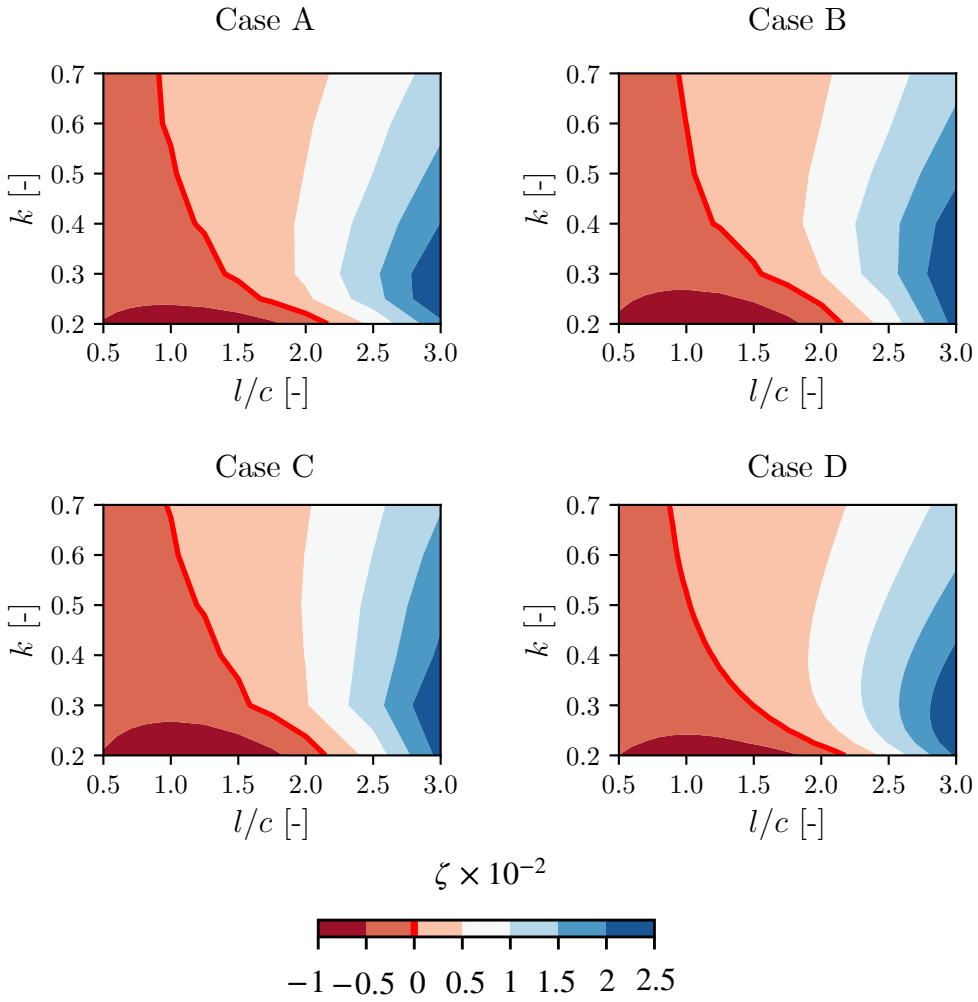


Figure 6.22: Flutter stability maps for cases A–D

6.4 Chapter Summary

CFD validation against experimental data highlights good agreement in steady pressure, unsteady pressure, and aerodamping across various mode shapes. Flutter analysis reveals low nodal diameter forward travelling wave modes as most unstable, with increased reduced frequency generally aiding flutter prevention. Travelling wave mode coefficient analysis indicates decreased reduced frequencies affect unsteady disturbances' propagation and aerodamping. Larger plunge-twist ratios are generally beneficial for flutter prevention. A stability map shows optimisation potential by sacrificing blade stiffness

for higher plunge-twist ratios. Concerns arise regarding the linear cascade's representativeness, but validation across multiple cascade implementations affirms the effectiveness of the aerodynamic influence coefficient method for predicting aerodamping. Analytical methods like LINSUB prove effective for predicting flutter, offering a faster alternative to high-fidelity CFD.

7 Flutter Model for Cascade Flows

The unsteady response and associated aerodamping of a combined plunge-twist mode shape have been shown to be driven by the reduced frequency k, normalised twist axis setback l/c, and inter-blade phase angle σ_m. The results of the previous chapter culminated in the creation of a flutter stability map. This map showed how blade manufacturers should design blades to decrease the likelihood of flutter and also showed where the flutter stability limit occurs. Engine manufacturers are particularly interested in the location of the flutter stability limit, as this is the boundary that must be moved in order to create flutter stable engine designs. It was also shown that the shape of the flutter stability limit for a subsonic linear cascade followed some rectangular hyperbola of k and l/c for the most unstable inter-blade phase angles, although there was no physical explanation for this observation. A key element in the prevention of flutter is not only to examine trends but also to provide a physical explanation of the phenomena to prevent flutter in future designs. To explain such trends, engine designers often look to flutter models, which simplify the highly complex interaction of the mode shape and unsteady aerodynamics to aid in developing useful conclusions. Therefore, the aims of this chapter are as follows:

1. Define a flutter model based on simplified physical modelling of the unsteady aerodynamic response and its interaction with the mode shape
2. Validate the model assumptions for the subsonic linear cascade
3. Apply the model to explain the shape and location of the flutter stability limit for the subsonic linear cascade in terms of k, l/c and σ_m
4. Define a general flutter stability parameter which can be used to advise future designs

7.1 Model Definition

Before the model is defined, the combined 1F mode shape is summarised. A 1F mode shape can be approximated by a combined plunge-twist mode shape with pure plunge vibration perpendicular to the chord and pure twist vibration about half chord blade centre. Under the assumption that the components are in phase and the blades are rigid bodies, the vibration of the combined mode can be considered a SDOF rotation about a twist axis located a distance l downstream of the leading edge. To simplify the terms

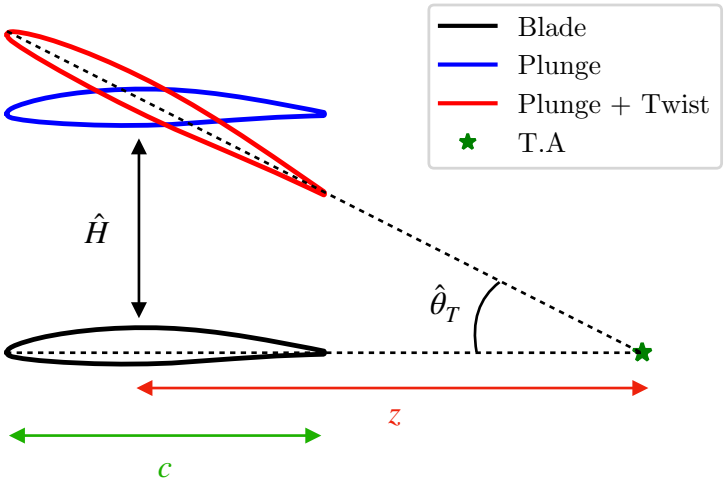


Figure 7.1: Schematic of twist vibration induced incidence parameters

of the model, the twist axis setback l has been replaced by the half-chord twist axis setback z, where $z = l - c/2$.

To begin the development of the flutter model, it was hypothesised that the aerodynamic response is driven by the vibration induced flow incidence on the blades. As was just mentioned, the 1F mode shape can be considered a superposition of plunge and twist components. Therefore, both the plunge and twist components of the mode will generate their own vibration induced incidence onto the blades. Let $\alpha_P(t)$ and $\alpha_T(t)$ be the incidence induced by plunge and twist vibration, respectively. A schematic of the blade vibration and the key parameters for the twist vibration motion are shown in figure 7.1. For twist vibration, a clockwise twisting displacement causes an increase in the relative incidence. Therefore, the incidence change due to twist vibration α_T can be defined by the twist angle of the SDOF rotation as a function of time, as shown by equation 7.1.

$$\alpha_T(t) = \theta_T(t) = \frac{\hat{H}}{z} \sin(\omega t) \tag{7.1}$$

It was shown by Cumpsty [74] that the plunge vibration induced incidence can be determined in velocity space. A schematic of the blade vibration and the key parameters for the plunge mode are shown in figure 7.2. In this figure, the blade has zero displacement and a maximum upward plunge velocity. The plunge velocity causes a decrease in the relative incidence; therefore, the plunge vibration induced incidence $\alpha_P(t)$ is out of phase with the plunge velocity. The plunge incidence can therefore be defined as the

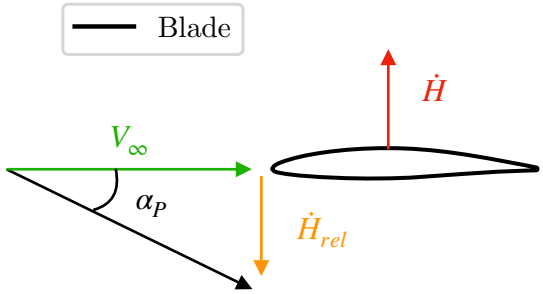


Figure 7.2: Schematic of plunge vibration induced incidence parameters

angle created between the inlet flow velocity V_∞ and the relative plunge velocity $\dot{H}_{rel}$, where $\dot{H}_{rel} = -\dot{H}$. It is assumed that the flow incidence is small, and therefore V_∞ and $\dot{H}$ are perpendicular vectors. Additionally, the assumption of a small incidence means that the rotor is guaranteed to be operating on a positive slope of the lift-incidence curve. This is critical as it means an increase in incidence causes an increase in the unsteady lift, which is not true when the slope of the incidence curve is negative near stall [35]. Let the plunge displacement and velocity perpendicular to the blade chord be given by equations 7.2 and 7.3, respectively. Finally, the plunge incidence can be defined by equation 7.4.

$$H(t) = \hat{H} \sin(\omega t) \tag{7.2}$$

$$\dot{H}(t) = \omega \hat{H} \cos(\omega t) \tag{7.3}$$

$$\alpha_P(t) = \frac{-\dot{H}(t)}{V_\infty} = \frac{k\hat{H}}{c} \cos(\omega t - \pi) \tag{7.4}$$

Now that the incidence change due to the vibration is defined, the variables that characterise the aerodynamic response must be defined. It was shown in chapter 5 that the work done per vibration cycle – and subsequently the aerodamping ratio – can be split into four components called forcing-vibration pairs. These terms are the aerodamping due to plunge and twist vibrations, which induce an unsteady lift and moment. The same procedure for splitting the aerodamping into these components will be followed here. Therefore, the aerodynamic response is defined as the unsteady lift acting at the centre of pressure and the unsteady moment about the half-chord blade centre.

The unsteady lifts and moments due to plunge and twist vibration will first be examined in the quasi-steady limit for a single blade. Quasi-steady analysis examines the vibration and response as $k \to 0$. For this implementation, this means that the instantaneous response is equal to the steady-state solution at that incidence. This is equivalent to there being no phase lag between the vibration and the unsteady response. Firstly, the amplitude of the quasi-steady lifts and moments must be defined. It is assumed that the amplitude of unsteady lift and unsteady moment generated due to plunge and twist vibration will be proportional in amplitude to the vibration induced incidences $\hat{\alpha}_P$ and $\hat{\alpha}_T$, respectively. For example, if the amplitude of the plunge vibration induced incidence $\hat{\alpha}_P$ increases by a factor of two, then the amplitude of unsteady lift due to plunge also increases by a factor of two. Each of the forcing-vibration pairs will therefore have a constant of proportionality K to model this linearity, which can be thought of as the gradient of the lift-incidence curve.

Secondly, the phase of the quasi-steady lifts and moments are defined. Since the aerodynamic response is being examined quasi-steadily, there is zero phase lag between the unsteady lift and unsteady moment and the plunge and twist incidence which generated it. Therefore, the quasi-steady lifts and moments due to plunge and twist vibration can be defined by equations (7.5)–(7.8).

$$L_P^{QS}(t) = K_{P,L}\alpha_P(t) = K_{P,L}\frac{k\hat{H}}{c}\cos(\omega t - \pi) \tag{7.5}$$

$$L_T^{QS}(t) = K_{T,L}\alpha_T(t) = K_{T,L}\frac{\hat{H}}{z}\sin\omega t \tag{7.6}$$

$$M_P^{QS}(t) = K_{P,M}\alpha_P(t) = K_{P,M}\frac{k\hat{H}}{c}\cos(\omega t - \pi) \tag{7.7}$$

$$M_T^{QS}(t) = K_{T,M}\alpha_T(t) = K_{T,M}\frac{\hat{H}}{z}\sin\omega t \tag{7.8}$$

Throughout this chapter, it is assumed that $K_{P,L} = K_{T,L}$ and $K_{P,M} = K_{T,M}$, so the amplitudes of quasi-steady lift and moment are independent of the vibration motion that generated them. In other words, the lift generated by plunge or twist vibration is equal, provided the plunge or twist vibration generates the same incidence. Figure 7.3 shows an example of the quasi-steady lifts and moments for a single blade vibrating in a combined mode shape over one vibration cycle.

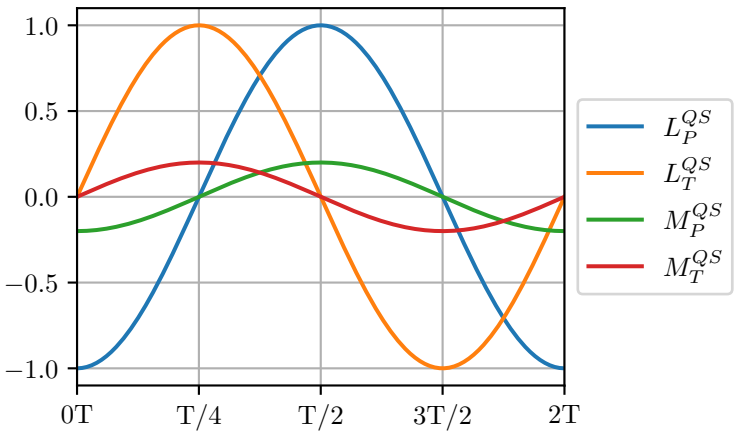


Figure 7.3: Quasi-steady lift and moment due to combined plunge and twist vibration for a single vibration cycle

The downside of the quasi-steady approximation is that the frequency cannot be approximated as zero for unsteady analysis. In reality, there will always be a phase lag between the vibration of the blade and the aerodynamic response. Therefore, to continue the analysis, a phase lag ϕ, which is currently unknown and dependent on reduced frequency, is added to the quasi-steady aerodynamic response from equations (7.5)–(7.8) to give the unsteady lifts and moments shown in equations (7.9)–(7.12). It is important to note here that this phase lag is the delay in the response behind the quasi-steady state response. Therefore, as the reduced frequency tends to zero, the phase lag also tends to zero and recovers the quasi-steady response.

$$L_P(t) = K_{P,L}\frac{k\hat{H}}{c}\cos\left(\omega t - \pi + \phi_{P,L}\right) \tag{7.9}$$

$$L_T(t) = K_{T,L}\frac{\hat{H}}{z}\sin\left(\omega t + \phi_{T,L}\right) \tag{7.10}$$

$$M_P(t) = K_{P,M}\frac{k\hat{H}}{c}\cos\left(\omega t - \pi + \phi_{P,M}\right) \tag{7.11}$$

$$M_T(t) = K_{T,M}\frac{\hat{H}}{z}\sin\left(\omega t + \phi_{T,M}\right) \tag{7.12}$$

To begin the aerodamping analysis, the modal forces f must be calculated from the unsteady lifts and moments by dotting the forces with the mode shape vector.

$$f_{P,L}(t) = K_{P,L}\frac{k\hat{H}^2}{c}\cos\left(\omega t - \pi + \phi_{P,L}\right) \tag{7.13}$$

$$f_{T,L}(t) = K_{T,L}\frac{\hat{H}^2}{z}\sin\left(\omega t + \phi_{T,L}\right) \tag{7.14}$$

$$f_{P,M}(t) = K_{P,M}\frac{k\hat{H}^2}{zc}\cos\left(\omega t - \pi + \phi_{P,M}\right) \tag{7.15}$$

$$f_{T,M}(t) = K_{T,M}\frac{\hat{H}^2}{z^2}\sin\left(\omega t + \phi_{T,M}\right) \tag{7.16}$$

Finally, the work done per vibration cycle for each component is calculated using equation 7.17, where $\dot{q}(t)$ is the modal velocity and $f_{comp}(t)$ is the modal force of the forcing-vibration component. The work done per vibration cycle for each component is shown in equations (7.18)–(7.21).

$$W_{comp} = \int_T f_{comp}(t)\cdot\dot{q}(t)dt \tag{7.17}$$

$$W_{P,L} = K_{P,L}\frac{k\hat{H}^2}{c}\hat{\dot{q}}\int_T \cos\left(\omega t - \pi + \phi_{P,L}\right)\cos\left(\omega t\right)dt \tag{7.18}$$

$$W_{T,L} = K_{T,L}\frac{\hat{H}^2}{z}\hat{\dot{q}}\int_T \sin\left(\omega t + \phi_{T,L}\right)\cos\left(\omega t\right)dt \tag{7.19}$$

$$W_{P,M} = K_{P,M}\frac{k\hat{H}^2}{zc}\hat{\dot{q}}\int_T \cos\left(\omega t - \pi + \phi_{P,M}\right)\cos\left(\omega t\right)dt \tag{7.20}$$

$$W_{T,M} = K_{T,M}\frac{\hat{H}^2}{z^2}\hat{\dot{q}}\int_T \sin\left(\omega t + \phi_{T,M}\right)\cos\left(\omega t\right)dt \tag{7.21}$$

The unknowns in the work done equations are the constants of proportionality K and the phase lag of the unsteady response ϕ. Therefore, equations (7.18)-(7.21) currently cannot be solved analytically and must be determined by CFD. Despite this requirement, the time integrals on the right hand side can be greatly simplified by looking at how the integrals vary with respect to the phase lag ϕ. Assign the work done per vibration cycle time integrals for each forcing-vibration pair to the variable D as shown in equations (7.22)–(7.25).

$$D_{P,L} = \int_T \cos(\omega t - \pi + \phi_{P,L}) \cos(\omega t) dt \tag{7.22}$$

$$D_{T,L} = \int_T \sin(\omega t + \phi_{T,L}) \cos(\omega t) dt \tag{7.23}$$

$$D_{P,M} = \int_T \cos(\omega t - \pi + \phi_{P,M}) \cos(\omega t) dt \tag{7.24}$$

$$D_{T,M} = \int_T \sin(\omega t + \phi_{T,M}) \cos(\omega t) dt \tag{7.25}$$

Figure 7.4 shows how D varies for each forcing-vibration pair as a function of their corresponding phase lags ϕ. It can be seen that $D_{P,L}$ and $D_{P,M}$ vary as a negative cosine function of the phase lag, and $D_{T,L}$ and $D_{T,M}$ vary as a sine function of the phase lag. Therefore, the time integrals can be simplified as shown by equations (7.26)–(7.29).

$$D_{P,L} = -\frac{1}{2f} \cos(\phi_{P,L}) \tag{7.26}$$

$$D_{T,L} = \frac{1}{2f} \sin(\phi_{T,L}) \tag{7.27}$$

$$D_{P,M} = -\frac{1}{2f} \cos(\phi_{P,M}) \tag{7.28}$$

$$D_{T,M} = \frac{1}{2f} \sin(\phi_{T,M}) \tag{7.29}$$

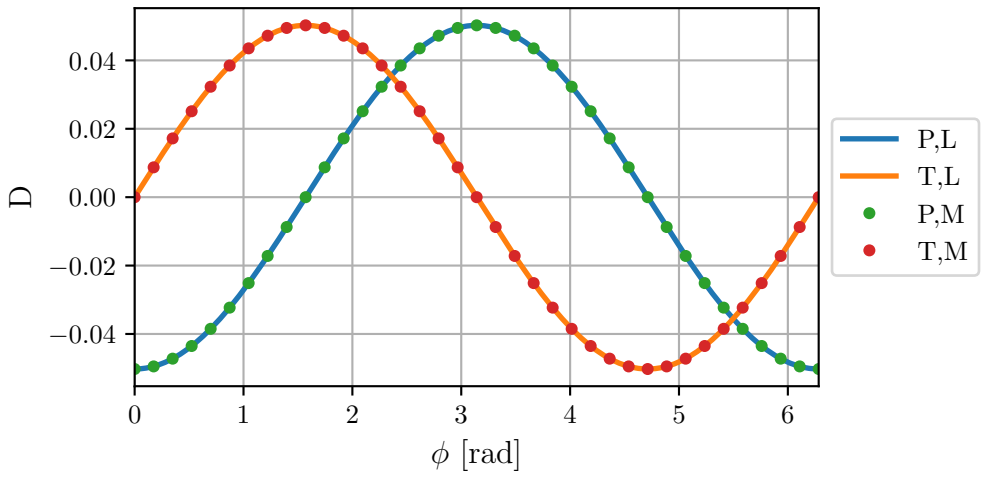


Figure 7.4: Time integral D as a function of phase

Finally, to complete the model, let the modal velocity amplitude be defined by equation 7.30 and substitute equations (7.26)–(7.29) into equations (7.18)–(7.21) and simplify to obtain the work done per vibration cycle terms for each forcing-vibration pair.

$$\hat{\dot{q}} = 2\pi f \tag{7.30}$$

$$W_{P,L} = -\pi K_{P,L} \frac{k\hat{H}^2}{c} \cos\left(\phi_{P,L}\right) \tag{7.31}$$

$$W_{T,L} = \pi K_{T,L} \frac{\hat{H}^2}{z} \sin\left(\phi_{T,L}\right) \tag{7.32}$$

$$W_{P,M} = -\pi K_{P,M} \frac{k\hat{H}^2}{zc} \cos\left(\phi_{P,M}\right) \tag{7.33}$$

$$W_{T,M} = \pi K_{T,M} \frac{\hat{H}^2}{z^2} \sin\left(\phi_{T,M}\right) \tag{7.34}$$

The work done per cycle terms shown in equations (7.31)–(7.34) will reproduce the exact work done for each forcing-vibration pair. This result shows that the work done due to plunge vibration is always stable, as the work done is negative, and the work done due to twist vibration is always unstable. These terms can be summed to give the total work done per cycle and determine the aerodamping ratio.

$$W = W_{P,L} + W_{T,L} + W_{P,M} + W_{T,M} \tag{7.35}$$

$$\zeta = -\frac{W}{2\pi\hat{\dot{q}}^2} \tag{7.36}$$

7.2 Validation and Simplification of the Model for a Subsonic Linear Cascade

To begin the validation, the values of K are found and compared to the assumptions made in the model. K can be found by dividing the amplitude of the unsteady lift and moment determined by CFD by the amplitude of the incidence that generated it, either $\hat{\alpha}_P$ for plunge or $\hat{\alpha}_T$ for twist. It was assumed in the definition of the flutter model that $K_{P,L} = K_{T,L}$ and $K_{P,M} = K_{T,M}$. This states that the amplitude of unsteady lift and moment are equal for plunge or twist vibration, provided they generate the same incidence. It is also assumed that the amplitude of the aerodynamic response is driven by the change in incidence; consequently, the values of K are assumed to be constant with respect to reduced frequency and twist axis setback. The procedure for determining K is as follows:

1. Values of reduced frequency k and twist axis setback l/c are chosen and the combined mode shape is built analytically.

2. The mode shape is then split into its pure plunge and pure twist components.

3. Two URANS simulation are run at the chosen operating point for the plunge and twist mode shape components.

4. $K_{P,L}$, $K_{T,L}$, $K_{P,M}$ and $K_{T,M}$ are found by dividing the amplitude of unsteady lift and moment by the twist vibration induced incidence which generated it.

5. This process is repeated for all k and l/c in the range $0.2 < k < 0.7$ and $0.5 < l/c < 3$.

Figure 7.5 shows how the constants of proportionality K varies as a function of reduced frequency k with $l/c = 1.5$. It can be seen from the figure that the assumption that $K_{P,M} = K_{T,M}$ is valid, but there is a slight discrepancy in the assumption that $K_{P,L} = K_{T,L}$, as $K_{T,L} > K_{P,L}$. Similarly, the assumption that the constants of proportionality do not change with reduced

frequency is valid for $K_{P,M}$ and $K_{T,M}$, but there is a slight negative gradient of $K_{P,L}$ and $K_{T,L}$ as the reduced frequency increases. Although the gradients themselves are small, the assumption is considered valid for this test case. Figure 7.6 shows how the constants of proportionality K vary as a function of twist axis setback l/c with $k = 0.4$. Again, similar to the variations in the reduced frequency case, the assumption that $K_{P,M} = K_{T,M}$ is valid but $K_{T,L} > K_{P,L}$. As the twist axis setback is increased, K does not vary, which validates the model assumptions. The conclusion to be drawn from these two figures is that the constants of proportionality K are approximately constant with respect to reduced frequency and twist axis setback. This shows that the amplitude of the aerodynamic response is in fact driven by the change in incidence due to the vibration of the blades. Additionally, it has been shown that $K_{P,L} \approx K_{T,L}$ and $K_{P,M} \approx K_{T,M}$, which states that the amplitude of unsteady lift and moment are equal for plunge and twist vibration, provided they generate the same incidence.

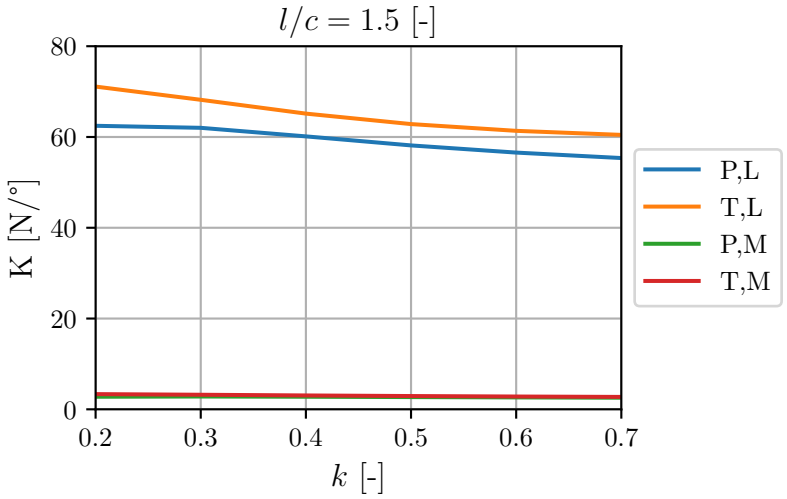


Figure 7.5: Constants of proportionality K as a function of reduced frequency k with $l/c = 1.5$

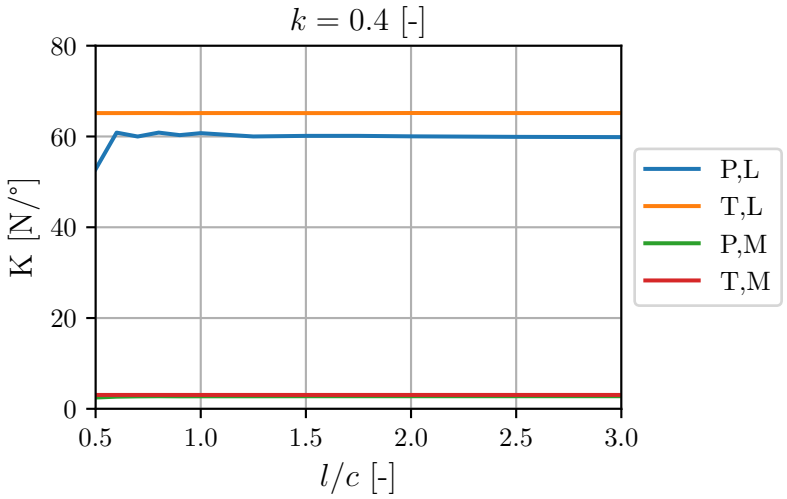


Figure 7.6: Constants of proportionality K as a function of twist axis setback l/c with $k = 0.4$

Now that K is known, the unknowns in the work done per cycle equations (7.31)–(7.34) are the phases of the unsteady lift and moment due to plunge and twist vibration. So far, the work done has been calculated for a single vibrating blade. For vibrating blades in a cascade, the phase of unsteady pressure will change depending on the inter-blade phase angle. Therefore, from this point onwards, the inter-blade phase angle is fixed to $\sigma_m = 40°$, and all model coefficients and conclusions drawn from this point onwards assume this inter-blade phase angle.

Figure 7.7 shows how the phase of unsteady lift due to plunge $\phi_{P,L}$, phase of unsteady lift due to twist $\phi_{T,L}$, phase of unsteady moment due to plunge $\phi_{P,M}$, and phase of unsteady moment due to twist $\phi_{T,M}$ vary as a function of k and l/c. It should be noted that the phase of unsteady lift and unsteady moment due to plunge have been neglected at $l/c = 0.5$, as the amplitude of unsteady lift and moment is zero for the pure twist mode shape. It can be seen from the figure that the phase of unsteady lift and moment is highly dependent on k and is a very weak function of l/c. Consider the case of a twist motion induced unsteady moment. For this case, the blade will always vibrate in pure twist mode, but as l/c increases, the amplitude of the blade vibration decreases. Since flutter is an inherently linear phenomenon, it is assumed that the vibration amplitude is proportional to the forcing. This results in the amplitude of the unsteady moment decreasing as l/c is increased. However, the phase of the unsteady moment remains the same, as the mode shape is identical but with a smaller amplitude. This result is not

unique to twist motion induced unsteady moments, as each of the forcing-vibration pairs has a phase that is approximately constant with respect to l/c. The phase of unsteady lift due to plunge $\phi_{P,L}$ and phase of unsteady moment due to plunge $\phi_{P,M}$ vary more greatly as a function of l/c compared to the twist components. Since these are the only two cases that use the unsteady pressures due to plunge, it is suspected that there is some local unsteady behaviour that is producing this phase change as a function of l/c. This could be something physical, such as large vibration amplitudes inducing some non-linearity into the flow, or something non-physical, such as plunge motion induced unsteady pressure amplitudes not being captured correctly at low l/c due to interference of numerical noise due to the small vibration amplitude. Either way, for the sake of model simplification, it is assumed that the phases of unsteady lift and moment can be determined solely as a function of reduced frequency.

It can also be seen from figure 7.7 that for $\sigma_m = 40°$, the phase lags behind the quasi-steady response are fairly small for all k and l/c in the region of interest. Therefore, in order to simplify the model for the subsonic linear cascade, it is assumed that a small angle approximation can be implemented for the sine and cosine terms of the phase lag in equations (7.31)–(7.34). The small angle approximation assumes that $\cos\phi = 1$ and $\sin\phi = \phi$. This is a simplified approach based on the frequency range of interest. This method could definitely be generalised, as in the work of Vega and Corral [75], who showed that the influence coefficient phase can be determined as an approximately linear function of reduced frequency. This could be used to create a linear mapping and generalise the model in terms of the inter-blade phase angle. However, for this simple case, a small angle approximation is reasonable in the frequency range of interest. Under the assumption that the phase is solely a function of reduced frequency and that a small angle approximation can be implemented, the work done per cycle equations can be transformed into those shown in equations (7.37)–(7.40).

$$W_{P,L} = -\pi K_{P,L} \frac{k\hat{H}^2}{c} \tag{7.37}$$

$$W_{T,L} = \pi K_{T,L} \frac{\hat{H}^2}{z} \phi_{T,L}(k) \tag{7.38}$$

$$W_{P,M} = -\pi K_{P,M} \frac{k\hat{H}^2}{zc} \tag{7.39}$$

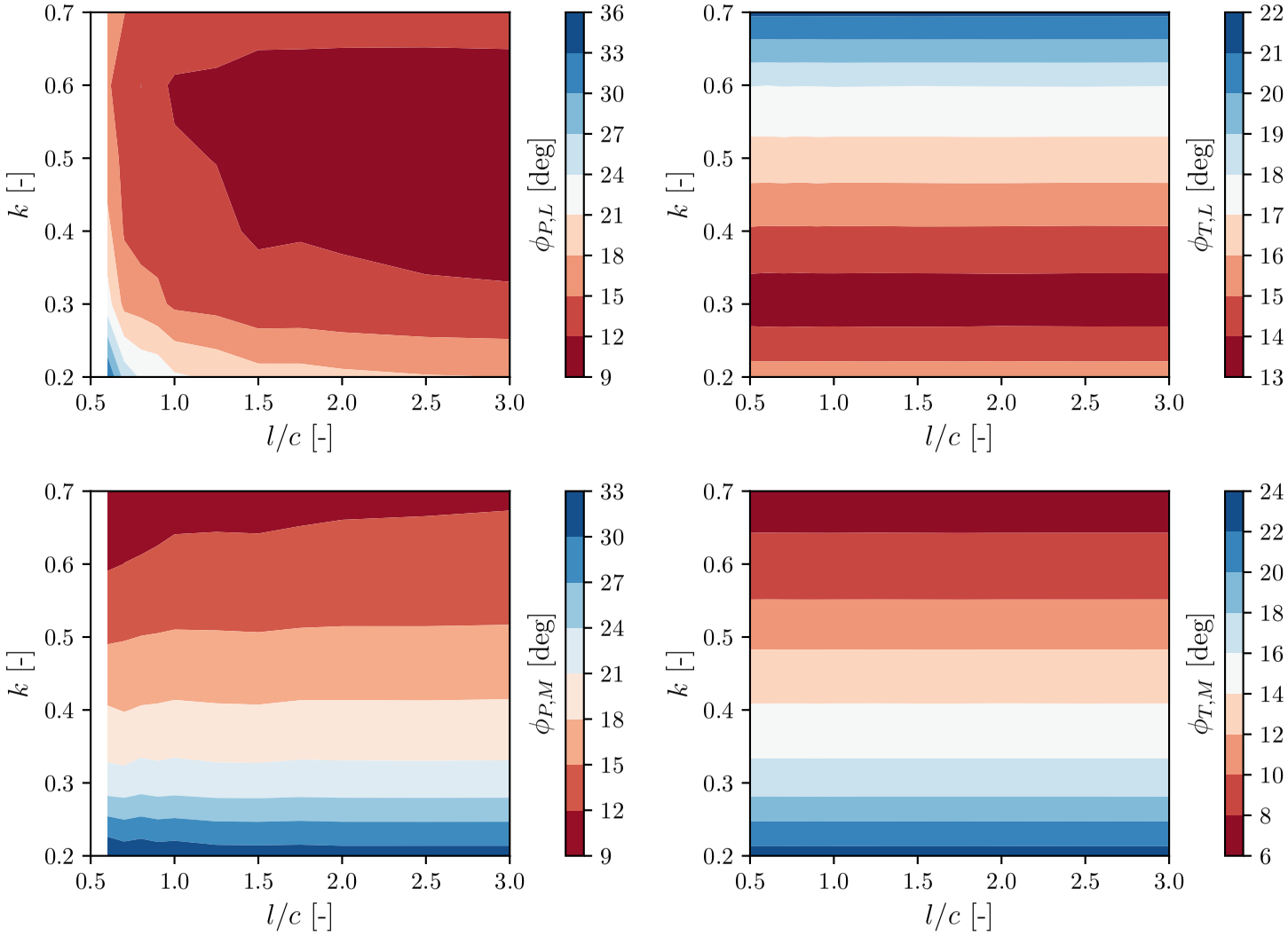


Figure 7.7: Contour maps of the phase of unsteady lift and moment due to plunge and twist vibration

$$W_{T,M} = \pi K_{T,M} \frac{\hat{H}^2}{z^2} \phi_{T,M}(k) \tag{7.40}$$

This simplification removes the phase lags due to plunge vibration induced unsteady lift $\phi_{P,L}$ and unsteady moment $\phi_{P,M}$ from the calculation of the work done. In addition, this shows that the aerodamping for any l/c can be determined as long as the phase lags for the twist induced unsteady lift and moment are known for the reduced frequency of the combined mode.

Finally, the simplifications made to the work done per cycle terms are validated by creating a stability map using the modified work terms and comparing the results to the purely CFD implementation of the subsonic linear cascade from the previous chapter. For the flutter model, the required inputs are the phase lags for the twist vibration induced unsteady lift as a function of reduced frequency $\phi_{T,L}(k)$ and the unsteady moment as a function of reduced frequency $\phi_{T,M}(k)$. These phase lags are determined by CFD. The selection of an l/c for determining the phase lags is arbitrary, so in this case, $l/c = 1$ was chosen. Figure 7.8 shows the stability map determined by the simplified work done per cycle terms shown in equations (7.37)–(7.40). It can be seen that there is a good agreement of amplitude of the minimum and maximum aerodamping for the simple model compared to the CFD-only approach. In addition, the shape of the contours is also very well predicted. The most important conclusion for this section is that the unsteady aerodynamics and the associated aerodamping are driven by the incidence change due to plunge and twist vibration and the phase lag of the twist vibration induced lift and moment.

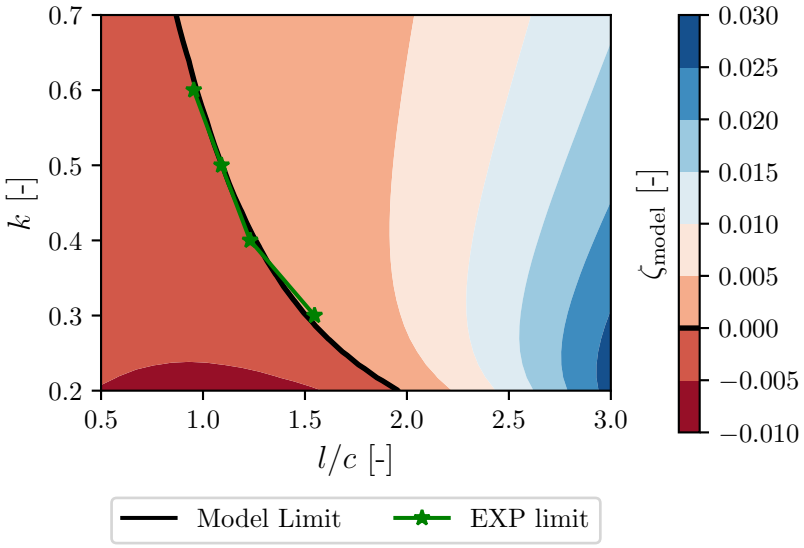


Figure 7.8: Flutter stability map produced using simple model

7.3 Shape and Location of the Flutter Stability Limit

It was shown in chapter 6 that the flutter stability limit followed some offset rectangular hyperbola of k and l/c, but there was no physical explanation for this trend. Therefore, the flutter model is now used to explain the shape and location of the flutter stability limit, where $W = 0$. By setting the sum of the work done per cycle terms shown in equations (7.37)–(7.40) to zero, the common constants can be removed.

$$W_{P,L} + W_{T,L} + W_{P,M} + W_{T,M} = 0 \tag{7.41}$$

$$-K_{P,L}\frac{kz^2}{c} + K_{T,L}z\phi_{T,L}(k) - K_{P,M}\frac{kz}{c} + K_{T,M}\phi_{T,M}(k) = 0 \tag{7.42}$$

As was previously stated, $K_{P,L} = K_{T,L}$ and $K_{P,M} = K_{T,M}$, as the amplitude of unsteady lift and moment are independent of the vibration motion which generates it, provided they induce the same incidence. Therefore

$$K_1 = K_{P,L} = K_{T,L} \tag{7.43}$$

$$K_2 = K_{P,M} = K_{T,M} \tag{7.44}$$

$$\delta = \frac{K_2}{K_1} \tag{7.45}$$

$$-\frac{kz^2}{c} + z\phi_{T,L}(k) + \delta\frac{kz}{c} - \delta\phi_{T,M}(k) = 0 \tag{7.46}$$

$$\frac{kz^2}{c} + z\left(\frac{\delta k}{c} - \phi_{T,L}(k)\right) - \delta\phi_{T,M}(k) = 0 \tag{7.47}$$

Equation 7.47 shows that the flutter limit can be described by a simple quadratic equation of z. There does exist a factorable solution, but only when $\phi_{T,L}(k) = \phi_{T,M}(k)$. However, it was shown in figure 7.7 that the phase lags are not identical for all reduced frequencies. Therefore, equation 7.47 is solved for z using the quadratic formula.

$$z = \frac{\left(\phi_{T,L}(k) - \frac{\delta k}{c}\right) \pm \sqrt{\left(\frac{\delta k}{c} - \phi_{T,L}(k)\right)^2 + \frac{4\delta k\phi_{T,M}(k)}{c}}}{2(k/c)} \tag{7.48}$$

$$\frac{kz}{c} = \frac{1}{2}\left(\phi_{T,L}(k) - \frac{\delta k}{c}\right) \pm \frac{1}{2}\sqrt{\left(\frac{\delta k}{c} - \phi_{T,L}(k)\right)^2 + \frac{4\delta k\phi_{T,M}(k)}{c}} \tag{7.49}$$

$$\frac{kz}{c} = A(k) \tag{7.50}$$

The solution shown in equation 7.50 gives a huge insight into the shape and location of the flutter stability limit. Firstly, this shows that the general shape of the flutter stability limit can be described by a non-standard rectangular hyperbola of the form $xy = A$. Where the x coordinate is the normalised half-chord twist axis setback z/c, the y coordinate is the reduced frequency k, and A is the right hand side of the quadratic equation $A(k)$. Given that $A(k)$ is a function of k, the flutter limit will vary from a standard rectangular hyperbola where A is constant. Therefore, the location of the flutter limit is determined by the amplitude of $A(k)$ and the shape is determined by how strong the gradient $A(k)$ is with respect to k. If the gradient of $A(k)$ with respect to k is zero, then a standard hyperbola is recovered, and the flutter limit will occur when kz/c is constant. Additionally, this result shows that there is a maximum of two crossings of $W = 0$ for a given reduced frequency, as the solution of the quadratic equation has only two solutions. However, the quadratic equation may only have one solution if the second solution results in a negative frequency.

Figure 7.9 shows how $A(k)$ varies as a function of k for the linear cascade. The unknowns $\phi_{T,L}(k)$, $\phi_{T,M}(k)$, δ are determined by CFD with an inter-blade phase angle $\sigma_m = 40°$. It can be seen that for this particular set of inputs, the amplitude of $A(k)$ is large compared to the gradient with respect to k. Therefore, the flutter stability limit will occur at an approximately constant value of kz/c, which can be well approximated by a standard hyperbola. The model predicts instability when kz/c is in the range (0.247 - 0.291).

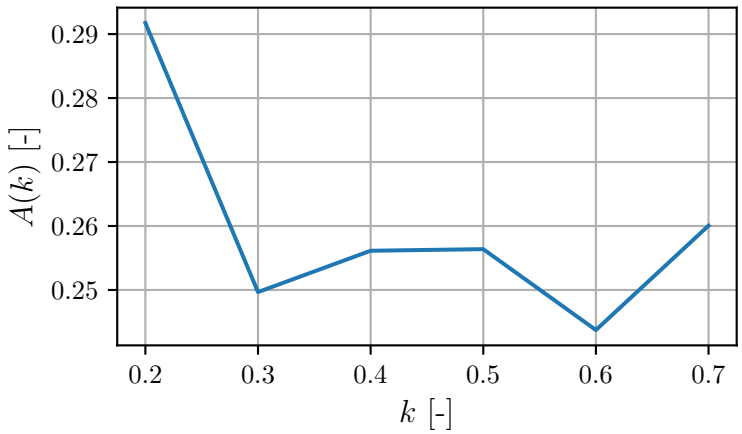


Figure 7.9: $A(k)$ as a function of reduced frequency

7.4 General Flutter Stability Parameter

It was shown in the previous section that the flutter stability limit can be approximated by the rectangular hyperbola of the form $kz/c = A(k)$. This result showed that generally, the flutter stability limit can be defined by the term kz/c, which is perturbed as a function of reduced frequency by $A(k)$. Therefore, a stability parameter is defined based on this conclusion. Let the stability parameter ξ be defined by equation 7.51.

$$\xi = \frac{kz}{c} \tag{7.51}$$

The definition of the flutter model was based on the assumption that the unsteady aerodynamic response is driven by the change in incidence on the blades due to both plunge and twist vibration. It was found that the terms of equation 7.51 can be rewritten in terms of the ratio of the plunge vibration

induced incidence $\hat{\alpha}_P$ and twist vibration induced incidence $\hat{\alpha}_T$ as shown in equation 7.52.

$$\xi = \frac{\hat{\alpha}_P}{\hat{\alpha}_T} = \frac{\omega \hat{H}/U}{\hat{H}/z} = \frac{kz}{c} \tag{7.52}$$

Consequently, the stability parameter ξ is named the 'plunge-twist incidence ratio'. Figure 7.10 shows the stability map for the linear cascade with lines of constant ξ plotted across the map. It can be seen that the flutter stability limit occurs at an approximately constant value of $\xi = 0.27$. This stability parameter merges the effect of plunge-twist ratio and reduced frequency into a single parameter and shows that modes with a large plunge-twist incidence ratio are stable, and modes with a small plunge-twist incidence ratio are unstable.

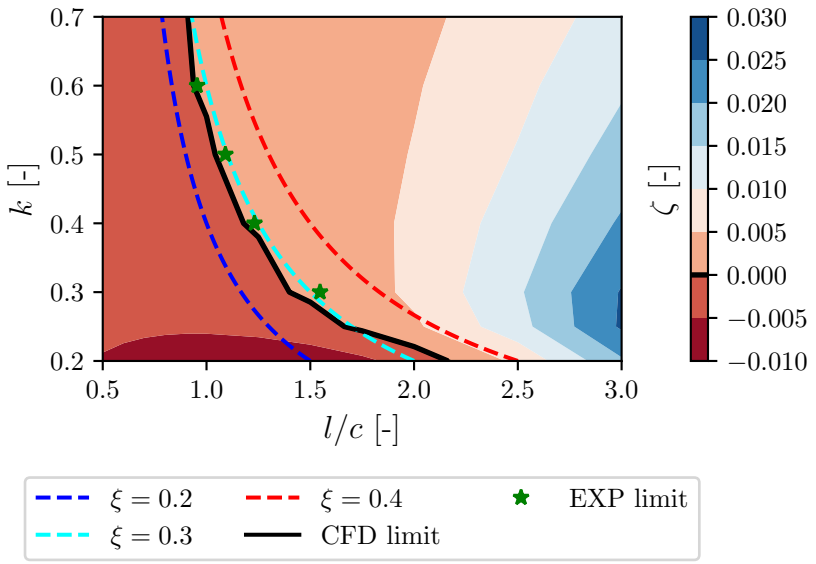


Figure 7.10: Flutter stability map including the stability parameter 'plunge-twist incidence ratio'

The conclusion that the flutter stability limit can be defined by a hyperbola of a plunge-twist ratio and reduced frequency has been determined before. Halliwell [29] defined a stability parameter, which will be named ξ_H as shown in equation 7.53

$$\xi_H = \frac{c\hat{\theta}_T}{k\hat{H}} \tag{7.53}$$

This stability parameter combines the twist-plunge displacement amplitude ratio $c\hat{\theta}_T/\hat{H}$ and the reduced frequency k into a single parameter. It was shown in figure 7.1 that the amplitude of the plunge vibration $\hat{H}$ can be rewritten in terms of the twist angle amplitude and half-chord twist axis setback. Therefore, Halliwell's stability parameter can be expressed as

$$\xi_H = \frac{c\hat{\theta}_T}{k\hat{H}} = \frac{c\hat{\theta}_T}{k\hat{\theta}_T z} = \frac{c}{kz} \tag{7.54}$$

$$\therefore \xi_H = \frac{1}{\xi} = \frac{\hat{\alpha}_T}{\hat{\alpha}_P} \tag{7.55}$$

Equation 7.55 shows that the stability parameter posed by Halliwell is in fact the reciprocal of ξ and consequently can be defined as the 'twist-plunge incidence ratio'.

7.5 Chapter Summary

A flutter model was developed based on the assumption that plunge and twist vibration induced incidence is responsible for the change in aerodynamic loading that causes flutter. It was shown that the amplitude of unsteady lift and unsteady moment is proportional to the vibration induced incidence, meaning that the unsteady response is in fact driven by the change in incidence. Additional assumptions based on the phase of unsteady pressure were made based on the results for the linear cascade. It was shown that the flutter stability limit can be defined by a non-standard rectangular hyperbola of reduced frequency and normalised twist axis setback. The hyperbola is defined as non-standard as it is still a weak function of reduced frequency. Further analysis showed that this hyperbola can be defined as the 'plunge-twist incidence ratio', which is the ratio of the amplitude of the plunge induced incidence and the twist induced incidence. In conclusion, it was stated that engine designers should aim to design blades with a large plunge-twist incidence ratio to ensure that flutter does not occur.

8 Effect of Steady-State Aerodynamic Loading on Flutter Stability

It was shown in the previous chapter that the flutter stability limit can be defined by the plunge-twist incidence ratio. For a weakly loaded subsonic linear cascade, the flutter stability limit occurred at an approximately constant incidence ratio $\xi = 0.27$. However, internal reports have shown that for a transonic fan, instability occurs when $\xi = 1$. There are many differences between the implementation of a subsonic linear cascade and a typical transonic fan, which will result in differences in the stability limit. Primarily, three-dimensional flow and mode shapes, increased loading, shock waves, and acoustic effects. In this chapter, the effects of steady loading are investigated. In order to bridge the gap between the two implementations, the effect of steady loading is investigated on a non-rotating, highly loaded two-dimensional compressor cascade. This maintains the two-dimensional flow features of the linear cascade, which allows easier comparison, while also introducing the two-dimensional flow features of transonic fans. In this chapter, the Mach number and incidence onto the blades are varied, and the effect on the aerodamping is investigated. The results from the two-dimensional cascade implementation can then be compared to results for three-dimensional rotating compressors from the literature to identify similarities and differences in the results.

8.1 Test Case

The geometry used throughout this chapter is the compressor cascade, 'standard configuration 10'. Standard configuration 10 is a purely two-dimensional compressor cascade, as proposed by Fransson and Verdon [76]. The profile is constructed by superimposing the thickness distribution of a modified NACA–0006 airfoil on a circular-arc camber line with a radius of camber $r = 0.2525$m. The blade chord is $c = 0.1m$, the pitch-chord ratio is $S/c = 1$, and the stagger angle is $\gamma = 45°$. The blade profile and periodic boundaries for a single passage are shown in figure 8.1. It can be seen that the sharp trailing edge variant of the blades has been plotted and will continue to be used throughout this chapter.

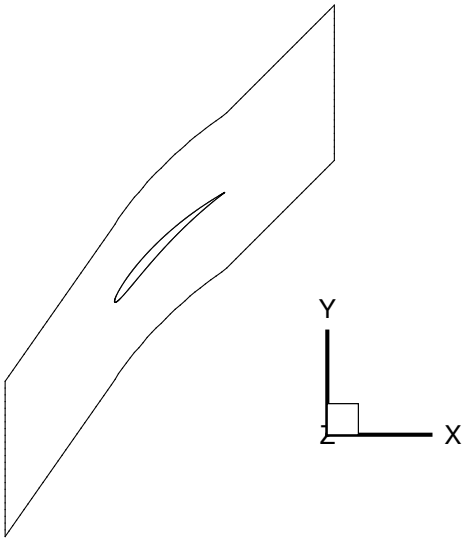


Figure 8.1: Two-dimensional blade geometry and periodic boundaries

This geometry was chosen because the cascade was designed to operate at both a subsonic and transonic operating point. The subsonic case has a design inlet Mach number of $M_i = 0.7$ and an incidence of $i = 10°$, whereas the transonic case has a design inlet Mach number of $M_i = 0.8$ and an incidence of $i = 13°$. The benefit of this, when looking at the effect of Mach number and incidence on flutter stability, is the knowledge that the blades have been designed to operate at more than one operating point. Whereas, the choice of a different geometry with only a single specific operating point would lead to obtaining results with unrealistic blade loading and a poorer comparison of results. This test case maintains most of the flow characteristics associated with the steady-state loading of a typical three-dimensional transonic compressor, such as shocks and separated regions on the suction side, but with a two-dimensional non-rotating geometry. The two primary differences are the lack of radial flow and mode shapes and radial acoustic modes.

8.2 Computational Implementation

Domain

The cascade is simulated as a quasi-two-dimensional annular cascade geometry with a large radius of 100 m and a small span of 25 mm. This radius was selected as it completely negates all three dimensionality of the flow.

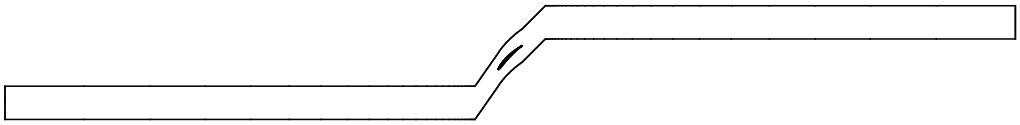


Figure 8.2: Extent of computational domain

The use of a quasi-two-dimensional domain is due to the implementation constraints of the flow solver. The choice of blade span is somewhat arbitrary, as inviscid boundary conditions are implemented on the hub and tip. The inlet and outlet boundaries are placed 14 chords upstream of the leading edge and downstream of the trailing edge, respectively. One-dimensional non-reflecting boundary conditions are implemented at the inlet and outlet boundaries, and the boundary condition for the blade is a viscous wall. The extent of the computational domain can be seen in figure 8.2. In this chapter, a work done method with phase-lagged boundary conditions is implemented to determine the aerodamping ratio. The vibration motion of the blades is resolved in time with 360 time steps per vibration cycle. The total inlet pressure and temperature are fixed at $p_0 = 101.3$ kPa and $T_0 = 300$ K, as in line with the default analysis for standard configuration 10. An iterative procedure is used to ensure the correct specified inlet Mach number. The procedure is as follows:

1. Define a target inlet Mach number (M_i).
2. Prescribe the total pressure ($p_{0,in}$), total temperature ($T_{0,in}$) and flow angle for the the inlet boundary condition.
3. Guess an outlet static pressure (p_{out}).
4. Run steady CFD and calculate the inlet Mach number for the corresponding pressure ratio.
5. If the calculated inlet Mach number is less than the target, decrease the outlet static pressure. If higher than the target, increase the static pressure.
6. Repeat from step 4 until the target Mach number is reached to within 0.001%.

Mesh

The mesh is semi-unstructured, with a large number of hexahedral elements in the boundary layer, prismatic elements in the near-field, and horizontally aligned hexahedral elements in the inlet and outlet ducts. The mesh is coarsened significantly towards the inlet and outlet boundaries to implement what is known as a 'sponge layer' to limit reflection of axially propagating acoustic waves, which are known to affect flutter stability [26]. For the sponge layer, a large axial distance is implemented for the first cell away from the inlet and outlet, with a length determined by the maximum wavelength of an expected propagating acoustic wave. While the upstream and downstream ducts have a significantly coarsened mesh, the prismatic near-field elements have a high density in the blade-to-blade passage to capture circumferentially propagating pressure waves. The domain is discretized radially by five mesh layers. Figure 8.3 shows the mesh convergence study for the transonic test case. For this study, six meshes were tested with an approximately constant increase in the number of nodes. For all meshes shown, the $y+$ is fixed to approximately 20. It was shown in [55] that use of this $y+$ value with a modified Spalart-Allmaras turbulence model gives the best agreement to experimental data near stall. In this study, the steady lift coefficient is chosen as the criteria for determining a mesh-independent solution. It can be seen that when the total number of nodes is greater than 192×10^3, the steady lift coefficient converges to a constant value. Therefore, this mesh is selected, as the solution is mesh-independent and has a much shorter computation time than the larger meshes. The final mesh has a total of 192×10^3 nodes with an average of $y+ = 19.86$.

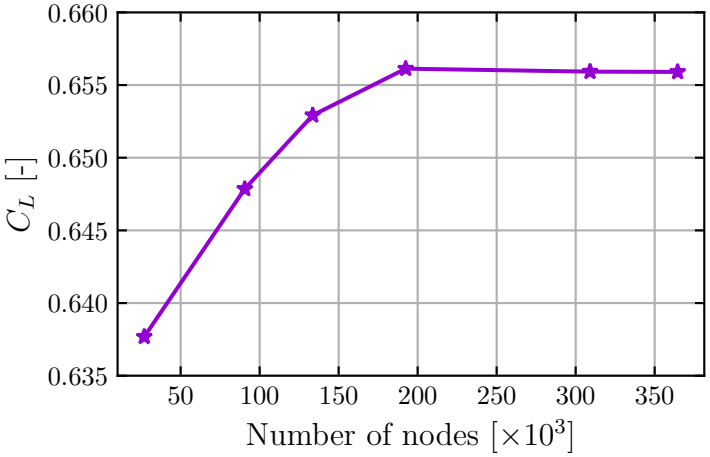


Figure 8.3: Mesh convergence study

Mode Shape

The mode shape used throughout this chapter is a quasi-two-dimensional combined plunge-twist mode shape which approximates a 1F mode. The following assumptions are made when defining the combined mode:

1. The 1F mode shape can be considered a superposition of plunge vibration perpendicular to the chord and twist vibration about half chord.

2. The vibration components are in phase, where plunge motion starts the vibration cycle with an upwards motion and the twist motion with a clockwise rotation, which acts to open the blade passage.

3. There is zero span-wise component in the mode shape.

4. The blades are rigid bodies.

Under these assumptions, the mode shape is equivalent to a single degree of freedom rotation about a twist axis located a chord-wise distance l downstream of the leading edge. A schematic of the implementation of the mode and the key parameters is shown in figure 8.4. Where T.A is the twist axis location, l is the twist axis setback, $\hat{H}$ is the plunge amplitude, A_{LE} is the blade leading edge amplitude, and $\hat{\theta}_T$ is the twist angle amplitude.

To allow post-processing into the aerodamping components shown in chapter 5, the pure plunge and pure twist components of the 1F mode shape

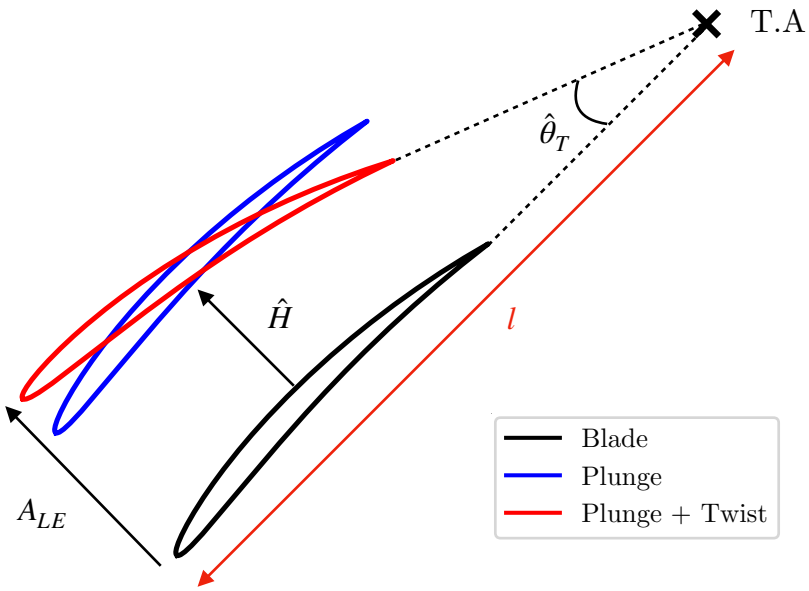


Figure 8.4: Schematic showing rigid body rotation about the twist axis (T.A)

must be implemented separately. To begin, the mode shape parameters of normalised twist axis setback l/c, reduced frequency k, and leading edge amplitude A_{LE} are selected. For all mode shapes in this chapter, the leading edge amplitude is set to $3\%c$. This amplitude was selected to be small enough not to introduce non-linearities in the flow but large enough to distinguish physical pressure perturbations from numerical noise. The twist angle amplitude $\hat{\theta}_T$ and the plunge amplitude $\hat{H}$ can be found directly from the input parameters as

$$\hat{\theta}_T = \arctan\left(\frac{A_{LE}}{l}\right) \tag{8.1}$$

$$\hat{H} = (l - c/2)\tan\left(\hat{\theta}_T\right) \tag{8.2}$$

Now that the displacement amplitudes of the plunge and twist motions are known, the modes can be implemented analytically for each node on the blade surface. Figure 8.5 shows a schematic of the implementation of the pure plunge mode with the relevant parameters. Where γ is blade stagger and $\kappa = \pi/2 - \gamma$. For the plunge component of the mode, each mesh node, i, must vibrate perpendicular to the chord with amplitude $\hat{H}$. Equation 8.3 shows the definition of the plunge mode shape for a single mesh node. This, in turn, is repeated for all mesh nodes on the blade surface.

$$\mathbf{\Phi}_{P,i} = \begin{Bmatrix} \hat{H}\cos(\kappa) \\ \hat{H}\sin(\kappa) \\ 0 \end{Bmatrix} \tag{8.3}$$

For the pure twist mode, a linearised rotation of axes method is applied to each mesh node on the blade surface, as shown in chapter 6. In this implementation, the origin of the rotation is set to half chord blade centre, which is assumed to be located at $(0, 0)$ on the x, y plane. Equation 8.4 shows the definition of the twist mode shape for a single mesh node i. This, in turn, is repeated for all mesh nodes on the blade surface.

$$\mathbf{\Phi}_{T,i} = \begin{Bmatrix} \hat{\theta}_T y_i \\ -\hat{\theta}_T x_i \\ 0 \end{Bmatrix} \tag{8.4}$$

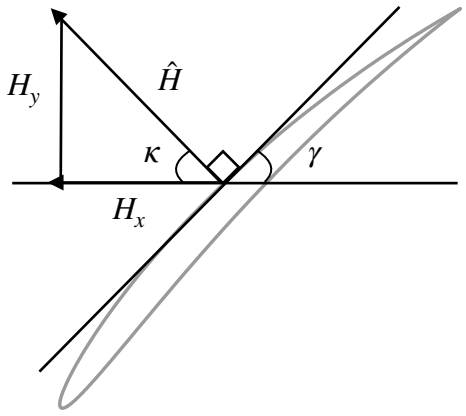


Figure 8.5: Schematic of pure plunge mode shape implementation

8.3 Validation

Due to the two-dimensional nature of the standard configuration 10 cascade, there is no experimental data for validation. Therefore, to validate the current work, the steady and unsteady flow results are compared against results from other aeroelastic flow solvers and implementations. Another downside is that the majority of validation cases in the literature for standard configuration 10 predominantly utilise inviscid flow solvers. Since this is not of interest in the present work, the validation of these cases has been neglected. One of the few papers to produce viscous aeroelastic results for this geometry was given by Repar et al. [77]. Therefore, this paper will be used to

validate the steady and unsteady CFD. Figure 8.6 shows the validation of the blade surface isentropic Mach number, given by equation 8.5, as a function of the normalised chord for the subsonic test case with $M_i = 0.7$ and $i = 10°$. There is a very good agreement between the CFD of the current work and the work of Repar. This shows that geometry and boundary conditions are implemented correctly and that the final mesh selected from the mesh convergence study converged to a comparable solution.

$$M_{isen} = \sqrt{\left(\left(\frac{p_0}{p}\right)^{\frac{\gamma-1}{\gamma}} - 1\right) \cdot \frac{2}{\gamma - 1}} \tag{8.5}$$

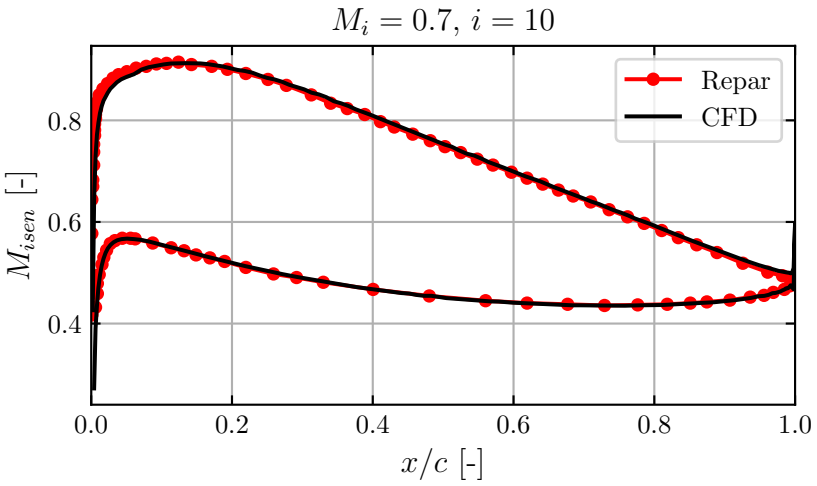


Figure 8.6: Isentropic Mach number validation of CFD against Repar [77]

Now the unsteady flow, vibration, and resulting aerodamping are validated. To allow a correct comparison of results, a different normalisation for the aerodamping ratio is defined, which matches that used in the literature. For this validation case, the aerodamping ratio is given by equation 8.6, where $C_p{}'$ is the unsteady pressure coefficient, $\boldsymbol{v}$ is the local blade velocity vector, and θ_T is the twist angle amplitude.

$$\zeta = \frac{\int \Im\left(C_p{}'\right) \boldsymbol{v} \cdot \boldsymbol{n} dA}{\theta_T c^2} \tag{8.6}$$

Figure 8.7 shows the aerodamping as a function of the inter-blade phase angle for the subsonic test case with $k = 0.5$ and $l/c = 0.5$. The aero-

damping from the current work is validated against the aerodamping calculated using both a 1D-NRBC and a 2D-NRBC from Repar. There is a reasonable agreement between the present CFD and the 2D-NRBC implementation. The magnitude of the aerodamping is well predicted in the range $-180° < \sigma_m < 70°$ and critically captures the spike in aerodamping in the region of $\sigma_m = 58.5°$ and $\sigma_m = -25°$. These two conditions correspond to an upstream and downstream circumferential acoustic resonant condition where no energy is lost to radiation in the axial direction [78]. The inter-blade phase angles for these resonant conditions can be estimated as shown by Whitehead [72] in equation 8.7.

$$\sigma_r = \left(M_\theta \pm \sqrt{1 - M_x^2}\right) \frac{Mk(S/c)}{1 - M^2} \tag{8.7}$$

This equation gives two inter-blade phase angles, one positive σ_r^+ and one negative σ_r^-, where the acoustic wave is cut on in the range $\sigma_r^- < \sigma_m < \sigma_r^+$. The resonant condition at $\sigma_m = 58.5°$ corresponds to the upstream resonant condition and $\sigma_m = -25°$ to the downstream resonant condition. Interestingly, the work of Repar does not seem to capture the negative inter-blade phase angle cut on condition, which is suspected to be due to poor resolution of the inter-blade phase angle. This explains why there is only a small spike in the current work, as the resonant condition is very sharp and occurs over a very small inter-blade phase angle range. There is a discrepancy for large inter-blade phase angles $\sigma_m > 70°$, which shows under-predicted aerodamping for the current CFD with a maximum under-prediction of 18.58% at $\sigma_m = 90°$. Although the aerodamping is under-predicted, the shapes of the aerodamping curves in this region are still comparable. On the other hand, there is poor agreement between the present CFD and the 1D-NRBC implementation from the literature. The magnitude of the aerodamping and the shape of the aerodamping curve are different across all inter-blade phase angles. The location of the minimum aerodamping, both in terms of the magnitude and the inter-blade phase angle at which it occurs, and the spike associated with the acoustic resonance is poorly predicted. In the present work, a 1D-NRBC is implemented at the inlet and outlet boundaries, but the mesh has been extended and coarsened upstream and downstream of the rotor to create a sponge layer that minimises reflections from axially propagating perturbations. This shows that the extension and coarsening of the mesh is an effective method for minimising reflections, which can modify the aerodamping. So much so that the results for the current implementation are comparable to implementing a 2D-NRBC.

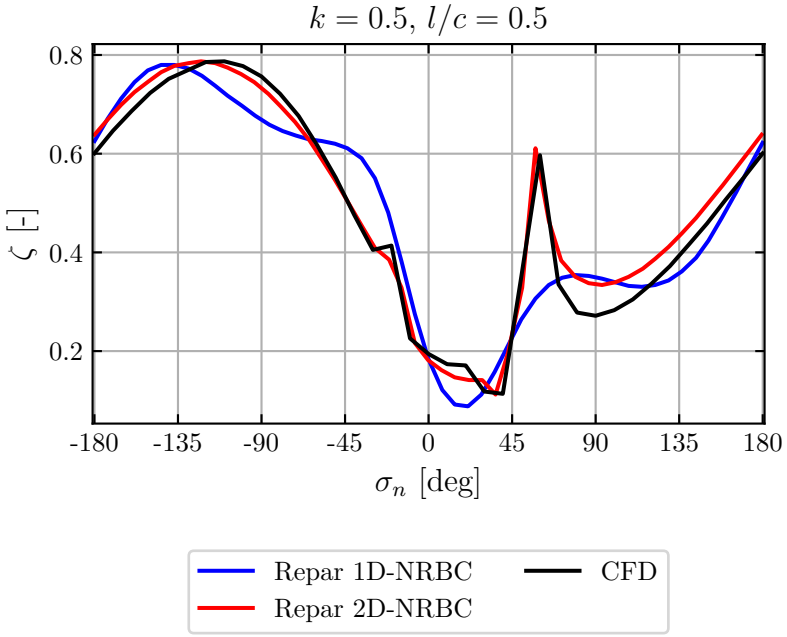


Figure 8.7: Aerodamping as a function of inter-blade phase angle validation of CFD against Repar [77]

8.4 Transonic Test Case Analysis

The majority of the work in this chapter focuses on the transonic test, which operates with a design inlet Mach number $M_i = 0.8$ and incidence $i = 13°$. In this section, the steady flow and interaction of unsteady flow and mode shape are investigated. This analysis informs the background understanding of the test case, which will be used when drawing conclusions from the variation of the inlet Mach number and incidence cases.

Figure 8.8 shows the steady state Mach number contour (left) and the blade surface isentropic Mach number as a function of normalised chord (right) for the transonic test case. It can be seen from the isentropic Mach number that there is a strong shock wave on the suction side at approximately $x/c = 0.25$. The iso-line of the shock, where $M = 1$, is highlighted in black on the Mach number contour. This shows that the cascade is unstarted, as the shock is expelled out of the blade passage. It can also be seen from the Mach number contour that the trailing edge has a region of separated flow due to trailing edge diffusion.

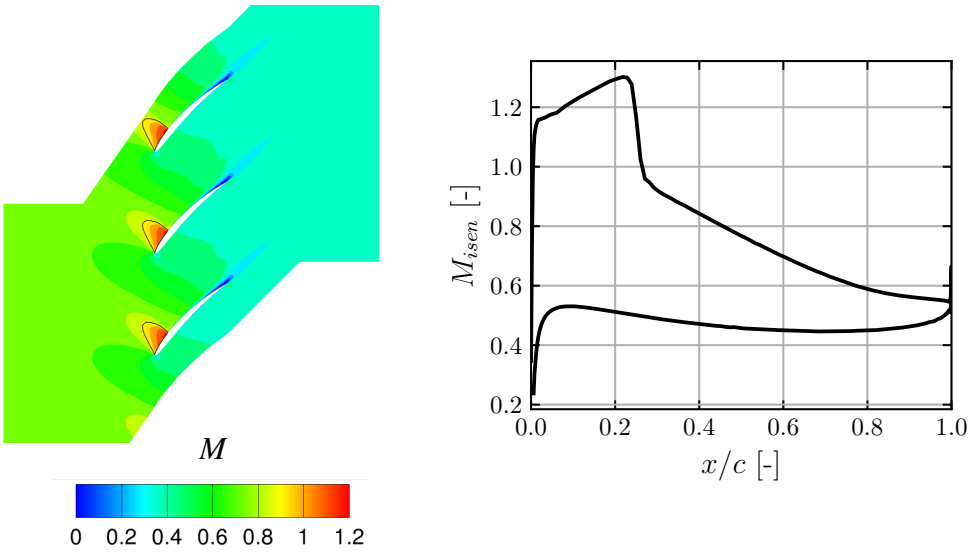


Figure 8.8: Steady state Mach number contour (left) and blade surface isentropic Mach number (right) for the transonic test case

Figure 8.9 shows a flutter stability map of work done per vibration cycle as a function of k and l/c for the transonic test case with $M_i = 0.8$ and $i = 13°$. For this particular inlet Mach number and incidence, the upstream acoustic wave has a cut on reduced frequency $k_{cut} = 0.11$ and the downstream acoustic wave has a cut on reduced frequency $k_{cut} = 0.28$. The lines of cut-on reduced frequency are labelled in figure 8.9. In general, low reduced frequencies and twist axis setbacks correspond to negative work done, whereas high reduced frequencies and twist axis setbacks correspond to positive work done as expected from the literature. It can be seen from the figure that the reduced frequency with the largest range of unstable l/c occurs at approximately $k = 0.3$, which corresponds to a reduced frequency just slightly above the downstream cut-on reduced frequency. Additionally, just above $k = 0.3$ at $l/c = 1$ is where the maximum destabilising work done per cycle occurs. Above and below this reduced frequency, the range of unstable l/c decreases. This is a particularly surprising solution, as it is expected from the literature that the least stable operating point should be one where the upstream acoustic wave is cut on, and the downstream acoustic wave is cut off [6].

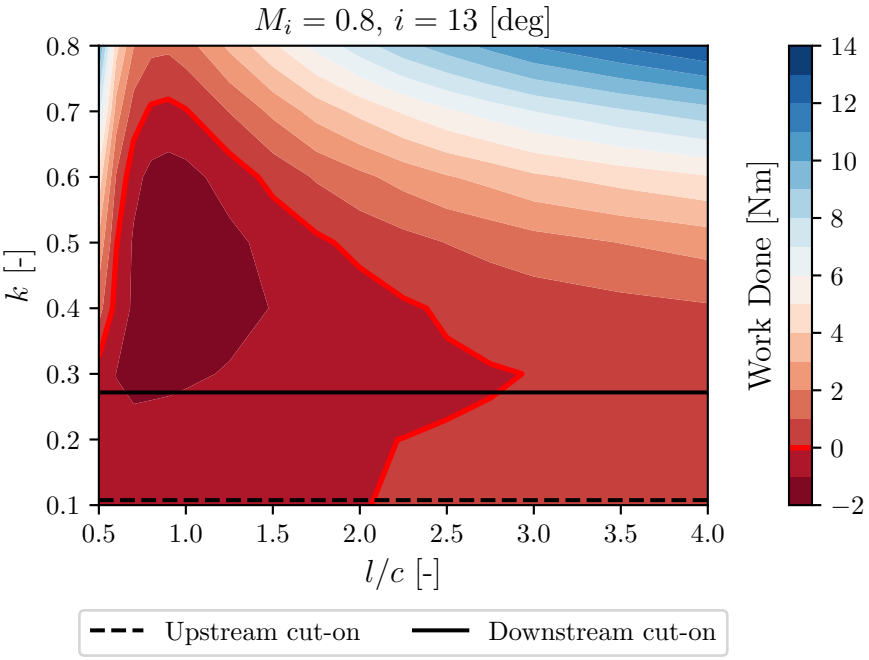


Figure 8.9: Stability map for the transonic test case

To investigate this trend in reduced frequency, the blade unsteady pressure coefficient amplitude a), unsteady pressure coefficient phase b) and local work done per cycle c) are plotted for many reduced frequencies with $l/c = 2.5$ as shown in figure 8.10. Here, the leading edge is at $x/c = 0$, the pressure side is from $-1 < x/c < 0$ and the suction side is from $0 < x/c < 1$.

It can be seen from figure 8.10 a) that the amplitudes of unsteady pressure on the pressure side remain very similar for all reduced frequencies. On the suction side, the largest amplitudes of unsteady pressure occur in the region of the shock at $x/c = 0.25$. The location of maximum unsteady pressure occurs at the shock front, where movement of the shock wave results in large changes in unsteady pressure. It can be seen that increasing the reduced frequency increases the unsteady pressure amplitude on the shock front. However, the location of maximum unsteady pressure along the chord does not seem to change much as a function of reduced frequency, as the Mach number and incidence are fixed, which sets the structure of the shock. This also explains the similar unsteady pressure amplitudes near the leading edge, as the constant incidence means the location of the steady-state stagnation point does not change. Any changes to the local unsteady stagnation point are expected to be fairly similar as a function of reduced frequency. Increasing the reduced frequency increases the unsteady pressure amplitude

both before and after the shock. The unsteady pressure amplitude towards the trailing edge of the suction side $0.8 < l/c < 1$ remains similar for all reduced frequencies.

It was shown in chapter 5 that the phase of unsteady pressure is key in determining whether positive or negative work is done on the blade. The red shaded regions in figure 8.10 b) show the phase of unsteady pressures that result in destabilising work done on the blade, where the darker shade indicates greater instability. For the pressure side, the unstable phases of unsteady pressure are $0° < \phi < 90°$ and $270° < \phi < 450°$ and for the suction side, $90° < \phi < 270°$. This shaded region accounts for the mode shape and blade normals for this specific case. On the pressure side, the phase is most unstable when $k = 0.2$, which is unstable for the entirety of the pressure side. Whereas the phase is stable for the entire pressure side when $k = 0.6$. On the suction side, the phase of unsteady pressure in the supersonic pre-shock region $0 < x/c < 0.25$ is stable for all reduced frequencies. In the region after the shock, the phase of unsteady pressure has moved into an unstable region for all reduced frequencies. This shows that the phase change associated with the shock wave is destabilising. Towards the trailing edge, there is a local region of stability that is associated with the trailing edge diffusion-driven separation. This is similar for all reduced frequencies, as the incidence is fixed, which sets the trailing edge flow.

It can be seen that there are some different trends in the phase of unsteady pressure on the suction side as the reduced frequency varies. Firstly, in the supersonic pre-shock region $0 < x/c < 0.25$, increasing the reduced frequency shifts the phase to a more stable value closer to $\phi = 0°$. However, generally, the phases of unsteady pressures are comparable. In the region of the shock front, the phase change associated with the shock is very sharp for $k = 0.2$ and $k = 0.3$ but becomes much less sharp as the reduced frequency increases. Downstream of the shock front, all reduced frequencies have an unstable phase, but the most unstable reduced frequency is $k = 0.4$, as the phase of unsteady pressure is closest to $\phi = 180°$. It can be seen that near the trailing edge, the stabilising change in phase associated with the separation occurs much closer upstream for low reduced frequencies. When $k = 0.2$, the downstream acoustic wave is cut off, and the downstream circumferential travelling wave propagates up through the passage and interacts with the shock. This explains the difference observed in the phase in the region $0.25 < x/c < 0.35$ just downstream of the shock front for $k = 0.2$. In this region, for $k = 0.2$, the gradient of the phase is negative, which indicates that there is a perturbation in pressure travelling upstream towards the shock front. This results in the very sharp change in phase observed for $k = 0.2$. As the downstream acoustic wave cuts on, the perturbations in pressure no longer

propagate up the passage, which results in a much smoother variation in phase near the shock for $k = 0.6$. To better understand the changes in phase occurring on the suction side, the instantaneous unsteady pressure p' is plotted at different points in the cycle for $k = 0.2$ and $k = 0.3$ in figure 8.11. This shows that the phase of unsteady pressure is very similar in the region near the leading and trailing edges on the suction side, and the largest change in phase is associated with the shock. It can be seen that for $k = 0.3$, there is a delay in the shock behind that of $k = 0.2$.

The amplitude and phase can now be related back to the total work done per cycle in figure 8.10 c). It can be seen that on the pressure side, the amplitude of the work done per cycle is significantly smaller than on the suction side for a given reduced frequency. This is due to the small amplitude of unsteady pressure on the pressure side compared to the suction side. This shows that the trends in the total work done per cycle as a function of reduced frequency are dominated by the work done on the suction side. On the suction side, in the region of the shock, there is a large spike in work done per cycle for all reduced frequencies. This spike is associated with the large unsteady pressure in this region due to the movement of the shock. It can be seen for $k = 0.2$, that this spike is stabilising as the phase of unsteady pressure is in a stable region. For $k = 0.3$, the downstream acoustic wave has just cut on, which results in a phase change of the shock, which moves the phase into an unstable region; therefore, the spike in work done per cycle becomes destabilising. This is also true for $k = 0.4$. When $k = 0.6$, the interaction of the pressure wave and the shock is weaker, resulting in a stabilising spike in work done. It was shown in figure 8.10 that the least stable reduced frequencies are those just above the downstream cut on reduced frequency. It is concluded that, when the downstream acoustic wave cuts on, the downstream circumferential travelling wave no longer propagates as effectively up the passage and has a weaker interaction with the shock. This causes a phase change of the shock, which creates a large amount of destabilising work done per cycle for these reduced frequencies.

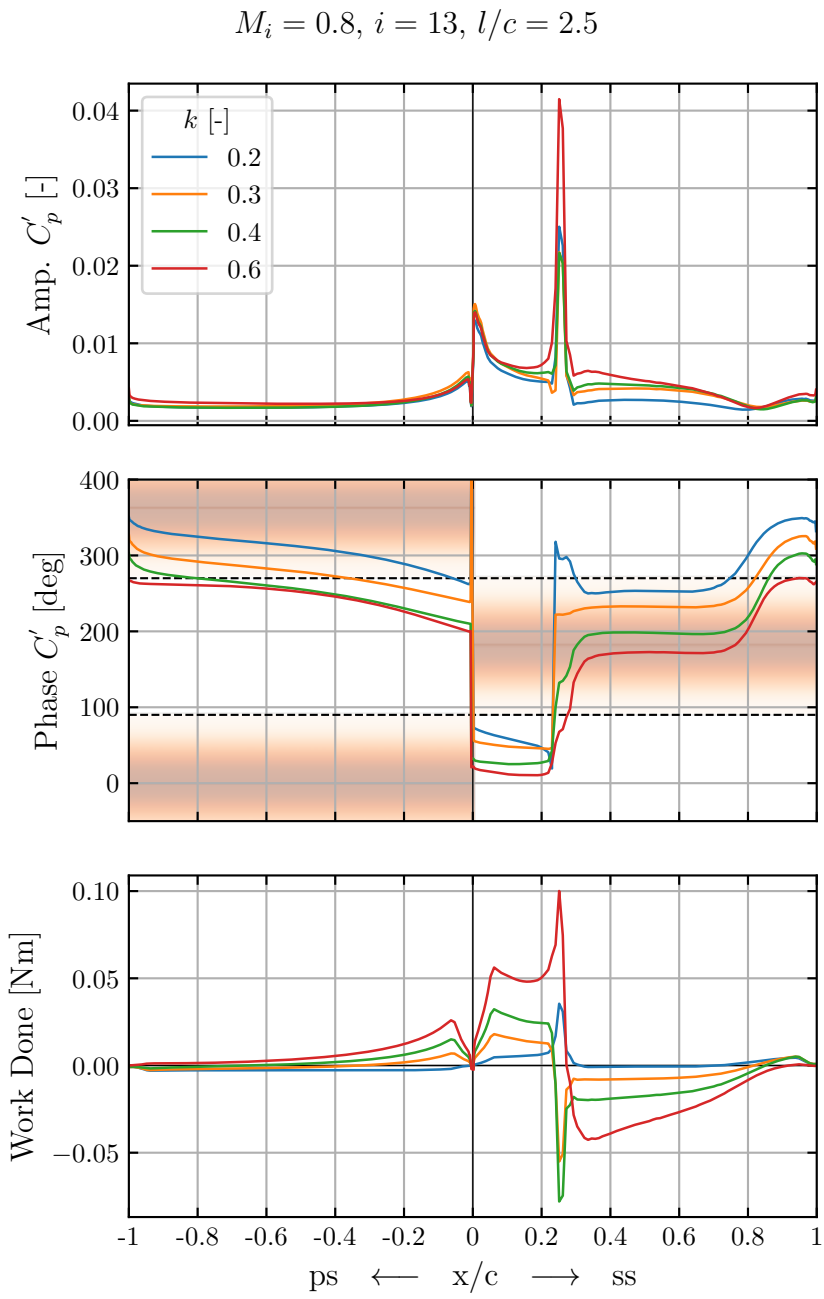


Figure 8.10: Effect of reduced frequency on the a) amplitude of unsteady pressure coefficient, b) phase of unsteady pressure coefficient, and c) local work done per cycle for the transonic test case

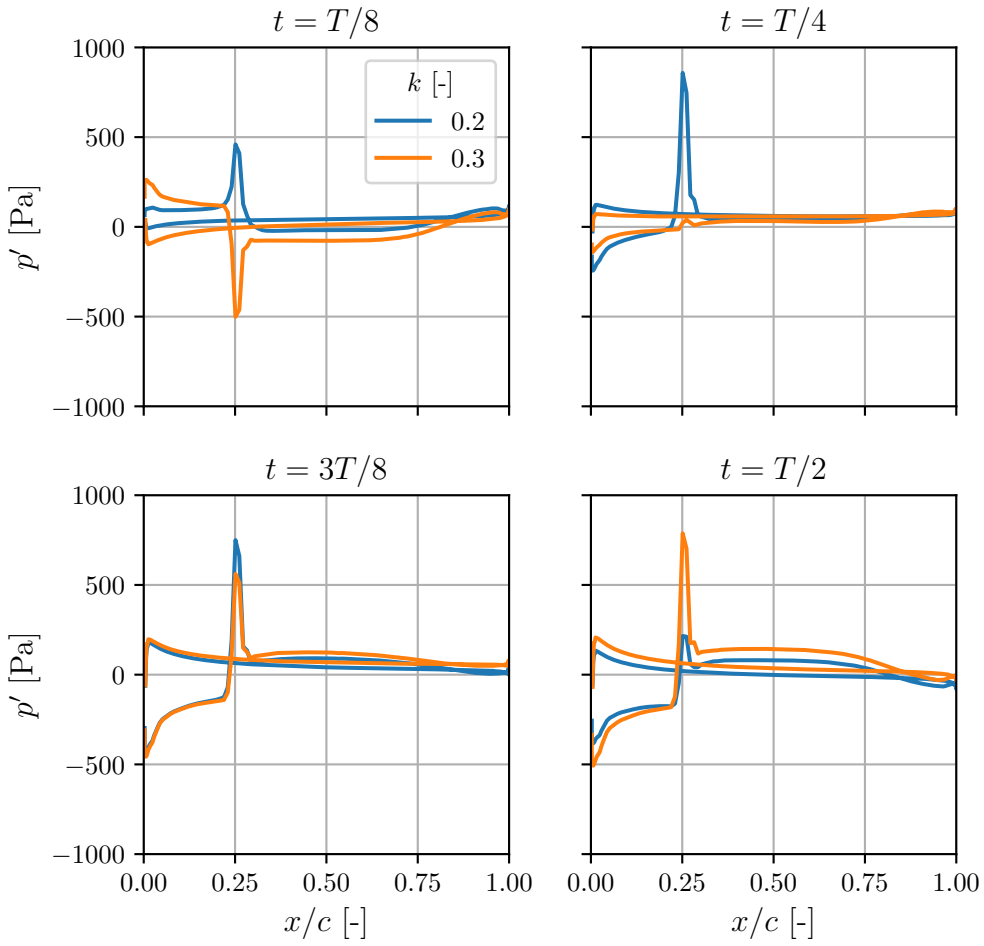


Figure 8.11: Blade surface instantaneous unsteady pressure for $k = 0.2$ and $k = 0.3$

It can be seen in figure 8.9 that for $k = 0.5$, there is a stabilising of the blade as l/c moves towards a pure twist mode shape. A similar trend was observed in chapter 6 which showed a minimum aerodamping occurred at an l/c slightly above pure twist. To examine this trend further, the aerodamping components defined in chapter 5 are plotted as a function of l/c for $k = 0.5$ in figure 8.12. It can be seen that the aerodamping components correctly sum to reproduce the aerodamping for the combined 1F mode shape, validating the method. The aerodamping due to plunge motion induced unsteady lift (PL) is positive and stabilising for all examined l/c. The aerodamping is zero at $l/c = 0.5$ as the plunge vibration and induced forcing is zero. As

l/c is increased, the aerodamping quickly tends towards a constant positive value, which remains practically unchanged in the range of $2 < l/c < 4$. It is assumed that as $l/c \to \infty$, the PL aerodamping tends towards some constant positive value. The PL term is a matching aerodamping component, meaning it only requires the unsteady pressures and mode shape from a single simulation. Therefore, examining the PL aerodamping with increasing l/c is equivalent to examining the aerodamping for a plunge mode shape with increasing vibration amplitude. The conclusion that the PL aerodamping always has a constant positive value is therefore equivalent to saying a blade vibrating in a pure plunge mode shape will always be damped by its own vibration. The aerodamping due to twist motion induced unsteady lift (TL) dominates the observed trends for the total aerodamping. Firstly, the TL term has the largest magnitude of all components and is the only component that has negative aerodamping for this reduced frequency and operating point. Therefore, for any point where the aerodamping is negative and flutter occurs, the TL aerodamping term is responsible. While the aerodamping is zero when $l/c = 0.5$, the aerodamping quickly drops to a large negative value, which hits a maximum negative value at $l/c = 0.8$, where the twist axis is just inboard of the blade trailing edge. In the range $0.8 < l/c < 4$ the aerodamping slowly increases, but still remains negative over the computed range. As $l/c \to \infty$ it is known that the TL aerodamping will converge to zero as the induced unsteady pressure due to twist tends to zero. The aerodamping due to plunge motion induced unsteady moment (PM) is small and stable for all l/c. The peak value of the PM term occurs at approximately the same l/c as the peak value of the TL term, which is interesting as these are the only cross-term aerodamping components. The PM aerodamping tends to zero as $l/c \to \infty$ as the induced moment tends to zero. The aerodamping due to twist motion induced unsteady moment (TM) is very small when $l/c > 2$ due to the small twist amplitude and unsteady moment for these plunge dominated modes. The TM aerodamping is the only non-zero aerodamping component when $l/c = 0.5$. In conclusion, this result has shown that it is the TM aerodamping term responsible for the stabilising of the blade at low l/c, but it is the TL aerodamping term that is responsible for the large destabilising response in the range of $0.6 < l/c < 1.8$.

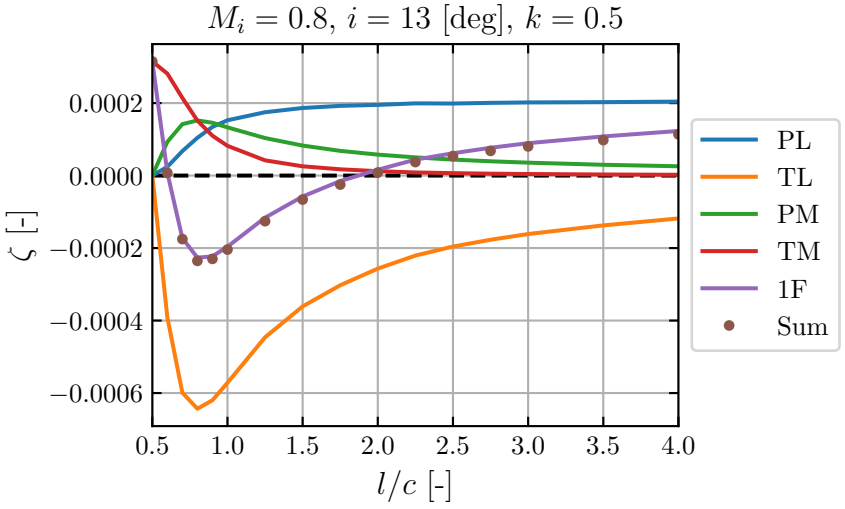


Figure 8.12: Aerodamping components as a function of l/c for $k = 0.5$

8.5 Effect of Varying Incidence

For investigating the effect of varying incidence, the inlet Mach number is fixed to the transonic case where $M_i = 0.8$, as this is the most representative case for flow in a typical aero engine compressor. Additionally, the inter-blade phase angle is fixed to $\sigma_m = 20°$, as this is generally the most unstable across the input parameter space. Figure 8.13 shows a constant Mach number characteristic for $M_i = 0.8$. To build this characteristic, the inlet Mach number and total pressure are fixed at the inlet, and the incidence is varied to move up and down the characteristic. Low incidences correspond to a rotor that is operating near choke, and high incidences correspond to a near stall condition. For the varying incidence cases, four main operating points are selected, as highlighted in figure 8.13. The maximum static-static isentropic efficiency η is also shown where

$$\eta = \frac{(p_2/p_1)^{\frac{\gamma-1}{\gamma}} - 1}{(T_2/T_1) - 1} \tag{8.8}$$

The limits are operating point 1, which is just below peak isentropic efficiency with an incidence of $i = 7°$, and final point 4, just below stall with an incidence of $i = 14.75°$. It can be seen that point 4 is the only point that is located on a positive slope of characteristic, while point 3 is operating at a similar pressure ratio but with a higher mass flow.

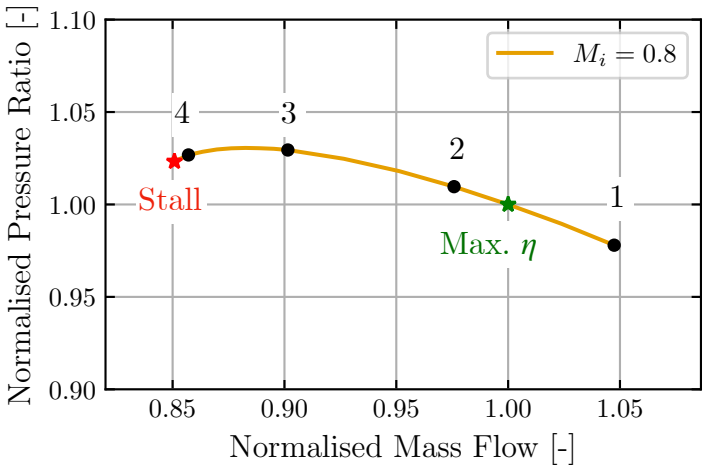


Figure 8.13: Selected operating points along the compressor characteristic for $M_i = 0.8$

Figure 8.14 shows the blade surface isentropic Mach number as a function of the normalised chord for different flow incidences. For an inlet Mach number of $M_i = 0.8$, the flow across the blade is transonic, and there is a shock wave on the suction side. As the incidence on the blade increases, the shock wave increases in strength and moves closer to the leading edge. This is a similar trend to that observed when a transonic compressor is throttled at constant rotational speed [79]. Towards the trailing edge, $0.8 < x/c < 1$ at large incidences, the trailing edge flow separates, which causes an increase in the isentropic Mach number. This is a results of decreased static pressure in the separated region. For $i = 7°$, there is a crossover of the suction and pressure surfaces at the leading edge. This results in a drop in efficiency, which places this incidence on the choke side of the design point.

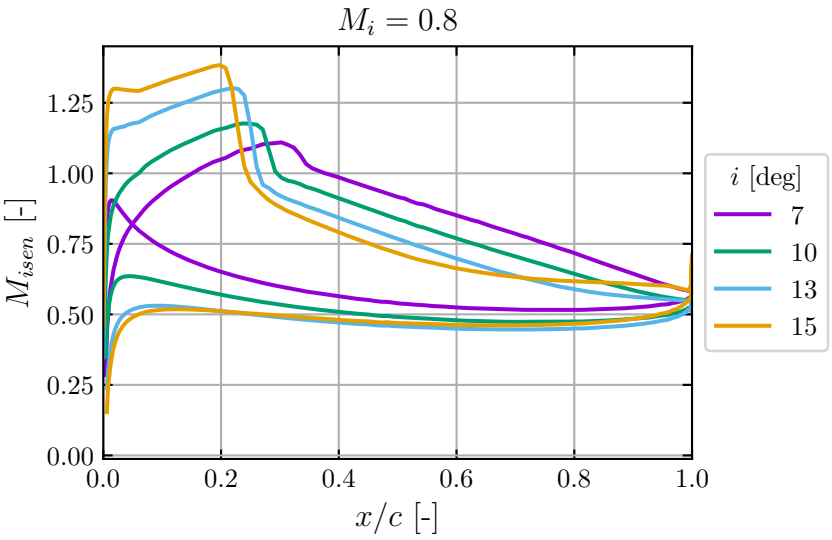


Figure 8.14: Blade surface isentropic Mach number

Figure 8.15 and figure 8.16 show the mid-span Mach number contour for the rotor operating near choke and near stall, respectively. Here, 'near choke' has an incidence $i = 7°$ and 'near stall' has an incidence $i = 14.75°$, which is the highest incidence CFD solution before the rotor can no longer satisfy the prescribed pressure ratio. The iso-line of $M = 1$ is highlighted in black in the region of the shock. For the near choke incidence, there is very little separation of the flow at the trailing edge. However, the zoomed-in region near the leading edge shows that there is a separation beginning to form on the pressure side due to the below design incidence. It has been shown in the literature that the flow on the leading edge fully separates for $M_i = 0.75$ and $i = 5°$ for this geometry [80]. Near stall, the flow is very different. There are two regions on the suction side that separate for different reasons. Firstly, there is a shock-induced flow separation, which can be seen from the zoomed-in figure, and a large trailing edge diffusion-driven separation. The flow remains detached along the entirety of the suction side. For the near stall case, the shock has moved significantly closer to the leading edge, and the sonic region has grown and covers a much larger area of the passage. In both cases, the cascade is considered unstarted as the shock is not contained within the passage.

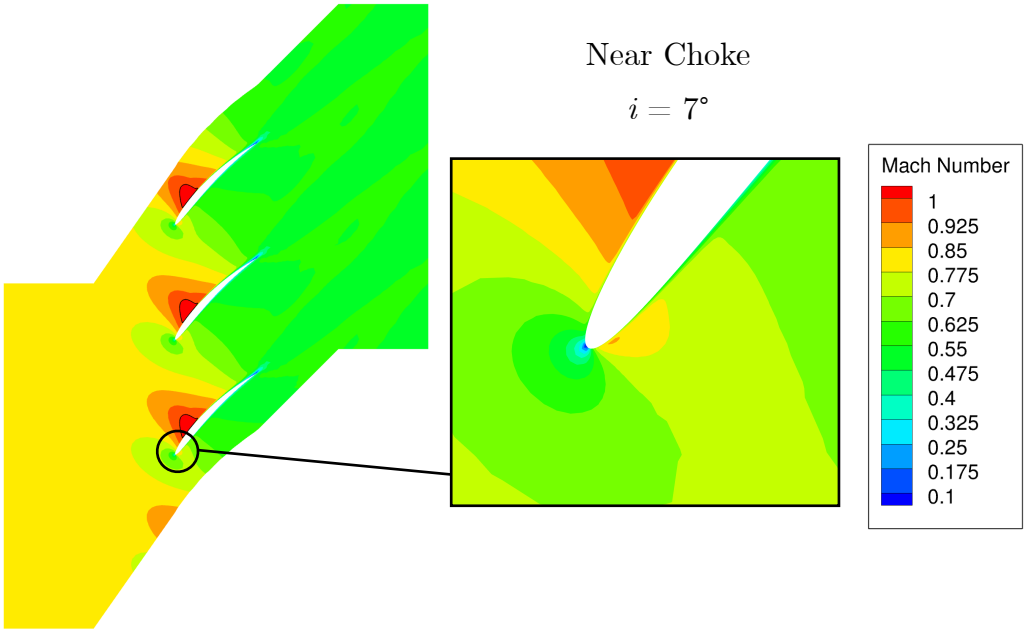


Figure 8.15: Mid-span Mach number contour near choke

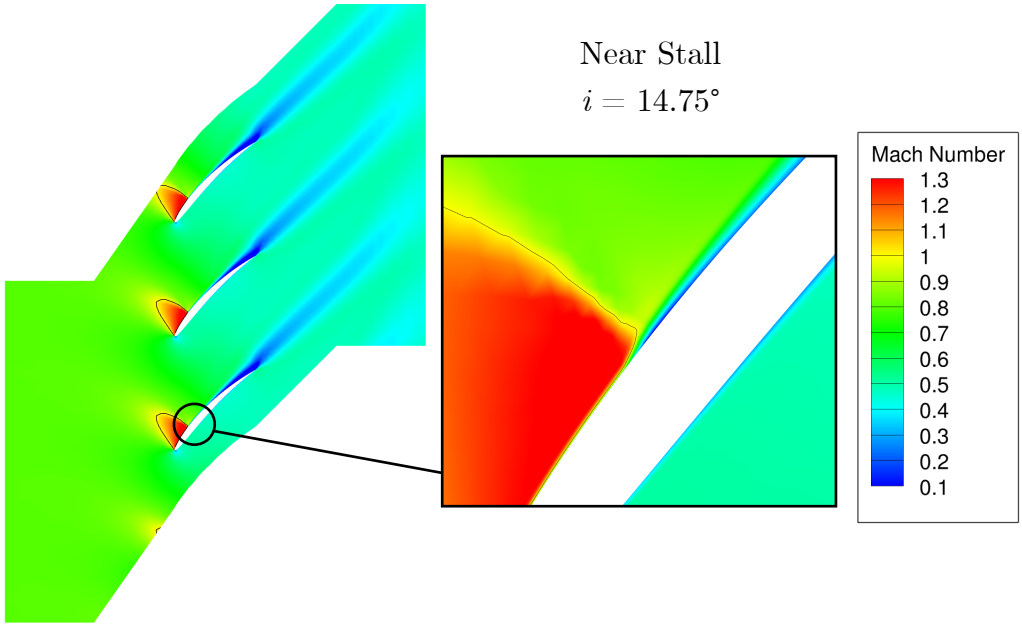


Figure 8.16: Mid-span Mach number contour near stall

Figure 8.17 shows how the aerodamping components vary as a function of

the incidence on the rotor for $k = 0.3$ and $l/c = 2$. Firstly, it can be seen that increasing the incidence on the rotor causes total aerodamping to decrease. For this particular k and l/c, the cascade begins to flutter when the incidence is increased beyond $i = 12.3°$. The gradient of aerodamping with respect to incidence is low at the design point but begins to drop off significantly faster towards stall, which highlights the high sensitivity of the aerodamping to the operating point near stall. It can be seen that the slope of the aerodamping is smooth; there are no drastic changes in the aerodamping as the incidence is increased up to and beyond the point of zero slope of characteristic. Even when there are large-scale separations on the suction side near stall, the aerodamping decreases smoothly. This is in agreement with the literature for transonic fans [6]. Figure 8.17 also shows how the components of the aerodamping change with incidence. It can be seen that as the incidence increases, all of the aerodamping components decrease, indicating that the change in steady loading is destabilising for all interactions of vibration and forcing. The work done due to plunge vibration induced unsteady lift and moment (PL and PM) contribute positively to flutter stability for the entire incidence range. The work done due to twist vibration induced unsteady moment (TM) switches from positive to negative damping at approximately $i = 12.2°$ but remains small for all incidences. Finally, the work done due to twist vibration induced unsteady lift (TL). This term is the most important for a few reasons. Firstly, the TL term dominates the trends seen in total aerodamping. TL varies very little up to $i = 10°$ and drops sharply past this point, while all other components decrease almost linearly with incidence. Secondly, close to the stall boundary, where stall flutter is likely to occur, the PL, TM, and PM terms cancel, and the total aerodamping is almost completely determined by the TL component.

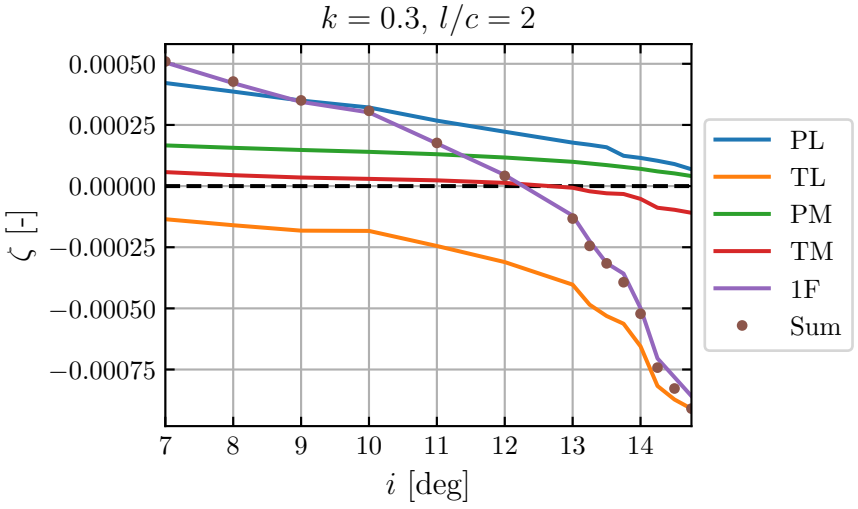


Figure 8.17: Aerodamping components as a function of incidence

Figure 8.18 shows the cut-on reduced frequencies upstream and downstream of the rotor as a function of incidence. It can be seen from the figure that the cut-on conditions do not vary much as the incidence on the rotor is varied. It was shown in chapter 5 that the cut-on frequency can be determined by

$$\omega_{cut} = aM_\theta \frac{m}{r} + a\sqrt{k_{r\theta}^2 \left(1 - {M_x}^2\right)} \tag{8.9}$$

For this particular case, the radial-circumferential wavenumber $k_{r\theta}$, nodal diameter m (inter-blade phase angle), speed of sound a and Mach number magnitude M are constant. The only changes made to the cut-on frequency with respect to incidence are due to changes in the upstream and downstream axial and tangential Mach numbers M_x and M_θ. Where the upstream Mach numbers vary due to the change in inlet flow angle and the downstream Mach numbers vary due to the flow turning imparted by the rotor. It is therefore concluded that the change in the upstream and downstream axial and circumferential Mach numbers in the incidence range of interest is not considerable enough to induce large changes in the cut-on reduced frequency. It was shown in figure 8.17 that the aerodamping decreases as incidence increases for a fixed reduced frequency and plunge-twist ratio. It can therefore be concluded that the decrease in aerodamping with increased incidence is unlikely to be associated with a change in the upstream and downstream acoustic wave properties.

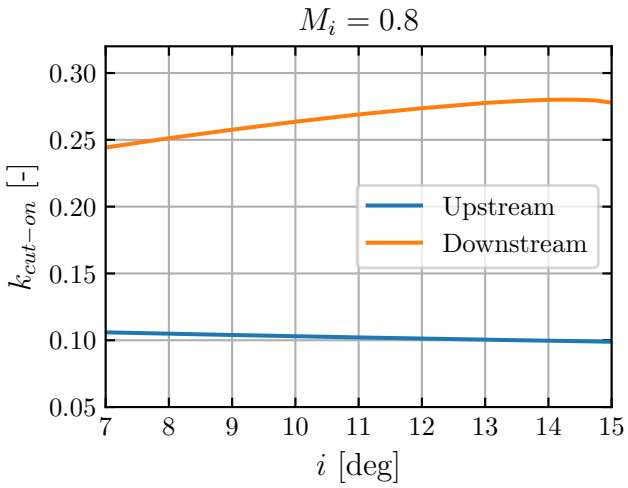


Figure 8.18: Upstream and downstream cut on reduced frequency as a function of incidence

Figure 8.19 shows a) the amplitude of unsteady pressure coefficient, b) phase of unsteady pressure coefficient and c) resulting aerodamping ratio as a function of normalised chord for different incidences for a single mid-span radial layer. This figure gives an incite into how the local unsteady pressure and mode shape interact to produce the resultant integrated aerodamping in figure 8.17.

It can be seen in figure 8.19 a) that there are large amplitudes of unsteady pressure on the suction side, particularly in the region of the shock. The peak location of maximum unsteady pressure occurs directly on the shock wave front, where the movement of the shock itself induces large changes in the unsteady pressure. It was shown in figure 8.14 that increasing the incidence results in a stronger steady state shock closer to the leading edge. This is reflected in the amplitude of unsteady pressure, which shows larger amplitudes as incidence increases, as well as the location of the maximum unsteady pressure moving closer to the leading edge. There are also large unsteady pressure amplitudes on the leading edge of the pressure side for low incidences, which decrease in amplitude as the incidence is increased. This is due to the low incidence being close enough to choke that there is a region of the blade on the pressure side that is close to separating. This can be seen from figure 8.14, which shows a crossover of the suction side pressure side towards the leading edge, indicating that the stagnation point is on the suction side of the blade. As the blade vibrates, there is a local separation on the pressure side, which induces a large unsteady pressure amplitude. As

the incidence increases, the stagnation point moves from the suction side to the pressure side, and the unsteady pressure amplitude near the leading edge on the pressure side decreases. The unsteady pressures on the rest of the pressure side remain largely unchanged. It can also be seen that towards the trailing edge of the suction side $0.8 < x/c < 1$, there is an increase in the amplitude of unsteady pressure with incidence, which corresponds to large-scale separations on the suction side in this region.

Figure 8.19 b) shows the phase of the unsteady pressure coefficient. The highlighted regions show the phase of unsteady pressure that results in destabilising work being done on the blade, where a darker shade indicates greater instability. It can be seen that on the suction side, the supersonic pre-shock region has a phase of unsteady pressure, which is in the stable region. The shock then causes a large change in the phase of unsteady pressure, which terminates in a phase inside the unstable region. Therefore, the phase change associated with the shock is destabilising. On the suction side, the phase of unsteady pressure does not change much with incidence in the range $0 < x/c < 0.6$. However, in the trailing edge region of the suction side $0.6 < x/c < 1$ there is a large phase change associated with the trailing edge separation, which moves the phase angle out of the unstable region. Larger incidences give rise to larger trailing edge flow separations, which cause the phase to shift from unstable to stable much further up the chord. The phase of unsteady pressure on the pressure side has a very similar trend with normalised chord for all incidences. However, there appears to be an approximately linear offset in phase as the incidence is increased, which moves the pressure side phase into an unstable region. It is hypothesised that this change in phase is associated with a decrease in axial flow velocity in the passage as incidence increases, which affects the speed of propagation of perturbations in the passage and produces a phase lag.

Figure 8.19 c) shows the resulting local aerodamping. This shows that the supersonic pre-shock region is stabilising and that the aerodamping after the shock front is negative and destabilising. This confirms the work of Rendu et al. [44] and Vahdati et al. [45]. Before the shock front, the aerodamping remains fairly constant for all incidences. The behaviour directly on the shock produces a large spike in unstable aerodamping, which is more unstable and occurs closer to the leading edge for large incidences. This can be directly related to the higher unsteady pressure amplitude and the closer proximity of the shock to the leading edge for high incidences. In the region after the shock, the aerodamping is again very similar for all incidences.

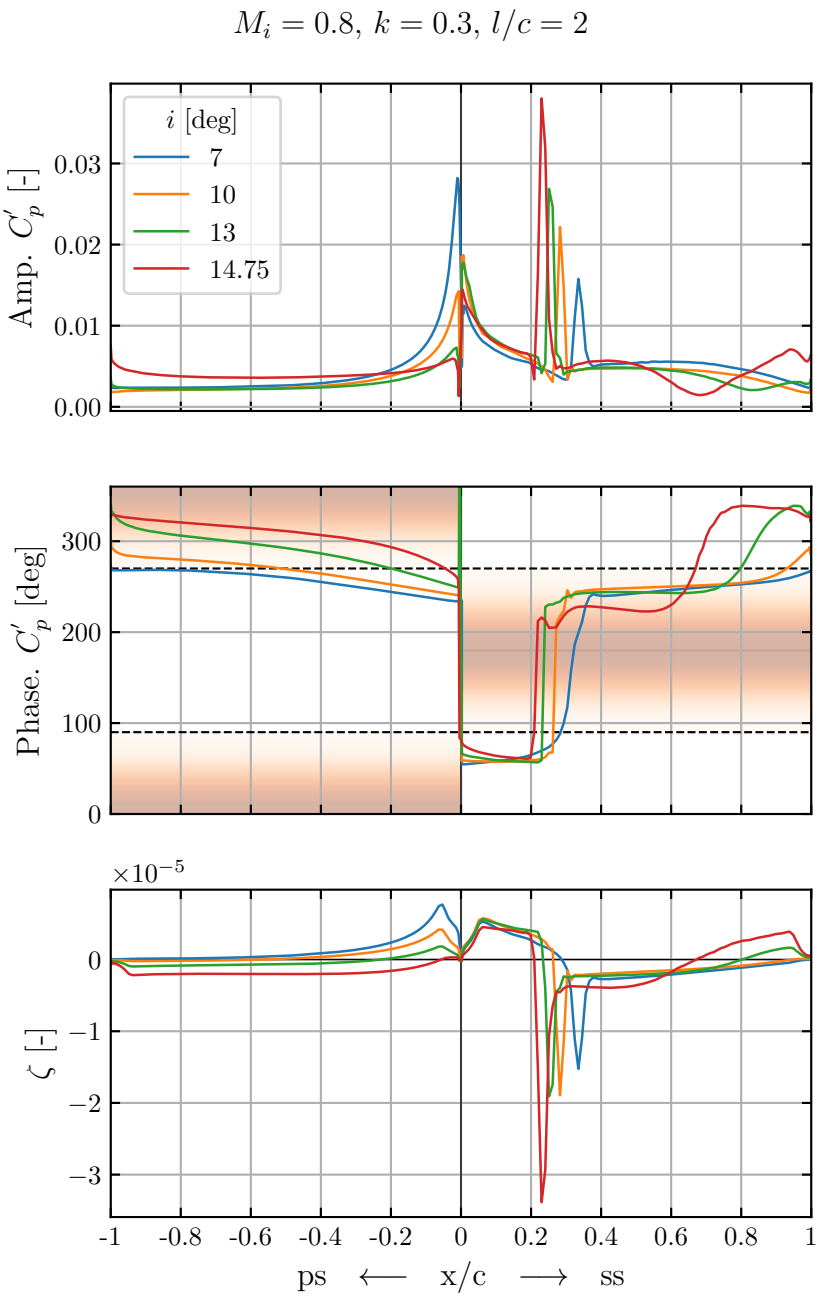


Figure 8.19: Effect of incidence on the a) amplitude of unsteady pressure coefficient, b) phase of unsteady pressure coefficient, and c) total aerodamping

These results show that the separated region on the suction side near the trailing edge produces a large stabilising aerodamping, which is a surprising

finding as flow separation is typically associated with being detrimental to flutter stability. The aerodamping on the leading edge of the pressure side is highly stable for low incidences, which can be accounted for by the large unsteady pressure amplitude and stable phase in this region. However, as the incidence increases, the pressure side becomes unstable for nearly the entire side due to the linear offset observed in the phase of unsteady pressure.

Figure 8.20 shows the contribution to the total aerodamping for the suction side (SS) and the pressure side (PS) as a function of incidence for $k = 0.3$ and $l/c = 2$. This shows that the total aerodamping as a function of incidence is dominated by the changes in aerodamping on the pressure side. It was shown in figure 8.19 that the pressure side aerodamping is driven by two factors: near choke leading edge separation at low incidences and an approximately linear change in phase as incidence is increased due to a change in axial flow velocity in the passage. It can be seen that the variation in aerodamping as a function of incidence for the suction side is small. By referring back to the local aerodamping for a single mid-span radial layer in figure 8.19c), it can be seen that the aerodamping in the region of the shock front becomes more unstable as incidence is increased. However, the separated region near the trailing edge on the suction side becomes more stable as the incidence increases. These stabilising and destabilising changes to the aerodamping with incidence mostly cancel, which results in very small changes to the aerodamping on the suction side as a function of incidence.

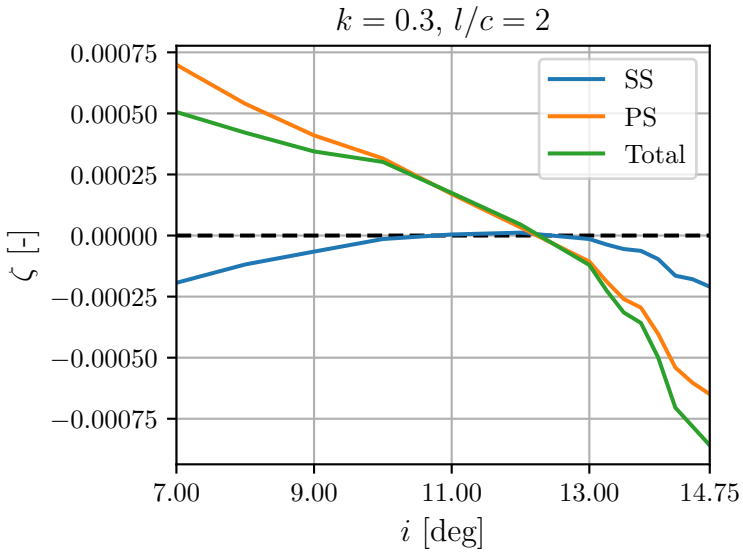


Figure 8.20: Suction side (SS) and pressure side (PS) contributions to the total aerodamping as a function of incidence – $k = 0.3$, $l/c = 2$

For each flow incidence, a full stability map is defined as a function of reduced frequency k and twist axis setback l/c. The reduced frequency range is defined as $0.1 < k < 1$ and the normalised twist axis setback range as $0.5 < l/c < 4$. The values selected between these limits were chosen in constant 5% increments. The aerodamping for each incidence and mode shape is found, and the flutter stability limit is determined by locating the iso-line where $\zeta = 0$. Figure 8.21 shows the regions on the stability map where flutter occurs for different incidences as a function of k and l/c. The lines of upstream and downstream cut on reduced frequency $k_{cut,up}$ and $k_{cut,down}$ are also shown. It is assumed that the cut-on frequencies are approximately constant for each incidence, which is a reasonable assumption given the results shown in figure 8.18. The black lines mark the critical flutter reduced frequency, where $\zeta = 0$. It can be seen that for the $i = 10°$ case, flutter occurs in a very small region, which is largely outside the typical k and l/c expected for a compressor blade mode shape. Therefore, the risk of flutter occurring at this incidence is very low. Whereas for $i = 14.75°$, the unstable region has grown significantly, and flutter is much more likely to occur due to the likelihood of a typical compressor mode shape lying in an unstable region. It can be seen that for $i = 12°$ and $i = 13°$, reduced frequencies with the largest number of unstable l/c occur when the downstream acoustic wave is just cut on. It was shown in the transonic test case analysis that this is due to the destabilising phase change of the shock as the flow in the passage changes when the downstream acoustic wave cuts on.

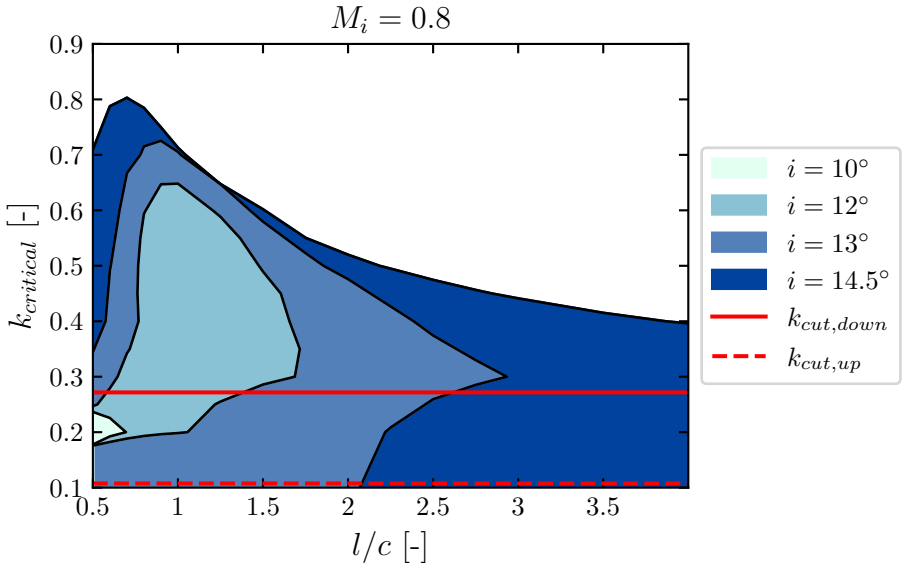


Figure 8.21: Flutter regions for different flow incidences as a function of k and l/c

Figure 8.22 shows the flutter stability limit for three different cases. Case A is for standard configuration 10 with $M_i = 0.8$ and $i = 10°$; case B is for the subsonic linear cascade from chapter 6; and case C is for standard configuration 10 with $M_i = 0.8$ and $i = 13°$. The lift coefficients for these cases are 0.2409, 0.1132 and 0.2627 for cases A, B, and C respectively. It can be seen that case A is considerably more stable than case B despite the fact that case B has a significantly higher steady aerodynamic loading, nearly a factor of 2 change in the lift coefficient. In addition, it can be seen that case C is considerably more unstable than case B for the linear cascade, despite case C only having a 3° change in incidence compared to case A and only an approximately 9% change in steady lift coefficient. This shows that increasing the steady aerodynamic loading does not necessarily make the blades more unstable. But rather, the increase in steady aerodynamic loading when a rotor is operating near the working line is stabilising, and it is only when the flow changes near the stall line, due to a high incidence, that the higher steady loading is destabilising. These flow changes are the increase in shock strength, movement of the shock towards the leading edge, flow separation, phase of the shock, and changes in the propagation of pressure perturbations due to decreased axial flow velocity in the passage. In conclusion, it is not an increase in steady loading that is destabilising, but rather specific flow features near stall that are destabilising. Also shown in this figure are the closest

approximations of the plunge-twist incidence ratio. It can be seen for case B for the linear cascade that the flutter stability limit can be well approximated by a constant plunge-twist incidence ratio. However, for cases A and C, the agreement between the plunge-twist incidence ratio and the flutter stability limit is poor. This suggests that the definition of the plunge-twist incidence ratio is effective for simple, subsonic cases only, and the addition of complex flow features such as shock waves and separations breaks the assumptions made in the definition of the model.

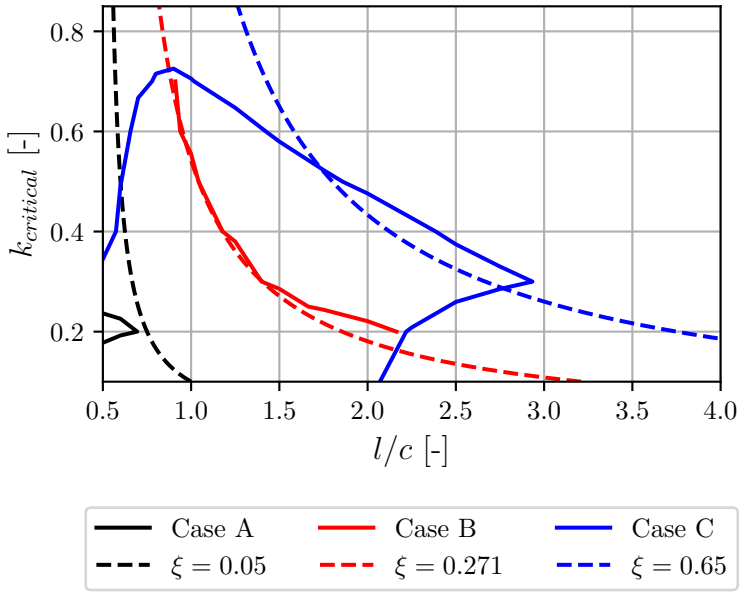


Figure 8.22: Comparison of the flutter stability limit between the subsonic linear cascade and standard configuration 10

8.6 Effect of Varying Inlet Mach Number

For investigations on the effect of varying inlet Mach numbers, the flow incidence is kept constant. It was shown in the previous section that flutter only occurs when the blade incidence is sufficiently high. Therefore, for the Mach number variations, the flow incidence is fixed to $i = 14°$. Additionally, the inter-blade phase angle is fixed to $\sigma_m = 20°$, as this is generally the most unstable across the input parameter space.

Figure 8.23 shows the blade surface isentropic Mach number as a function of the normalised chord for different inlet Mach numbers. As to be expected, there is a clear change in the shock structure as the inlet Mach number is varied. For $M_i = 0.8$ and $M_i = 0.75$, the isentropic Mach number increases

from the leading edge towards the shock front, which terminates with a strong shock wave. Whereas for $M_i = 0.7$ the isentropic Mach number decreases from the leading edge to the shock front and is terminated by a much weaker shock. Below this inlet Mach number, the flow is entirely subsonic over the blades. The loading towards the trailing edge, $0.8 < x/c < 1$ increases as Mach number increases but maintains a very similar shape, which suggests that the flow near the trailing edge is largely set by the fixed incidence.

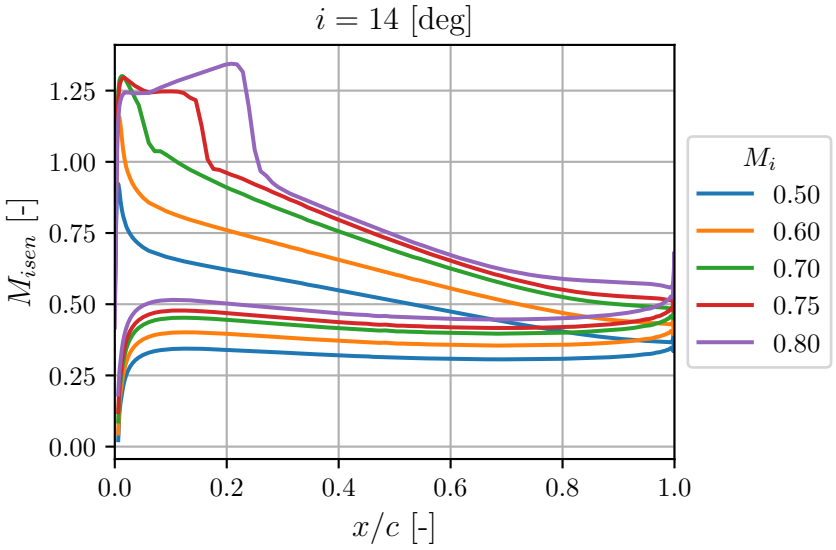


Figure 8.23: Blade surface isentropic Mach number for different inlet Mach numbers at fixed incidence

Figure 8.24 shows the total aerodamping as a function of the inlet Mach number for $k = 0.5$ and $l/c = 0.9$. This reduced frequency and plunge-twist ratio were selected as they are the most unstable mode shapes for each Mach number. It can be seen from the figure that, generally, increasing the Mach number makes the rotor more unstable. The most unstable case is $M_i = 0.8$, which indicates that the presence of a strong shock wave on the suction side is heavily destabilising. However, there is not a monotonic trend in aerodamping with Mach number, as there is a local stabilisation for $M_i = 0.7$.

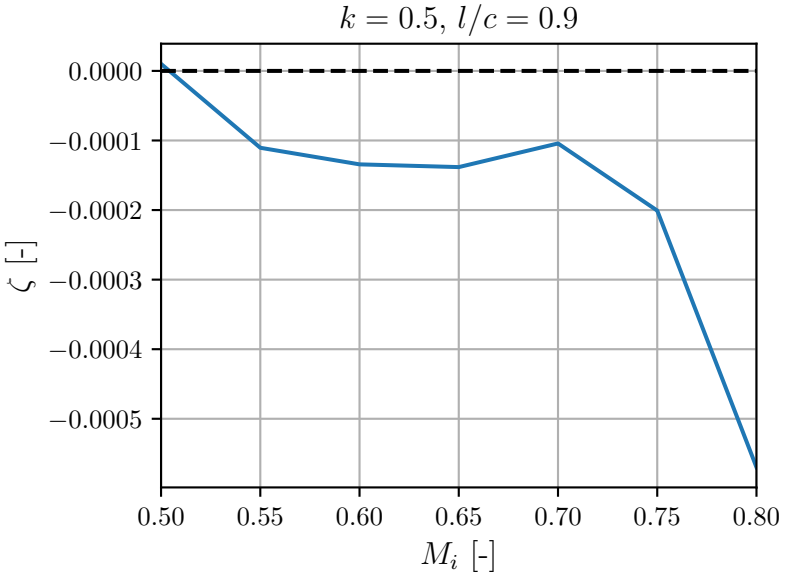


Figure 8.24: Effect of Mach number on aerodamping – $k = 0.5$, $l/c = 0.9$

Figure 8.25 shows a) the amplitude of unsteady pressure coefficient, b) phase of unsteady pressure coefficient and c) resulting aerodamping ratio as a function of x/c for different inlet Mach numbers for a single mid-span radial layer. Again, $k = 0.5$ and $l/c = 0.9$, as these are the most unstable modes.

It can be seen in figure 8.25 a) that the amplitude of unsteady pressure on the pressure side is approximately constant as the inlet Mach number increases. For the suction side, there are large changes as the Mach number is increased. Firstly, it can be seen that the peak in amplitude of unsteady pressure associated with movement of the shock moves significantly closer to the leading edge as the Mach number is decreased. This can be related to the steady aerodynamics of the shock, which moves closer to the leading edge as the Mach number is increased. For $M_i = 0.6$, there is no shock on the suction side but rather a large amplitude of unsteady pressure directly on the leading edge. After the shock front, the amplitudes of unsteady pressure for $M_i = 0.6$ and $M_i = 0.7$ are very similar for the majority of the suction side from $0.15 < x/c < 1$. It isn't until $M_i = 0.8$ that there is a large change in the unsteady pressure amplitude on the suction side. Firstly, it can be seen that this inlet Mach number is the only case with a large region of supersonic flow prior to the shock. In the region after the shock, the amplitude of unsteady pressure is much larger than for $M_i = 0.6$ and $M_i = 0.7$.

Figure 8.25 b) shows the phase of the unsteady pressure coefficient. This shows that for the pressure side, there is very little phase change as the inlet

Mach number is increased. Surprisingly, the trends in the phase of unsteady pressure are also quite similar on the suction side. For all inlet Mach numbers, the leading edge phase is stable, which then quickly switches to an unstable phase just downstream of the leading edge. For the transonic cases $M_i = 0.7$ and $M_i = 0.8$, there is a sharp change in phase associated with the shock. There is a similar phase change on the suction side in the region of $x/c = 0.2$ for $M_i = 0.6$, despite the fact that there is no shock present on the suction side. In the region of $0.3 < x/c < 0.7$, the phase flattens out with an unstable phase. The least stable phase in this region is for $M_i = 0.8$, as this is very close to $\phi = 180°$. There is a similar stabilising change in phase for each Mach number towards the trailing edge. This phase change is associated with the trailing edge diffusion-driven separation, which is fairly similar for each Mach number as the incidence on the blade is constant.

Finally, the unsteady pressures can be related to the local aerodamping, as shown in figure 8.25 c). Firstly, this shows that the aerodamping on the pressure side is approximately constant as a function of the inlet Mach number. This is directly related to the similar unsteady pressure amplitude and phase as the Mach number is varied. Therefore, it can be concluded that the majority of the changes in the total aerodamping with varying inlet Mach numbers are due to the interaction of flow and mode shape on the suction side. On the suction side for $M_i = 0.6$, the leading edge is stable, which switches to unstable at approximately $x/c = 0.175$. The amplitude of the aerodamping is very low compared to $M_i = 0.7$ and $M_i = 0.8$ as there is no shock wave present on the suction side. For $M_i = 0.7$, there is a large stabilising spike in aerodamping due to the shock wave unsteady pressure amplitude spike having a stable phase of unsteady pressure. In the post-shock region, the aerodamping is very similar to $M_i = 0.6$, as there is little change in the amplitude and phase of unsteady pressure between the two cases in this region. This shows that the stabilisation of the $M_i = 0.7$ case in figure 8.24 is due to the stabilising effect of the shock. For $M_i = 0.8$, the supersonic pre-shock region is stabilising, and the shock wave shifts the aerodamping to a negative value in the region after the shock. For this case, the shock wave itself is unstable, which creates a large spike in negative aerodamping at approximately $x/c = 0.25$. The post-shock region for $M_i = 0.8$ has large destabilising aerodamping compared to the two other cases. This is due to the increased unsteady pressure amplitude in the post-shock region.

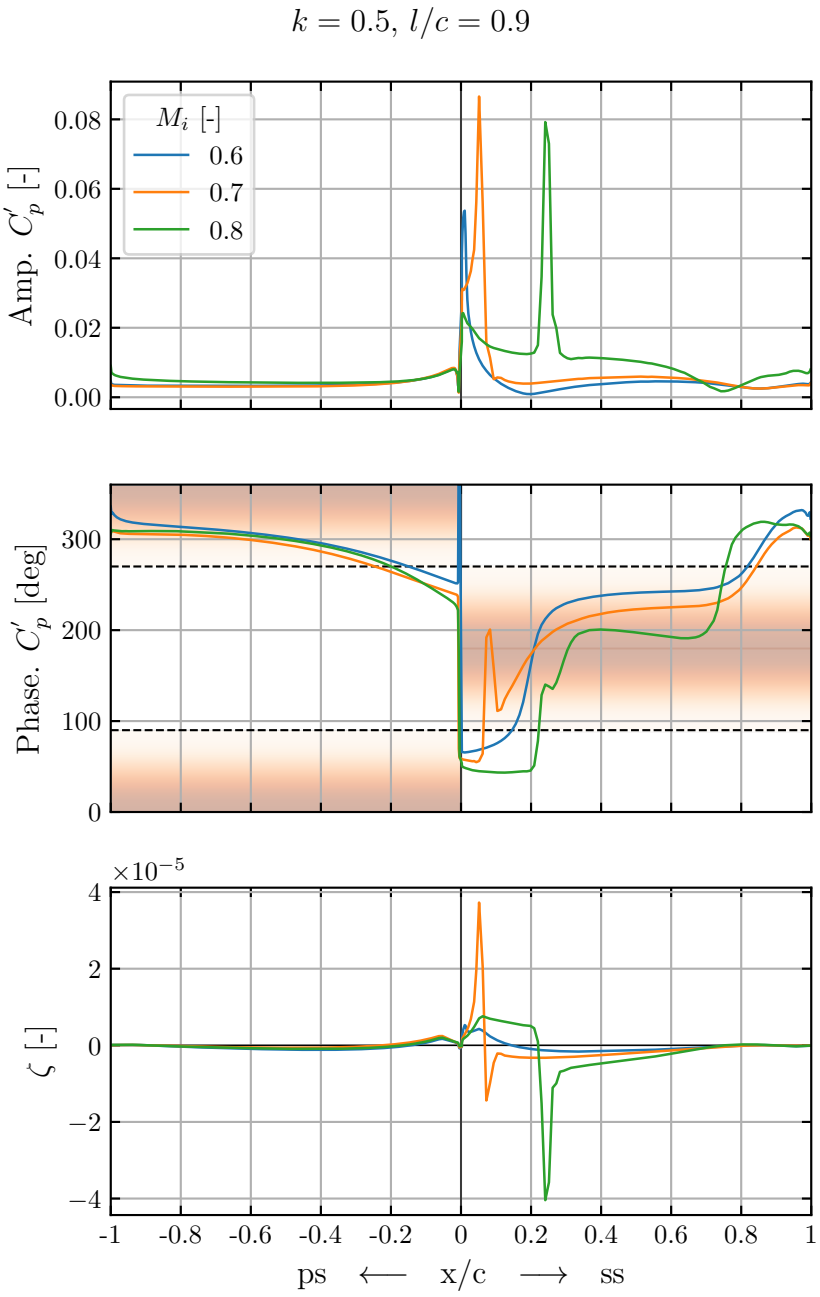


Figure 8.25: Effect of Mach number on the a) amplitude of unsteady pressure coefficient, b) phase of unsteady pressure coefficient, and c) total aerodamping – $k = 0.5$, $l/c = 0.9$

Figure 8.26 shows an aerodamping contour as a function of reduced fre-

quency and inlet Mach number. Also plotted on this figure are the upstream and downstream cut-on reduced frequencies. Here, the cut-on reduced frequencies for each inlet Mach number were calculated using the respective free stream flow velocity. It was shown in figure 8.18 that the variation of the axial and circumferential Mach numbers did not have a significant effect on the upstream and downstream cut-on reduced frequencies. Whereas in this case, it can be seen that there is a much larger variation. For example, when $M_i = 0.8$, the upstream acoustic wave cuts on at approximately $k = 0.1$, whereas when $M_i = 0.5$, the upstream acoustic wave cuts on at approximately $k = 0.4$. This shows that it is the magnitude of the Mach number rather than the distribution of the axial and circumferential components with constant magnitude that induces the largest changes in the cut-on frequency.

It was shown in figure 8.9 for the baseline transonic test case that the least stable mode shapes are those with a reduced frequency just higher than the downstream cut-on reduced frequency. Further analysis showed that there is a phase change associated with the shock, which occurs when the downstream acoustic wave cuts on which destabilises the blade. It can be seen from the current figure that this conclusion is true for all inlet Mach numbers, as there is a very close agreement between the cut on of the downstream acoustic wave and a sharp drop in the work done per cycle as the reduced frequency is increased. It can also be seen that there is a band of stability in the region where the upstream acoustic wave is cut on and the downstream acoustic wave is cut off. In the literature, this condition is associated with unstable work being done on the blade, but the opposite trend is observed in the current work. It is hypothesised that this change in trend is related to the phase of unsteady pressure on the suction side. It was shown in the analysis of the transonic test case that the total aerodamping is driven by the local aerodamping on the suction side as a function of reduced frequency. For a transonic compressor, it is highly unlikely that the downstream pre-cut on and downstream post-cut on phases of unsteady pressure are comparable to this two-dimensional case. For example, it was shown by Rendu [44] that two-dimensional analysis of a three-dimensional rotating compressor is not possible. This work stated that there is a radial flow migration that occurs on the suction side due to low axial velocity after the shock and large adverse pressure gradients due to the fan operating near stall. This causes the flow to be centrifuged radially, which is not possible in this case. The radial flow migration will induce a phase change downstream of the shock, which propagates significantly slower due to the small radial velocity compared to the axial or circumferential velocity. When the downstream acoustic wave is cut off, the downstream travelling pressure wave propagates up into the passage and interacts with this radial migration of the flow just before the

shock front. This interaction between the radial flow migration and the perturbation of pressure in the passage is suspected to be the root cause of the differing results. Not only this, but it was also shown by Huang [38] that the effect of the downstream wave cutting on and its effect on aerodamping can even be different for three-dimensional rotating compressors with different geometries and operating points. Therefore, it can be concluded that the cut on of the upstream and downstream acoustic waves significantly changes the state of the flow in the blade passage, which has a strong effect on the total aerodamping, and this is highly case-specific.

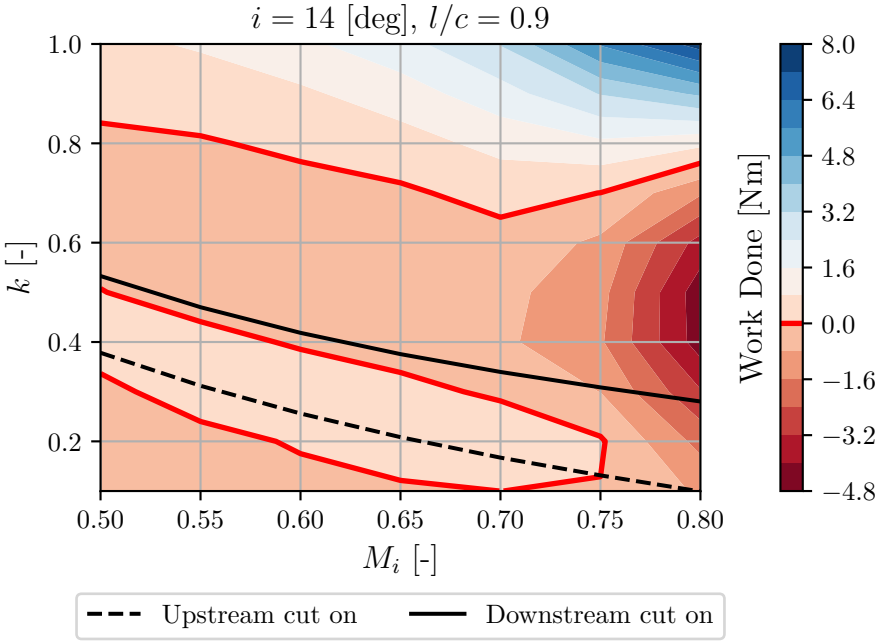


Figure 8.26: Work done per cycle contour as a function of inlet Mach number and reduced frequency

8.7 Chapter Summary

The chapter begins with the validation of the steady and unsteady CFD results against computational implementation for standard configuration 10, showcasing good agreement with Repar's computational studies. Implementation of a sponge layer effectively acts as a 2D non-reflecting boundary condition, ensuring accurate prediction of far-field flow. Investigation of a transonic baseline case reveals unstable plunge-twist ratios occur when downstream acoustic waves are just cut on. A further increase in reduced frequency

destabilises due to energy loss to axial propagation. Aerodamping decreases with increased blade incidence, primarily influenced by twist-induced unsteady lift, especially near stall. Pressure side aerodamping exhibits stabilising effects at low incidences but becomes destabilising with increased incidence due to a velocity drop in the passage. A stability map depicts critical flutter reduced frequency concerning incidence and plunge-twist ratio, highlighting instability near downstream cut-on frequencies. Comparison with a subsonic linear cascade shows destabilisation due to specific flow features near stall rather than just a general increase in steady aerodynamic loading. Increasing inlet Mach numbers generally destabilise the rotor; this is predominantly driven by changes in suction side steady shock structures. A stability map shows that there is a strong correlation between downstream acoustic wave cut-on and flutter instability for a range of Mach numbers.

9 Conclusions

Objective 1

Determine the effect of plunge-twist ratio, reduced frequency and nodal diameter on flutter stability of a two-dimensional cascade using experimentally validated CFD

CFD was validated against experimental data and showed good agreement in terms of steady pressure, amplitude and phase of unsteady pressure and total aerodamping for a range of different mode shapes.

Flutter analysis showed that the most unstable inter-blade phase angles for a range of reduced frequencies and twist axis setbacks were low nodal diameter forward travelling wave modes. It was shown that, generally, increasing the reduced frequency is beneficial for flutter prevention. Analysis of the travelling wave mode coefficients showed that at low reduced frequencies, unsteady disturbances propagate more effectively to the blades that are further away from the vibrating blade 0 as compared to higher frequencies, which in turn decreases aerodamping. For high reduced frequencies, it was shown that the aerodamping tends to zero as the blades become too stiff to be affected by the flow. It was shown that generally larger plunge-twist ratios are beneficial for preventing flutter. For some reduced frequencies, the mode stabilises as $l/c \to 0.5$ for a pure twist mode shape, indicating that it is the cross coupling of plunge and twist vibration that induces the largest instability at slightly larger l/c.

A stability map was developed that showed that for this cascade, some of the blade stiffness could be sacrificed to reduce the modal frequency in favour of a higher plunge-twist ratio to move the aerodamping to its most stable location. The stability map showed that the flutter limit follows an offset rectangular hyperbola of reduced frequency and twist axis setback for the most unstable inter-blade phase angle $\sigma_m = 40^\circ$.

It was noted that the implementation of the linear cascade creates some flow features that are not representative of those in a typical low-speed compressor section. This brought into question how well the linear cascade approximates the flow in a low-speed compressor and the validity of the AIC method to determine the aerodamping. To validate the implementation, four different cascades were investigated. The results showed that, despite different implementations, the results were very similar. The conclusion is that steady aerodynamic loading is not as critical as expected, and despite the fact that the linear cascade is not tuned, the aerodynamic influence coefficient method is still effective for predicting aerodamping. The primary reason for this is that the blades closest to the vibrating blade 0 have a similar loading,

and the influence of blades near the walls contributes very little to the total aerodamping. It was shown that the aerodamping for 1F flutter of the linear cascade can be effectively predicted using a purely analytical implementation of the program code LINSUB [72]. This method had the additional benefit that the code is freely available and faster than the high-fidelity CFD used in the simulation of the linear cascade.

The primary goal of this objective was to validate the effect of reduced frequency, plunge-twist ratio, and nodal diameter using experimental CFD. The reasoning behind this goal is that, frequently, investigations of these parameters are purely computational methods in the literature. The results presented agree with those from the literature and critically validate the observed trends using experimental data.

Objective 2

Develop a flutter model to physically explain the location of the stability limit based on the results from the parametric study of the modal variables

A flutter model was developed based on the assumption that plunge and twist vibration induced incidence is responsible for the change in aerodynamic loading that causes flutter. The aerodynamic response was defined as the unsteady lift and unsteady moment from which the work done per cycle components can be found, which sum to produce the total work done per cycle and subsequently the aerodamping. It was shown that in this case, the amplitude of the unsteady lift and unsteady moment is proportional to the vibration induced incidence, meaning that the unsteady response is in fact driven by the change in incidence. However, this still left the phase to be determined. Further simplifications were made to the model based on results from the subsonic linear cascade. In the final section, an expression was derived for the flutter stability limit, which could be determined from known input parameters and the phase of unsteady lift and moment due to twist vibration. It was shown that the flutter stability limit can be defined by a non-standard rectangular hyperbola of reduced frequency and normalised twist axis setback. The hyperbola is defined as non-standard as it is still a weak function of reduced frequency. Further analysis showed that this hyperbola can be defined as the 'plunge-twist incidence ratio', which is the ratio of the amplitude of the plunge induced incidence and the twist induced incidence. In conclusion, it was stated that engine designers should aim to design blades with a large plunge-twist incidence ratio to ensure that flutter does not occur.

Objective 3

Determine how the inlet Mach number and flow incidence affect flutter stability of a highly loaded two-dimensional compressor cascade

Firstly, the steady and unsteady results were validated against the computational implementation of Repar, as experimental data for the compressor cascade standard configuration 10 is not available. The results showed very good agreement with the steady-state flow. Implementation of a sponge layer in the inlet and outlet ducts effectively modified the one-dimensional non-reflecting boundary conditions into a two-dimensional non-reflecting boundary condition. There is a good agreement with the work of Repar for the spikes in aerodamping associated with circumferentially propagating acoustic waves, which indicates that the flow in the far field is being correctly predicted.

The transonic baseline test case for standard configuration 10 was investigated. This revealed that reduced frequencies with the largest number of unstable plunge-twist ratios occurred when the downstream acoustic wave was just cut on. The change in the downstream acoustic wave from cut off to cut on as reduced frequency is increased caused a destabilising change in the phase of the shock. As the reduced frequency is increased further, additional energy is lost to the axial propagation of the downstream acoustic wave, which then results in high reduced frequencies becoming flutter stable. It was shown that the stabilising of the mode as the plunge-twist ratio is reduced down towards pure twist is due to the stabilising effect of the twist vibration induced unsteady moment. Additionally, it was demonstrated that the large destabilising effect at low plunge-twist ratios is caused by the twist vibration induced unsteady lift.

A decrease in aerodamping was observed when the incidence on the blade increased. The trends observed in the aerodamping were predominantly influenced by the aerodamping due to twist vibration-induced unsteady lift, accounting for almost all of the unstable contribution to the aerodamping at large incidences near stall. It was also shown that a change in the acoustic wave properties is unlikely to be driving the instability seen at large incidences. The pressure side local aerodamping was identified as driving the trends observed in the total aerodamping as the incidence increased. There was a large stabilising effect near the leading on the pressure side for low incidences due to a local stabilising flow separation due to the near choke operating point. As the incidence increases, there is a destabilising offset in phase on the pressure side due to the drop in axial velocity in the passage. The suction side aerodamping has much smaller changes as the destabilising effect of increased shock strength cancels with the stabilising trailing edge

separation. A stability map was created that showed the critical flutter reduced frequency as a function of incidence and plunge-twist ratio for many different incidences. This map revealed that for multiple incidences, the least stable reduced frequencies are those just above the downstream cut on reduced frequency. The flutter stability limit for the standard configuration 10 cascade was compared to that of the subsonic linear cascade. It was shown that it is not an increase in steady loading that is destabilising, but rather specific flow features near stall that are destabilising. It was also highlighted that a constant plunge-twist incidence ratio is no longer an effective definition of the flutter stability limit. This is due to complex flow features such as shocks and separations, which break the assumptions made in the definition of the model.

The inlet Mach number was varied at constant incidence and showed that, in general, increasing the inlet Mach number destabilises the rotor. It was shown that the decrease in aerodamping is driven by the change in aerodamping on the suction side, which in turn is related back to the amplitude change in unsteady pressure due to the steady shock structure. A stability map of the inlet Mach number and reduced frequency was defined. It was shown that the cut on of the downstream acoustic wave is destabilising for all inlet Mach numbers. Additionally, it was shown that reduced frequencies where the upstream acoustic wave is cut on and the downstream acoustic wave is cut off is stabilising for most inlet Mach numbers. This is quite contrary to the literature for transonic fans, but it was shown that it may be possible to relate this back to radial flow migration on the suction side, which is not possible for the two-dimensional case.

10 Future Work

- It was shown in chapter 8 that the most unstable mode shapes are those with a reduced frequency, which is slightly above the downstream acoustic wave cut on reduced frequency. This is the opposite trend observed in transonic fans, which typically show instability when the upstream acoustic wave is cut on and the downstream acoustic wave is cut off. Further work should be conducted on both the standard configuration 10 geometry and a transonic fan to better understand the difference in these observed trends. Additionally, there is work in the literature that suggests that the acoustic wave properties and flutter are highly geometry-specific and should be examined.

- It was shown in chapter 7 that the stability limit can be defined by an approximately constant plunge-twist incidence ratio. Further work should be conducted to see if the plunge-twist incidence ratio can effectively be used as a flutter stability criteria for a transonic compressor. Primarily, it should be found if the unsteady lift and moment are still driven by the vibration induced flow incidence, or if flow features such as shock waves and radial flow migration mean that generated response is no longer a function of vibration induced incidence only.

- Further work should be conducted to investigate the effect of changing the gradients of the phase of unsteady lift due to twist and the phase of unsteady moment due to twist with respect to reduced frequency to find out the effect of this on the location and shape of the flutter stability limit.

- The flutter model should be expanded, and a relationship for the phase lag with respect to the inter-blade phase angle should be found to generalise the model for all inter-blade phase angles.

- All of the mode shapes in this thesis are assumed to be rigid bodies. In actuality, the mode shape of a typical aero engine compressor blade will have some flexion of the blades themselves. The term preferred by the author for this is 'combined mode contamination'. It is suspected that flexion of the blades, which act to increase the amount of twist in the mode shape, will be destabilising. Further work should be conducted to investigate the effect of contamination in combined mode shapes on flutter stability.

Bibliography

[1] A. V. Srinivasan, "Flutter and Resonant Vibration Characteristics of Engine Blades," in *Volume 4: Manufacturing Materials and Metallurgy; Ceramics; Structures and Dynamics; Controls, Diagnostics and Instrumentation; Education; IGTI Scholar Award*, vol. 4, American Society of Mechanical Engineers, jun 1997.

[2] B. Beirow, T. Giersch, A. Kühhorn, and J. Nipkau, "Forced Response Analysis of a Mistuned Compressor Blisk," *Journal of Engineering for Gas Turbines and Power*, vol. 136, jun 2014.

[3] M. Matsumoto, H. Shirato, T. Yagi, R. Shijo, A. Eguchi, and H. Tamaki, "Effects of aerodynamic interferences between heaving and torsional vibration of bridge decks: the case of Tacoma Narrows Bridge," *Journal of Wind Engineering and Industrial Aerodynamics*, vol. 91, pp. 1547–1557, dec 2003.

[4] M. M. Abdel Hafeez and A. A. El-Badawy, "Flutter Limit Investigation for a Horizontal Axis Wind Turbine Blade," *Journal of Vibration and Acoustics*, vol. 140, aug 2018.

[5] V. V. Vedeneev, M. Kolotnikov, and P. Makarov, "Experimental validation of numerical blade flutter prediction," *Journal of Guidance, Control, and Dynamics*, vol. 38, no. 6, pp. 1281–1291, 2015.

[6] M. Vahdati and N. Cumpsty, "Aeroelastic Instability in Transonic Fans," *Journal of Engineering for Gas Turbines and Power*, vol. 138, no. 2, pp. 1–14, 2015.

[7] T. Brandvik and G. Pullan, "An Accelerated 3D Navier–Stokes Solver for Flows in Turbomachines," *Journal of Turbomachinery*, vol. 133, apr 2011.

[8] J. C. MacBain, J. E. Horner, W. A. Stange, and J. S. Ogg, "Vibration analysis of a spinning disk using image-derotated holographic interferometry," *Experimental Mechanics*, vol. 19, pp. 17–22, jan 1979.

[9] D. J. Ewins, "Vibration Characteristics of Bladed Disc Assemblies.," *J Mech Eng Sci*, vol. 15, no. 3, pp. 165–186, 1973.

[10] Y. Lu, B. Lad, J. Green, S. Stapelfeldt, and M. Vahdati, "Effect of Geometry Variability on Transonic Fan Blade Untwist †," *International*

Journal of Turbomachinery, Propulsion and Power, vol. 4, p. 24, aug 2019.

[11] J. Nipkau, *Analysis of mistuned blisk vibrations using a surrogate lumped mass model with aerodynamic influences*. PhD thesis, BTU Cottbus - Senftenberg, 2011.

[12] W. Sears, "Some Aspects of Non-Stationary Airfoil Theory and Its Practical Application," *Journal of the Aeronautical Sciences*, vol. 8, no. 3, pp. 104–108, 1941.

[13] A. R. Collar, "The Expanding Domain of Aeroelasticity," *The Journal of the Royal Aeronautical Society*, vol. 50, pp. 613–636, aug 1946.

[14] J. S. Green, "Forced Response of a Large Civil Fan Assembly," in *Volume 5: Structures and Dynamics, Parts A and B*, pp. 685–692, ASMEDC, jan 2008.

[15] M. Vahdati, A. I. Sayma, M. Imregun, and G. Simpson, "Multibladerow Forced Response Modeling in Axial-Flow Core Compressors," *Journal of Turbomachinery*, vol. 129, pp. 412–420, apr 2007.

[16] L. di Mare, G. Simpson, and A. I. Sayma, "Fan Forced Response Due to Ground Vortex Ingestion," in *Volume 5: Marine; Microturbines and Small Turbomachinery; Oil and Gas Applications; Structures and Dynamics, Parts A and B*, pp. 1123–1132, ASMEDC, jan 2006.

[17] A. N. Rao, P. Sureshkumar, S. Stapelfeldt, B. Lad, K.-B. Lee, and R. P. Rico, "Unsteady Analysis of Aeroengine Intake Distortion Mechanisms: Vortex Dynamics in Crosswind Conditions," *Journal of Engineering for Gas Turbines and Power*, vol. 144, dec 2022.

[18] R. E. Kielb, J. W. Barter, J. P. Thomas, and K. C. Hall, "Blade Excitation by Aerodynamic Instabilities: A Compressor Blade Study," in *Volume 4: Turbo Expo 2003*, no. June, pp. 399–406, ASMEDC, jan 2003.

[19] S. Stapelfeldt and C. Brandstetter, "Non-synchronous vibration in axial compressors: Lock-in mechanism and semi-analytical model," *Journal of Sound and Vibration*, vol. 488, p. 115649, dec 2020.

[20] Y.-c. Fung, *An Introduction to the Theory of Aeroelasticity*. New York: Wiley, 1955.

[21] M. F. Platzer and F. O. Carta, "AGARD Manual on Aeroelasticity in Axial-Flow Turbomachines. Volume 1. Unsteady Turbomachinery Aerodynamics," tech. rep., Advisory group for aerospace research and development, Neuilly-Sur-Seine, 1987.

[22] S. Stapelfeldt and M. Vahdati, "On the importance of engine-representative models for fan flutter predictions," *Journal of Turbomachinery*, vol. 140, no. 8, 2018.

[23] O. O. Bendiksen and P. P. Friedmann, "Effect of Bending-Torsion Coupling on Fan and Compressor Blade Flutter.," *American Society of Mechanical Engineers (Paper)*, no. 81 -GT-163, 1981.

[24] F. Zhao, *Embedded Blade Row Flutter*. PhD thesis, 2016.

[25] M. Vahdati, G. Simpson, and M. Imregun, "Mechanisms for wide-chord fan blade flutter," *Journal of Turbomachinery*, vol. 133, no. 4, pp. 1–7, 2011.

[26] F. Zhao, J. Nipkau, and M. Vahdati, "Influence of acoustic reflections on flutter stability of an embedded blade row," *Proceedings of the Institution of Mechanical Engineers, Part A: Journal of Power and Energy*, vol. 230, no. 1, pp. 29–43, 2016.

[27] D. S. Whitehead, "Torsional flutter of unstalled cascade blades at zero deflection," no. 3429, 1964.

[28] J. Panovsky and R. E. Kielb, "A Design Method to Prevent Low Pressure Turbine Blade Flutter," *Journal of Engineering for Gas Turbines and Power*, vol. 122, no. 1, pp. 89–98, 2000.

[29] D. Halliwell, "Fan Supersonic Flutter: Prediction and Test Analysis," 1975.

[30] K. B. Lee, M. Wilson, and M. Vahdati, "Numerical study on aeroelastic instability for a low-speed fan," *Journal of Turbomachinery*, vol. 139, no. 7, 2017.

[31] S. Iseni, D. Micallef, and F. di Mare, "Sensitivity analysis of eigenmode variations on the flutter stability of a highly loaded transonic fan," in *Proceedings of GPPS Forum 18*, no. May, pp. 1–9, GPPS, 2018.

[32] R. Kielb, J. Barter, O. Chernycheva, and T. Fransson, "Flutter of low pressure turbine blades with cyclic symmetric modes: A preliminary

design method," *Journal of Turbomachinery*, vol. 126, no. 2, pp. 306–309, 2004.

[33] X. Jia, H. Huang, and D. Wang, "Effect of Fan Blade Vibration Mode on Flutter Stability," in *Proceedings of Global Power and Propulsion Society*, GPPS, 2021.

[34] X. Dong, Y. Zhang, Y. Zhang, Z. Zhang, and X. Lu, "Numerical simulations of flutter mechanism for high-speed wide-chord transonic fan," *Aerospace Science and Technology*, vol. 105, p. 106009, oct 2020.

[35] F. Sisto, "Stall-Flutter in Cascades," *Journal of the Aeronautical Sciences*, vol. 20, pp. 598–604, sep 1953.

[36] F. O. Carta, "Coupled Blade-Disk-Shroud Flutter Instabilities in Turbojet Engine Rotors," *Journal of Engineering for Power*, vol. 89, pp. 419–426, jul 1967.

[37] F. Zhao, "Impact of mode shape and acoustic gust on blade flutter stability," in *Proceedings of the 15th International Symposium on Unsteady Aerodynamics, Aeroacoustics & Aeroelasticity of Turbomachines*, (Oxford), pp. 1–10, ISUAAAT, 2018.

[38] H. Huang, M. Yang, and D. Wang, "Uncovering the Root Causes of Stall Flutter in a Wide Chord Fan Blisk," *International Journal of Turbomachinery, Propulsion and Power*, vol. 7, no. 4, 2022.

[39] J. Nipkau, B. Power, and M. Jordan, "Aeromechanical design and test of a modern highly loaded fan," *Proceedings of the ASME Turbo Expo*, vol. 2B, pp. 1–11, 2017.

[40] S. Stapelfeldt and M. Vahdati, "Improving the Flutter Margin of an Unstable Fan Blade," *Journal of Turbomachinery*, vol. 141, no. 7, 2019.

[41] J. D. Gill, V. R. Capece, and R. B. Fost, "Experimental methods applied in a study of stall flutter in an axial flow fan," *Shock and Vibration*, vol. 11, pp. 597–613, 2004.

[42] T. E. Smith and J. R. Kadambi, "The Effect of Steady Aerodynamic Loading on the Flutter Stability of Turbomachinery Blading," *Journal of Turbomachinery*, vol. 115, pp. 167–174, jan 1993.

[43] F. Zhao, N. Smith, and M. Vahdati, "A simple model for identifying the flutter bite of fan blades," *Journal of Turbomachinery*, vol. 139, no. 7, 2017.

[44] Q. Rendu, M. Vahdati, and L. Salles, "Radial Decomposition of Blade Vibration to Identify a Stall Flutter Source in a Transonic Fan," *Journal of Turbomachinery*, vol. 141, no. 10, 2019.

[45] M. Vahdati, A. I. Sayma, J. G. Marshall, and M. Imregun, "Mechanisms and prediction methods for fan blade stall flutter," *Journal of Propulsion and Power*, vol. 17, no. 5, pp. 1100–1108, 2001.

[46] K. Isomura and M. B. Giles, "A numerical study of flutter in a transonic fan," *Proceedings of the ASME Turbo Expo*, vol. 4, no. July, pp. 500–507, 1997.

[47] M. Aotsuka and T. Murooka, "Numerical Analysis of Fan Transonic Stall Flutter," in *Volume 7B: Structures and Dynamics*, American Society of Mechanical Engineers, jun 2014.

[48] M. B. Giles, "Nonreflecting boundary conditions for Euler equation calculations," *AIAA Journal*, vol. 28, pp. 2050–2058, dec 1990.

[49] J. M. Tyler and T. G. Sofrin, "Axial Flow Compressor Noise Studies," pp. 309–332, jan 1962.

[50] B. Hellmich and J. R. Seume, "Causes of Acoustic Resonance in a High-Speed Axial Compressor," *Journal of Turbomachinery*, vol. 130, no. 3, 2008.

[51] P. Moinier and M. B. Giles, "Eigenmode analysis for turbomachinery applications," *Journal of Propulsion and Power*, vol. 21, no. 6, pp. 973–978, 2005.

[52] F. Zhao, J. Nipkau, and M. Vahdati, "A simple low-fidelity model for embedded blade row flutter prediction," *Proceedings of the ASME Turbo Expo*, vol. 7B, pp. 1–13, 2015.

[53] T. Colonius, S. K. Lele, and P. Moin, "Boundary conditions for direct computation of aerodynamic sound generation," *AIAA Journal*, vol. 31, pp. 1574–1582, sep 1993.

[54] P. R. Spalart, S. R. Allmaras, and J. Reno, "One-Equation Turbulence Model for Aerodynamic Flows," *AIAA*, p. 23, 1992.

[55] K. B. Lee, M. Wilson, and M. Vahdati, "Validation of a numerical model for predicting stalled flows in a low-speed fan-Part I: Modification of Spalart-Allmaras turbulence model," *Journal of Turbomachinery*, vol. 140, no. 5, 2018.

[56] Y. Liu, L. Lu, L. Fang, and F. Gao, "Modification of Spalart–Allmaras model with consideration of turbulence energy backscatter using velocity helicity," *Physics Letters A*, vol. 375, pp. 2377–2381, jun 2011.

[57] L. Ma, L. Lu, J. Fang, and Q. Wang, "A study on turbulence transportation and modification of Spalart–Allmaras model for shock-wave/turbulent boundary layer interaction flow," *Chinese Journal of Aeronautics*, vol. 27, pp. 200–209, apr 2014.

[58] A. I. Sayma, M. Vahdati, L. Sbardella, and M. Imregun, "Modeling of three-dimensional viscous compressible turbomachinery flows using unstructured hybrid grids," *AIAA journal*, vol. 38, no. 6, pp. 945–954, 2000.

[59] R. Swanson and E. Turkel, "On central-difference and upwind schemes," *Journal of Computational Physics*, vol. 101, pp. 292–306, aug 1992.

[60] J. Dodds and M. Vahdati, "Rotating Stall Observations in a High Speed Compressor—Part II: Numerical Study," *Journal of Turbomachinery*, vol. 137, may 2015.

[61] S. C. Stapelfeldt, A. B. Parry, and M. Vahdati, "Investigation of flutter mechanisms of a contra-rotating open rotor," *Journal of Turbomachinery*, vol. 138, no. 5, pp. 1–10, 2016.

[62] M. Vahdati and M. Imregun, "A non-linear aeroelasticity analysis of a fan blade using unstructured dynamic meshes," *Proceedings of the Institution of Mechanical Engineers, Part C: Journal of Mechanical Engineering Science*, vol. 210, no. 6, pp. 549–564, 1996.

[63] N. M. Newmark, "A Method of Computation for Structural Dynamics," *Journal of the Engineering Mechanics Division*, vol. 85, pp. 67–94, jul 1959.

[64] Y. Hanamura, H. Tanaka, and K. Yamaguchi, "A Simplified Method to Measure Unsteady Forces Acting on the Vibrating Blades in Cascade," *Bulletin of JSME*, vol. 23, no. 180, pp. 880–887, 1980.

[65] F. O. Carta, "Unsteady Gapwise Periodicity of Oscillating Cascaded Airfoils," in *ASME 1982 International Gas Turbine Conference and Exhibit*, pp. 1–15, American Society of Mechanical Engineers, apr 1982.

[66] L. Malzacher, S. Geist, D. Peitsch, and H. Hennings, "A Low Speed Compressor Test Rig for Flutter Investigations," in *Volume 7B: Structures and Dynamics*, pp. 1–12, American Society of Mechanical Engineers, jun 2016.

[67] J. Ren, H. Huang, D. Wang, X. Dong, and B. Cao, "An efficient coupled-mode flutter analysis method for turbomachinery," *Aerospace Science and Technology*, vol. 106, p. 106215, nov 2020.

[68] E. F. Crawley and K. C. Hall, "Optimization and mechanisms of mistuning in cascades," *Journal of Engineering for Gas Turbines and Power*, vol. 107, no. 2, pp. 418–426, 1985.

[69] H. Försching, "A Parametric Study of the Flutter Stability Characteristics of Turbomachine Cascades," in *Volume 5: Manufacturing Materials and Metallurgy; Ceramics; Structures and Dynamics; Controls, Diagnostics and Instrumentation; Education; General*, American Society of Mechanical Engineers, jun 1996.

[70] G. Zambonini, X. Ottavy, and J. Kriegseis, "Corner Separation Dynamics in a Linear Compressor Cascade," *Journal of Fluids Engineering*, vol. 139, jun 2017.

[71] J. Belz and H. Hennings, "Experimental flutter investigations of an annular compressor cascade: influence of reduced frequency on stability," in *Unsteady Aerodynamics, Aeroacoustics, and Aeroelasticity of Turbomachines*, pp. 77–91, Dordrecht: Kluwer Academic Publishers, 2006.

[72] D. S. Whitehead, "Classical two-dimensional methods," *AGARD Aeroelasticity in Axial-Flow Turbomachines*, vol. 1, pp. 58–88, 1987.

[73] D. S. Whitehead, "Force and Moment Coefficients for Vibrating Aerofoils in Cascade," in *Aeronautical Research Council Reports and Memoranda*, no. 3254, 1962.

[74] N. Cumpsty, *Compressor Aerodynamics*. Krieger Publishing, 2004.

[75] A. Vega and R. Corral, "The low reduced frequency limit of vibrating airfoils-Part II: Numerical experiments," *Journal of Turbomachinery*, vol. 138, no. 2, pp. 1–9, 2016.

[76] T. H. Fransson and J. M. Verdon, "Updated report on Standard Configurations for the Determination of unsteady Flow Through Vibrating Axial-flow Turbomachine-Cascades," in *Proceedings of the 6th International Conference on Aeroelasticity in Turbomachines*, 1991.

[77] P. J. Petrie-Repar, A. McGhee, and P. A. Jacobs, "Three-Dimensional Viscous Flutter Analysis of Standard Configuration 10," in *Volume 5: Turbo Expo 2007*, pp. 665–674, ASMEDC, jan 2007.

[78] H. M. Phan and L. He, "Validation Studies of Linear Oscillating Compressor Cascade and Use of Influence Coefficient Method," *Journal of Turbomachinery*, vol. 142, pp. 1–11, may 2020.

[79] H. Verschueren, *Stall inception in high stage loading low pressure ratio transonic fans*. PhD thesis, University of Cambridge, 2020.

[80] P. J. Petrie-Repar, A. McGhee, P. A. Jacobs, and R. Gollan, "Analytical Maps of Aerodynamic Damping as a Function of Operating Condition for a Compressor Profile," in *Volume 5: Marine; Microturbines and Small Turbomachinery; Oil and Gas Applications; Structures and Dynamics, Parts A and B*, pp. 1133–1144, ASMEDC, jan 2006.

Appendices

I Proof of Work Done Analysis

$$\ddot{x} + 2\zeta\omega\dot{x} + \omega^2 x = 0 \tag{.1}$$

$$F_d = -c\dot{x} = -\zeta c_c \dot{x} = -2\zeta m\omega_n \dot{x} \tag{.2}$$

$$dW = -\int F_d dx = 2\zeta m\omega_n \int \dot{x} dx = 2\zeta m\omega_n \int \dot{x}^2 dt \tag{.3}$$

$$K_E = \frac{1}{2} m\dot{x}^2 \tag{.4}$$

$$\bar{K}_E = \frac{1}{T}\int K_E dt = \frac{m}{2T}\int \dot{x}^2 dt = \frac{m\omega_d}{4\pi}\int \dot{x}^2 dt \tag{.5}$$

where $T = 2\pi/\omega_d$ is the period of the damped motion. It should also be known that $\omega_d = \omega_n\sqrt{1-\zeta^2}$

$$\frac{W}{\bar{K}_E} = \frac{8\pi\zeta}{\sqrt{1-\zeta^2}} \tag{.6}$$

$$\delta = \frac{2\pi\zeta}{\sqrt{1-\zeta^2}} \tag{.7}$$

$$\delta = \frac{W}{4\bar{K}_E} \tag{.8}$$

$$\bar{K}_E = \frac{K_{E,max} - K_{E,min}}{2} \tag{.9}$$

$$\delta = \frac{W}{2K_{E,max}} \tag{.10}$$

$$K_{E,max} = \frac{1}{2} m_r \omega^2 \tag{.11}$$

$$\hat{\dot{q}}^2 = m_r\omega^2 \tag{.12}$$

$$\delta = \frac{W}{\hat{\dot{q}}^2} \tag{.13}$$